COMPARTMENTALIZATION AND GRAIN-FABRIC ALIGNMENTS IN MIXED CARBONATE-SILICICLASTICS MASS-TRANSPORT DEPOSITS: THE CUTOFF FORMATION, PERMIAN BASIN, TEXAS

by

Hanaga Simabrata

A thesis submitted to the Faculty and the Board of Trustees of the Colorado School of Mines in partial fulfillment of the requirements for the degree of Master of Science (Geology).

Golden, Colorado

Date _____

Signed: _____

Hanaga Simabrata

Signed: _____

Dr. Lesli Wood
Thesis Advisor

Signed: _____

Dr. Zane Jobe
Thesis Advisor

Golden, Colorado

Date _____

Signed: _____

Dr. Wendy Bohrson
Professor and Head
Department of Geology and Geological Engineering

ABSTRACT

Mass-transport deposits (MTDs) comprise complex, multi-scale deformation that renders them unique compared to sediments of other depositional origins. The topics of this research entail compartmentalization (outcrops) and grain-fabric modifications (thin sections) in MTDs developed during the emplacement processes, which can significantly impact formation heterogeneity and anisotropy. Our research emphasizes on (1) the recognition criteria of sub-seismic MTD compartments and (2) qualitative and quantitative characterizations of grain-fabric alignments, both of which utilize the well-exposed Cutoff MTDs in the Permian Basin, Texas.

Our study shows that sub-seismic compartments in MTDs can be predicted from the intersegment contrasts of lithofacies, deformation types, and deformation orientations. Using these recognition criteria in conjunction increases the likelihood of identifying MTD compartments. Thin section analysis over 29.000 elongated grains (predominantly sponge spicules) reveals that grain-fabric alignments in MTDs are heterogeneous in multiple scales, and are likely controlled by grain lengths (with constant aspect ratio) and matrix types.

The results of this study contribute to the following fields: (1) identification of sub-seismic MTD compartments, which can serve as barriers or conduits to fluid flow, (2) anisotropy prediction of petrophysical (e.g., permeability) and mechanical (elastic moduli) properties, (3) the kinematic of MTD evolution during emplacement, including the origins of MTD compartments and the prediction of paleotransport directions.

TABLE OF CONTENTS

ABSTRACT iii

LIST OF FIGURES viii

LIST OF TABLES xvi

CHAPTER 1 CHARACTERIZATION OF VERTICAL SEGMENTS IN MASS-TRANSPORT DEPOSITS: THE CUTOFF FORMATION, PERMIAN BASIN, TEXAS 1

1.1 Abstract 1

1.2 Introduction 2

1.3 Geological Context 4

1.3.1 Regional 4

1.3.2 The Cutoff MTDs 5

1.3.3 Area of Interest 11

1.4 Methods 11

1.4.1 Lithofacies 12

1.4.2 Microstructure Types and Deformation Orientations 15

1.5 Result and Interpretation 15

1.5.1 MTD Architecture 15

1.5.2 Correlation 17

1.5.3 Segment A 25

1.5.4 Segment B 26

1.5.5 Segment C 27

1.5.6 Recognition Criteria for MTD Segments 29

1.6 Discussion 36

1.6.1 Kinematic Evolution of The Cutoff MTDs 36

1.6.2 Grain-fabric Alignments and Anisotropy 39

1.6.3 Silicification and Flow Barrier 42

1.7 Conclusions 44

CHAPTER 2 GRAIN-FABRIC ALIGNMENTS IN MIXED CARBONATE-SILICICLASTIC MASS-TRANSPORT DEPOSITS: THE CUTOFF FORMATION, PERMIAN BASIN, TEXAS 46

2.1 Abstract 46

2.2 Introduction 47

2.3 Geological Context 49

2.3.1 Regional 49

2.3.2 The Cutoff MTD 50

2.3.3 Area of Interest 53

2.4 Methods 54

2.4.1 Sample Preparation and Analysis 55

2.4.2 Quantification of Spicule Orientations 59

2.5 Results 62

2.5.1 Lithofacies and Microstructure Types 62

2.5.2 Spicule Orientations 63

2.5.3 Spicule Abundance, Length, and Aspect Ratio 73

2.5.4 Quantitative Analysis of Spicule Trends 75

2.6 Discussion 82

2.6.1 The Origin of Microstructures 82

2.6.2 The Origin of Spicule Alignments 84

2.6.3 Paleotransport of The Cutoff MTDs 84

2.6.4 Anisotropy Promoted by Grain-fabric Alignments 85

2.6.5 Predicting Grain-fabric Alignments from Large-scale Data 87

2.7 Conclusions 88

REFERENCES 91

APPRENDIX A SUPPLEMENTARY FILES 100

LIST OF FIGURES

Figure 1.1 (A) Basin configuration: the Permian Basin consists of the Delaware Basin to the west and the Midland Basin to the east, separated by the Central Basin Platform. The area of interest (Guadalupe Mts.) is signified by the red rectangle near the northwestern margin of the Delaware Basin. (B) Simplified illustration of slope-to-basin depositional systems of the Cutoff Formation. 7

Figure 1.2 (A) Exposure map of the Cutoff Formation, Guadalupe Mountains: The research focus is in the Rest Area Gully Locality where the Cutoff MTDs exhibit compartmentalization. (B) The estimated size of the Cutoff MTDs: The lengths of the Cutoff MTDs is at least 14 km and 21 km according to slope- and transport-parallel measurements, respectively. Applying the morphometric relationship compiled by Moscardelli and Wood (2015) to the estimated MTD lengths, we estimate that the area of the Cutoff MTDs is at least 93 km^2 to 190 km^2, which measures are comparable to, if not larger than, the MTDs documented in the Delaware Basin (Allen et al., 2013) and the Midland Basin (Bhatnagar et al.,2019). 8

Figure 1.3 (A) Rest Area Gully: This research focuses on two cliff-face outcrops called Snake Rock (SR) and Lunch Cliff (LC). About 200 meters downstream from the SR and LC is the location of massive sandstone outcrop in figure 3B. (B) The units of interest overlay the massive sandstone unit (~3m), which is interpreted as high-density turbidite (non-MTD). The bedding orientation of this massive sandstone likely reflects the depositional dip. (C) Our drone model suggests that the dip of termination surfaces in the area of interest are similar to that of the massive sandstone.....9

Figure 1.4 (A) Termination surfaces and complex folding in Snake Rock (uninterpreted). (B) Interpretation of figure 4A. (C) Termination surfaces and complex folding in Lunch Cliff (uninterpreted). (D) Interpretation of figure 4C. 10

Figure 1.5 (A) Calcium vs. Silicon. (B) Potassium vs. Titanium. (C) Titanium vs. Iron. (D) Clay indicator vs. silicon.....13

Figure 1.6 Thin section (top right) and composition masp in the same location (rest of the figures): Clayey to clay-rich packstone microbeds (white pin) contain high potassium (K), titanium (Ti), and iron (Fe). Highly silicified packstone microbeds (yellow pin) have relatively higher silicon (Si). The blue pin is calcite-cemented post-lithification fracture. The thin section location is given in Figure 6.....14

Figure 1.7 (A) uninterpreted Lunch Cliff outcrop: white arrows are the position of major termination surfaces. The yellow line is the location of measured section. The

green circle is human for scale. (B) interpreted Lunch Cliff outcrop: Consist of segment A, C, and D (not sampled) that are bounded by major termination surfaces LC 0 and LC 2. Other major termination surfaces are observed around A-C segment contact, which result in closely-spaced sub-segments. Minor termination surfaces (dashed lines) can be high-dipping (thrust faults) and low-dipping (shear surfaces and intra-fold truncations). Some of the thrust faults are detached from the bounding termination surfaces, e.g., see the southern part of surface LC 0 and LC 1. Smaller intra-fold truncations are not shown here. 18

Figure 1.8 (A) uninterpreted Snake Rock outcrop: white arrows are the position of major termination surfaces. The yellow line is the location of measured section. The lower photomosaic overlaps with the upper one exactly at the uppermost termination surface SR-Top. (B) Interpreted Snake Rock outcrop: Consist of segment B, C, and D (not sampled) that are bounded by major termination surfaces SR 0 and SR 2. Other major termination surfaces are observed around B-C segment contact, which result in closely-spaced sub-segments. Minor termination surfaces (dashed lines) can be high-dipping (thrust faults) and low-dipping (shear surfaces and intra-fold truncations). Some of the thrust faults are detached from the bounding termination surfaces, e.g., see the northern part of surface SR 1. Smaller intra-fold truncations are not shown here. 19

Figure 1.9 (A) Uninterpreted Bridge outcrop: Red rectangle highlights the zoom-in photo in Figure 9C and 9D. (B) Interpreted Bridge outcrop: Segment B piggybacks on segment A. Major termination surface SR -1 is truncated above LC 0. (C) Interface-mixing phenomenon (uninterpreted). (D) Interpretation of interface mixing: Segment B has been incorporated into segment A along major termination surface LC 0. 20

Figure 1.10 (A) examples of point arrays picked from the drone model. Point arrays in Lunch Cliff are more curved, owing to the shape of the cliff itself. This makes triangulation more suitable in Lunch Cliff. (B) The result of triangulations from Lunch Cliff are projected to Snake Rock point arrays, and the RMS error for each plane - point array pair. 22

Figure 1.11 MTD architecture: The MTDs in the area of interest is divided into three segments based on their lithofacies, i.e., segment A, B, and C. The smaller segments formed around the contact between segments are referred as sub-segment A1, A2, B1, B2, etc., according to the hosting segments and the spatial elevations. The characteristic contrasts between segments and sub-segments are summarized in this figure, and are discussed in detail in the following sub-sections. 23

Figure 1.12 MTD architecture (borehole style): The MTDs in the area of interest is divided into segments based on their lithofacies, i.e., segment A, B, and C. The smaller segments formed around the contact between segments are referred as sub-segment A1, A2, B1, B2, etc., according to the hosting segments and the

spatial elevations. The characteristic contrasts between segments and sub-segments are also summarized in this figure, and are discussed in detail in the following sub-sections. 24

Figure 1.13 XRF data of resilient and fissile beds grouped according to the segments and outcrop locations. 32

Figure 1.14 The log tracks are given as follows (from left to right): (1) sub-segment name, (2) lithology, deformation style, and the stratigraphic position of photos (right), (3) the proportion of Calcium and Silicon in resilient beds (wt.%), (4) clay indicators (wt.%) for resilient (blue line) and fissile beds (brown line), and (5) bidirectional lineation orientation -- left to right panel is 0 - 180 degrees of compass direction. The rose diagrams summarize the strike of extensional microstructures (green), microfolds and microboudins (blue), and fold axes (red). Photo: yellow arrows are gravel-sized clasts and ripped-up clasts. Green arrows are black beds and microbeds (high calcium, usually packstone). Blue arrows are recumbent microfolds. The grew arrow is sharp-based, fining upward packstone - grainstone. The red arrow is microfracture. 33

Figure 1.15 The log tracks are given as follows (from left to right): (1) sub-segment name, (2) lithology, deformation style, and the stratigraphic position of photos (right), (3) the proportion of Calcium and Silicon in resilient beds (wt.%), (4) clay indicators (wt.%) for resilient (blue line) and fissile beds (brown line), and (5) bidirectional lineation orientation -- left to right panel is 0 - 180 degrees of compass direction. The rose diagrams summarize the strike of extensional microstructures (green), microfolds and microboudins (blue), and fold axes (red). Photos: yellow arrows are sharp-based, fining upward packstone - grainstone. Green arrows are extensional microfractures. Blue arrows are asymmetrical microboudins. 34

Figure 1.16 The log tracks are given as follows (from left to right): (1) sub-segment name, (2) lithology, deformation style, and the stratigraphic position of photos (right), (3) the proportion of Calcium and Silicon in resilient beds (wt.%), (4) clay indicators (wt.%) for resilient (blue line) and fissile beds (brown line), and (5) bidirectional lineation orientation -- left to right panel is 0 - 180 degrees of compass direction. The rose diagrams summarize the strike of extensional microstructures (green), microfolds and microboudins (blue), and fold axes (red). Photos: The grew arrow is normal microfault associated with poorly-developed microboudins. The red arrow is well-developed microboudins. Yellow arrows are silicified packstone. 35

Figure 1.17 Bulk Plotting can be a powerful tool to predict the number of segments in MTDs. In this example, bulk plotting of extensional microfractures, microfolds, and microboudins reveal three and four segments in Snake Rock and Lunch Cliff, respectively. Note that the data-count (n) used in this procedure has been normalized to avoid over-representation of data from a particular segment. 36

Figure 1.18 (A) Transport-parallel section: The within-block Internal shear surface (ISS) separates the megablock of two distinctive seismic facies. Fault-propagation folds (FPF) are detached from the ISS. (B) transport-perpendicular section: The within-block ISS is offset by series of normal faults. Based on the deformation architecture, the within-block ISS likely predates both the FPF and normal faults. (C) Map of mega-block. (D) Segments bounded by termination surfaces behave like individual MTDs with distinct stress regime, deformation characteristics, and relative transport directions - similar to the contemporary flow-cell model. Large arrows indicate transport directions. The schematic diagram is also applicable to high-order segments.....39

Figure 1.19 Grain-fabric alignments between segments: dot-dash line is the predicted trend of H-index. Note the spikes of H-index on termination surfaces. 41

Figure 1.20 (A) Thin section without red alizarin (cross-polarized light): The black zones are silicified packstone, which terminate abruptly at the base of clayey packstone (yellow arrow). (B) Thin section with red alizarin (plane light): white areas are silicified packstone, which terminate abruptly at the base of clayey - clay-rich packstone (yellow arrow). (C) Thin section with red alizarin (cross-polarized light): yellow arrows indicate silicification along two highly permeable paths within packstone. 43

Figure 2.1 (A). Basin Configuration: The Permian basin is divided into the Delaware Sub-basin and the Midland Sub-basin by the Central Basin Platform. The research area is signified by the red square (Guadalupe Mts.). (B) A simplified diagram adopted from Hurd et al. (2016) and Walker et al. (2021): the deposition of Cutoff Formation had been influenced by the drowned Leonardian Platform and Shelf Margin. 50

Figure 2.2 The Stratigraphy of Cutoff Formation has been mapped in detail by Amerman et al. (2011) and Hurd et al. (2016). The multi-scale deformations in the unit of interest are confined within the top portion of the Cutoff Formation. The deformation intensity increases basinward. The overall paleotransport direction is N-S to NNW - SSE, which is oblique to the paleoslope. This study focused on the Rest Area Gully locale (relic lower slope). 52

Figure 2.3 The Uninterpreted (upper figure) vs. interpreted (lower figure) outcrop photomosaic of the area of interest: The outcrop is divided into three segments with distinct lithofacies characteristics, i.e., segment B, C, and D (segment D is not shown), as well as sub-segments termed B1, B2, C1, and C2. This research focuses on sub-segment B1, B2, and C2. Sub-segment B1 is dominated by extensional microstructures, similar to tension gashes observed by Amerman et al. (2011). Sub-Segment B2 are dominated by asymmetrical microboudins and small asymmetrical (isoclinal) microfolds, while C2 is dominated by large asymmetrical (isoclinal) microfolds. Note that sample B2 represents predominantly small asymmetrical microfolds. 56

Figure 2.4 The right-hand figure illustrates how each thin section is divided into grid of slices. The observed and measured slices were coded as rows (A, B, C, …F) and columns (1, 2, 3,… 12). The upper left figure is the zoom-in of slice A2. One hundred circles were assigned to emulate point-counting. The measurements from each slice were plotted to a rose diagram and analyzed quantitatively. 58

Figure 2.5 (A) This figure illustrates how axial data (red lines) are projected to an arbitrary line (green line). Dashed lines are conjugates of lines from the opposite quadrant. (B) Empirical examples from two real spicule measurements and two artificial data: Axial mean in this research is defined as the direction that gives maximum value for average of squared projections (P^2_{avg}), and at the same time gives lowest B-Err (similar to standard deviation). A condition of where no dominant direction exists is mathematically represented by a constant P^2_{avg} and B-Err. (C) When the peak of P^2_{avg} from all datasets shown in Figure 3B are normalized to 180° angle, we see that the difference of peak and through of P^2_{avg} (H-index) shrinks as the data become more and more dispersed around the circle. 61

Figure 2.6 (A) An example of interpreted thin section, B1 [PERP] - 0: The lithofacies consist of granulose packstone, surrounded by clayey packstone 'matrix'. The most prominent microstructures are packstone-filled extensional microfractures; highly discontinuous with typical length and height of ~1 cm or less, and width of about 1 mm. These microfractures are only visible in cross-polarized light. (B) Uninterpreted thin section B1 [PERP] - 0: the two small boxes represent the zoom-out versions of Fig.6C and Fig.6D. (C) Fining-upward microbed with an erosional base. (D) Contrast between granulose packstone and clayey packstone. 64

Figure 2.7 (A) An example of interpreted thin section, B2 [PERP] - 290: The dominant lithofacies are clayey packstone, followed by clay-rich packstone, and packstone with fining-upward features and sharp bases. The microstructures are isoclinal microfolds that verge downslope. Isoclinal microfolds involving packstone microbeds are discontinuous (detached) with tapered edges. Minor microstructures include thrust and normal microfaults, and microboudin. (B) Uninterpreted thin section B2 [PERP] - 290: The two small boxes represent the zoom-out versions of Fig.7C. (C) Detached microbeds with fining-upward sequence and sharp bases. (D) Replacement - from thin section B2 [BED]: Red zones are dominantly calcite, white zones are silicified, and black zones (opaque) are pyritized. 65

Figure 2.8 (A) An example of interpreted thin section, C2 [PERP] - 316: The composition consists of alternating clayey and clay-rich packstone, surrounded by packstone. Silica replacement belts commonly occupy the base of clayey packstone microbeds. The dominant microstructures are isoclinal microfolds (larger and more continuous than sample B2), with the crests verging upslope. Minor features are thrust, normal, and strike-slip microfaults, as well as a

possible injection. (B) Uninterpreted thin section C2 [PERP] - 316: The two small boxes represent the zoom-out versions of Fig. 8C and Fig.8D. (C) Silica replacement belt under cross-polarized light. (D) Thrust and normal microfaults. 68

Figure 2.9 (A) The mean spicule plunge in B1[PAR]-90 is horizontal, strongly following the apparent-dip of microbeds. (B) The mean spicule plunge in B1 [PERP]-0 is also horizontal, mimicking the apparent-dip of microbeds. (C) In the bedding-plane thin section, B1 [BED], the fine-scale spicule trends are overwhelmingly perpendicular to the direction of microfractures, albeit with minor parallel to sub-parallel variants. (D) The Original vs. dip-corrected rose diagram of spicule trends observed in B1 [BED]. 69

Figure 2.10 (A) The overall mean spicule plunge in B2 [PAR]-200 is about horizontal, similar to the overall mean apparent-dip of microbeds. In fine-scale, the plunge varies in accordance to the local apparent-dip of microbeds. (B) The overall mean spicule plunge in B2 [PERP]-290 almost coincides with the overall mean apparent-dip of microbeds. In fine-scale, the plunge varies in accordance to the local apparent-dip. (C) The bedding-plane thin section B2 [BED] shows that local mean spicule trends are mostly parallel to the local strike of microfolds. (D) The Original vs. dip-corrected rose diagram of spicule trends observed in B2 [BED]. 70

Figure 2.11 (A) The overall mean spicule plunge in C2[PAR]-46 is about horizontal, similar to the overall mean apparent-dip of microbeds. In fine-scale, the spicules are plunging to two directions, NW and SW, following the attitude of their local microbeds. (B) The overall mean spicule plunge in C2[PERP]-316 almost coincides with the overall mean apparent-dip of microbeds. In fine-scale, the plunge variability reflects the local apparent-dip in which the spicules are measured. (C) Local mean spicule trends observed in C2[BED] are following the local strike of microfolds. The wellness of alignments seems to be dependent on the strike curvature of microfolds. For example, spicule alignments on the crestal area, where the curvature is high (e.g, slice #B4), are generally more chaotic than on the flank (e.g., slice E7). (D) The original vs. dip-corrected rose diagram of spicule trends observed in C2[BED]. 71

Figure 2.12 (A) A sample zoom-in figure, roughly covering slice E5 and E6: spicule trends are transverse to the strike of microfractures. (B) A sample zoom-in figure, roughly covering slice B9 and B10: spicule trends are parallel to sub-parallel to the strike of microfolds. (C) A sample zoom-in figure, roughly covering slice B5, B6, C5, and C6: spicules on the limbs of microstructures (low curvature) are more well-organized (unimodal), while spicules on the crest of microstructures (high curvature) are more chaotic (multimodal). 72

Figure 2.13 Distributions of spicule lengths in all samples: The measured spicule lengths are grouped into classes with 10-micron increments. The class medians are taken as the x-axis and the class frequency as the Y-axis. The differences in

length distributions between thin section orientations are due to the obliquity of observation planes with respect to the long-axes of spicules.....75

Figure 2.14 (A) Frequency distribution of dip-corrected H index for all bedding-plane thin sections: The calculated H index from individual slices is grouped into classes with 0.1 increments. The H index class mid-points are taken as the x-axis and frequencies as the y-axis. The upside-down arrows represent the averages of H-index calculated from the histogram, and the number of data (n) is essentially the total number of slices in the thin sections. (B) Case 1: elongated grains are well-organized in the individual slices but show more variability of local mean trends (high strike sinuosity). Case 2: elongated grains are poorly organized in individual zones, but have less variability of local mean trends. Both cases give the exact same rose diagram, with identical overall trend and H-index. 77

Figure 2.15 The spicule lengths are grouped into classes with 50-micron increment. In some cases, two classes or more are merged until the combined frequency (n spicule) is at least 20. The spicule data in a class must originate from multiple slices to prevent locality bias. For each length class, the H-Index was calculated and plotted against the class median of spicule length. The results of these procedures show that longer spicules are better aligned compared to the shorter counterparts. These observations are true for uncorrected (Fig. 14A) and dip-corrected (Fig. 14B) H-index. In sample B2 [BED] and C2 [BED], the H-index seems to flatten as the length groups approaches maximum.....80

Figure 2.16 (A) Spicule length to H-index cross-plots, sorted by matrix types: The argillic groups show higher trendline positions compared to the micritic groups. The separation is very subtle in sample B1[BED], likely due to its lower clay content (lack of clay-rich packstone). This observation indicates that H-index is dependent not only on grain length, but also the presence of clay. (B) Dip-corrected H-index distributions from individual slices: The inherently high trendline position of argillic groups are counterbalanced by their relatively lower overall lengths. As a result, there is no significant difference in H-index distribution mean between argillic and micritic groups. 81

Figure 2.17 (A) Key features of microfractures in sample A: poorly-defined margins, devoid of fractured grains, filled with sediments instead of calcite cement, and localized upstanding spicules along the fracture walls. (B) Interpreted key features of microfractures in sample A. (C) An example of necking and tapered edges in sample C that evidenced of non-brittle, pre-lithification deformation. (D) Schematic diagram showing the stages of non-brittle failures in sample B and C.....83

Figure 2.18 (A) Original interpretation of the Cutoff MTD paleotransport: The fold axes and shortening lineation methods are in agreement, but the result from extensional lineation method differs significantly. (B) Alternative interpretation of the Cutoff MTD paleotransport: Fold axes, fold axial plane,

shortening lineation, extensional lineation, and grain-fabric alignment methods are now in unison.....86

Figure 2.19 Illustration of anisotropy in elongated micro-grains: We assume that the property of interest to a certain direction (λaθ) can be represented with bidirectional vectors. The left figure depicts a property that grows stronger toward the long axis. The right figure illustrates a property that grows stronger toward the short axis. (B) This figure illustrates how the proportion of elongated micro-grains (anisotropic components) and R2 (degree of orientedness) control the shape of anisotropy. The resultant shape of anisotropy is assumed to be the aggregate of contributions from isotropic (orange circles) and anisotropic components. 87

Figure 2.20 (A) Three-dimensional model of spicule orientations: the short axes of spicules are perpendicular to microbeds. If the microbed is tilted, the spicules are also tilted, such that the plunge of each spicule grain approaches the apparent dip of the microbed. Their long axes are parallel to the strike of isoclinal microfolds and transverse to the strike of flow-parallel microfractures / microfaults. Thin sections transverse to the dominant spicule alignments exhibit shorter apparent spicule length. (B) Outcrop Scale: the strikes of isoclinal folds are parallel to isoclinal microfolds and perpendicular to flow-parallel microfractures / microfaults. This allows for upscaling of grain-fabric alignments from microscopic to localized outcrop scale. (C) seismic scale: the strikes of isoclinal folds are likely parallel to the strike of compressional ridges, and transverse to the strike of conjugate extensional fractures/faults. This allows for upscaling of grain-fabric alignments from outcrop to localized seismic scale. 90

LIST OF TABLES

Table 1.1 Data Recapitulation..... 12

Table 1.2 The summary of Root Mean Square error of plane - point arrays..... 21

Table 2.1 Summary of Data Availability: All thin sections in this table are in cross-polarized light. Cartoons to the right illustrate the plane orientations of strike-parallel and strike-perpendicular thin sections..... 57

Table 2.2 Summary of Spicule Abundance 73

Table 2.3 Long- to Short-axis Percentile-Percentile Ratios..... 74

ACKNOWLEDGEMENTS

Two and a half years have passed since the first time I set foot in the United States. I am fascinated by how much I have grown in terms of personality and knowledge; thanks to the world-class education at Mines, which I value for the rest of my life. I dedicate this page to people and entities whose supports made all my achievements possible.

I was accepted to Mines by Dr. Lesli Wood into her consortium, Sedimentary Analogs Database (SAnD), and was immediately taken under Dr. Zane Jobe's care in the Central of Research Excellence (CoRE). In this opportunity, I would like to acknowledge all the privileges I received from Dr. Zobe and CoRE, including but not limited to: helpful colleagues, awesome computer, private workspace, research grants, and weekly lunch meeting. The presence of Dr. Jobe in the office (over 40 hours a week) is the most important factor that allowed me (and others) to persist through hard times. Thank you so much for hosting me! I also highly appreciate Dr. Wood's invaluable insight in my research, as well as all the helps she provided. I offer my deep gratitude to my thesis committees: Rick Sarg, Bruce Trudgill, Sebastian Cardona, and Gregory Hurd; as well as an honorable mention: Dr. Mary Car.

Next, I would like to thank my main sponsor, *Lembaga Pengelola Dana Pendidikan* (LPDP), who immensely funded my study here at Mines. Thanks for being the top-notch, role-model government organization, and thanks for being the beacon of hope for the country. I would also like to recognize my research sponsors: RMAG, AAPG, and the Bartshe Grant.

Finally, I want to cherish my parents and siblings for their indirect supports, all my friends here at CoRE and SAnD, my classmates, my gym buddies, my field summer camp students, my roommates, and all the nice people here in Golden. Thanks for having me!

Hanaga Simabrata

CHAPTER 1

CHARACTERIZATION OF VERTICAL SEGMENTS IN MASS-TRANSPORT DEPOSITS: THE CUTOFF FORMATION, PERMIAN BASIN, TEXAS

1.1 Abstract

Recent studies suggest that mass-transport deposits (MTDs) are vertically compartmentalized either by amalgamation of successive mass failures or internal shear surfaces within a single event. These compartments (i.e., segments) record important information about MTD emplacement and also strongly affect formation heterogeneity in the subsurface. While MTD segments have been documented in outcrop and seismic data, a comprehensive study on how to predict vertical MTD compartmentalization in the subsurface, especially at sub-seismic scale, are still lacking. Our research focuses on (1) defining segment architectures, (2) delineating recognition criteria (by simulating borehole data) to identify vertical segments in MTDs, and (3) discussing their genetic origin and implications for subsurface prediction.

MTDs of the Cutoff Formation are vertically compartmentalized by termination surfaces that are traceable for several kilometers. We utilized drone photogrammetry, conventional mapping, measured sections, and sample analysis (i.e., thin section & XRF) to characterize the vertical contrasts of deformation styles and lithofacies between segments, as well as laterally within segments. Our results show that the area of interest is compartmentalized into at least three segments. A shear zone (damage zone) is formed around the segment contacts, which further compartmentalize the outcrop into several sub-segments. Our research indicates that

lithofacies contrasts can only resolve segments, while the change of microstructure styles and deformation orientation are more reliable in recognizing sub-segments. We conclude that all criteria must be used in conjunction to confidently identify vertical segments (and sub-segments) in MTDs from borehole data.

The results of this study can help the prediction of vertical compartmentalization and the lateral continuity (or lack thereof) of MTD segments from wellbore data. The variability of segment (and sub-segment) characteristics and their associated termination surfaces in MTDs can affect subsurface anisotropy, and can act as barriers or buffers to fluid flow in the subsurface, which are important factors in formation evaluation.

1.2 Introduction

Mass-transport deposits (MTDs) are the products of cohesive gravity flows emplaced due to slope instability, and are important constituents of marine and lacustrine stratigraphic successions (Posamentier and Walker, 2006; Sammartini et al., 2019). MTDs may occur in shelf margins (Moscardelli and Wood, 2016), the upper and middle part of continental slopes, or locally in the proximity of salt domes (e.g., Gamboa and Alves, 2015), volcanoes (e.g., Clare et al., 2018), and the flank of channel-levee systems (e.g., Posamentier, 2003; Ortiz-Karpf et al., 2015). MTD facies encompass a wide process continuum, including slide, slump, and debris flow (often with m- to km-scale rafted blocks), and associated co-genetic turbidity current (Posamentier and Martinsen, 2011). The areal extent of such deposits can range from 0.3 to more than 100.000 km^2 , with thicknesses of less than 1 meter to more than 1000 meters (see Moscardelli and Wood, 2016).

Multi-scale deformational features make MTDs unique compared to sediments from other depositional processes. These multi-scale deformation in MTDs can pose geohazard risk in deep-

sea drilling (Sun et al., 2017; Sun and Alves, 2020), and can influence sealing capacity (Dugan, 2012; Cardona et al., 2020), reservoir quality (Allen et al., 2013; Gamboa and Alves, 2015), and reservoir compartmentalization issues. At the mm-scale, MTDs undergo fabric modification that includes consolidation and densification (Shipp et al., 2004; Sawyer et al., 2009; Dugan, 2012), rearrangement of clay minerals and pore structures (Day-Stirrat et al., 2013), assimilation of the underlying sediments by basal-shear processes (Cardona et al., 2020), and alignments of grain fabric (Simabrata et al., part B). MTDs can develop millimeter to meter-scale fractures, faults, and folds that are embedded in larger fold-thrust systems (e.g., Woodcock, 1976; Amerman et al., 2011; Alsop and Marco, 2014) and also in individual rafted blocks (Alves, 2015; Gamboa and Alves, 2015). At a much larger scale, seismic studies reveal lateral compartmentalization of MTDs by longitudinal shear surfaces or zones that may separate the emplaced body into multiple flow units with distinct seismic facies and deformation structures (e.g., Bull et al., 2009; Steventon et al., 2019; Nugraha et al., 2020). Vertically compartmentalized MTDs are recognized from continuous to faint, horizontal to quasi-horizontal internal reflectors that separate the MTD bodies into packages of distinct seismic characters, and may also emerge upward as thrust faults (e.g., Schnellmann et al., 2005; Ogata et al., 2014; Gamboa and Alves, 2015; Le Goff et al., 2020). In outcrop studies, the vertical compartmentalization of MTDs can manifest as stack of deformed units with distinct rheological and/or lithological characteristics, e.g., debris flow deposits overlying contorted intervals (e.g., Van Der Merwe et al., 2011; Ogata et al., 2014; Jablonská et al., 2018), or simply as laterally extensive termination surfaces that dissect MTD bodies into several segments (e.g., Amerman et al., 2011; Le Goff et al., 2020). One or a combination of the following processes may cause vertical compartmentalization in MTDs: (1) pulses of retrogressive failures from unstable headwall scarps (Ogata et al., 2014;

Walker et al., 2021), (2) partial remobilization of initial failure (Ogata et al., 2014), (3) stacking of coeval MTDs triggered by regional events (e.g., earth quake) (see Strasser et al., 2013; Kremer et al., 2017; Praet et al., 2017; also see Sammartini et al., 2019), (4) a single mass-failure that deforms the underlying strata (Schnellmann et al., 2005; Van Der Merwe et al., 2011), (5) partial flow transformation (Haughton et al., 2009; Talling et al., 2012; Jablonská et al., 2018) and, (6) vertical partitioning during emplacement by internal shear surfaces (Le Goff et al., 2020).

Although the vertical compartmentalization of MTDs have been documented widely in outcrops and seismic, these phenomena are recognized largely because the data resolution and quality allow for direct identification. Our research emphasizes on testing indirect criteria to reliably predict the existence of vertical segments in MTDs. We utilize outcropping MTDs of the Cutoff Formation to demonstrate segments with differing lithofacies characteristics and deformation styles, bounded by termination surfaces, and how the segments correlate over several hundred meters (i.e., the segment architecture). We discuss the origin of vertical compartmentalization in MTDs, the implication on subsurface anisotropy, and how termination surfaces that bound MTD segments can act as barriers or baffles to fluid flow.

1.3 Geological Context

1.3.1 Regional

The Permian Basin is the foreland basin related to the Marathon-Ouachita Orogenic Belt that resulted from the collision between Laurentia and Gondwana Continents during late Mississippian time (Galley, 1958; Horak, 1985; Yang and Dorobek, 1995). During late Pennsylvanian basement uplift divided the Permian Basin into the Delaware Basin to the west and the Midland Basin to the east, with the Central Basin Platform remaining topographically

high (Hills, 1984a; Horak, 1985; Yang and Dorobek, 1995) (Fig. 1.1A). This basin configuration facilitated carbonate platform, shallow-marine siliciclastic, to deep-water depositional systems to thrive until the cessation of subsidence at the end of Permian (Yang and Dorobek, 1995). The Cutoff Formation was deposited on the antecedent Leonardian shelf margin of the northern Delaware Basin during late Leonardian regional transgression and early Guadalupian regression/progradation (Kerans and Fitchen, 1995; Hurd et al., 2016) (Fig. 1.1B). MTDs dominate the upper portion of the Cutoff Formation, with the thickness and deformation intensity generally increase basinward (Amerman et al., 2011; Hurd et al., 2016).

1.3.2 The Cutoff MTDs

The Cutoff MTDs exposed along the Guadalupe and Delaware Mountains are well-constrained paleogeographically and have been thoroughly mapped in both proximal (Hurd et al., 2016) and distal locales (Amerman et al., 2011) (Fig. 1.2A). The lithofacies comprising the Cutoff MTDs are stacked millimeter- to centimeter-thick, mixed carbonate-siliciclastic wackestones to packstones, with abundant fine-grained bioclasts (Amerman et al., 2011; Hurd et al., 2016; Simabrata et al., part B). Individual beds often host internal thin packages (herein microbeds), most likely turbidites and hemipelagites that were deposited prior to the emplacement of Cutoff MTDs (Hurd et al., 2016; Simabrata et al., part B). Common MTD-related structures include meter- to decameter-scale open-to-recumbent folds and millimeter- to centimeter-scale, bed-restricted microstructures (e.g., microfractures / tension gashes, microfolds, microfaults, microboudins) that often deform the microbeds (Amerman et al., 2011). These microstructures form lineations when intersected by bedding planes (Amerman et al., 2011). Elongated bioclasts (primarily sponge spicules) in the Cutoff MTDs exhibit grain-fabric alignments, whose degree of orderliness increase with grain length and the presence of clay

(Simabrata et al., part B). This multi-scale deformation in the Cutoff MTDs is likely co-genetic because their trends are coherent (see Simabrata et al., part B). The overall paleotransport direction of the Cutoff MTDs inferred from folds, microstructure lineations, and grain-fabric alignments vary slightly from NNW- SSE to NNE – SSW (see Amerman et al., 2011; Simabrata et al., part B). Using data from Amerman et al., (2011) and Hurd et al., (2016), we estimate that the length of the Cutoff MTDs is at least 14 km (slope-parallel measurement, i.e., NW - SE) to about 21 km (transport-parallel measurement, i.e., NNE - SSE) (See Fig. 1.2A). Using scaling relationships derived by Moscardelli and Wood (2016), this length range predicts an area of 93 km^2 to 190 km^2, which is comparable to, if not larger than, the Bone Spring MTD of the Delaware Basin (see Allen et al., 2013) and the Upper Leonard MTD of the Midland Basin (see Bhatnagar et al., 2019) (Fig. 1.2B and 1.2C).

Outcrops of the Cutoff MTDs are compartmentalized by termination surfaces that physically manifest as thin, fissile layers that truncate both underlying and overlying deformed beds, are generally unfolded and can be easily identified with naked-eye observations. These surfaces are typically low-dipping (0 - 30^0), can be localized or laterally extensive, and sometimes compartmentalize the MTD into segments with distinct deformation styles and lithofacies types (see Amermasn et al., 2011; Hurd et al., 2016). These surfaces have been interpreted as boundaries between different MTD events (see Amerman et al., 2011; Hurd et al., 2016), but could also represent internal shear surfaces within a single event (cf. Le Goff et al., 2020). Some major termination surfaces are overlain by seemingly undisturbed, discontinuous, organic-rich carbonate mudstone intervals (up to ~2m), and have been interpreted as draping infill that separate mass-failure events (Amerman et al., 2011; also see Armitage et al., 2009).

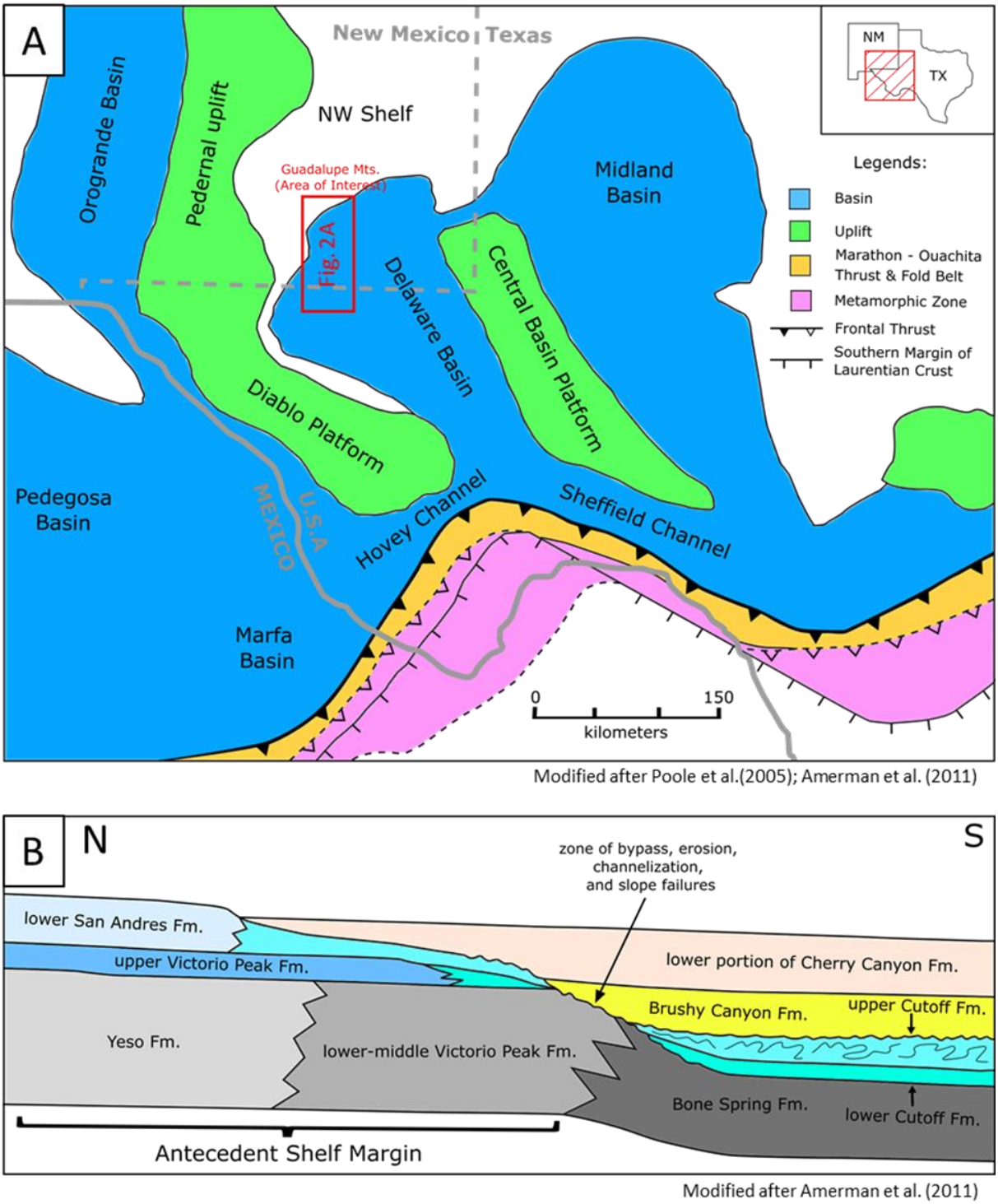

Figure 1.1 (A) Basin configuration: the Permian Basin consists of the Delaware Basin to the west and the Midland Basin to the east, separated by the Central Basin Platform. The area of interest (Guadalupe Mts.) is signified by the red rectangle near the northwestern margin of the Delaware Basin. (B) Simplified illustration of slope-to-basin depositional systems of the Cutoff Formation.

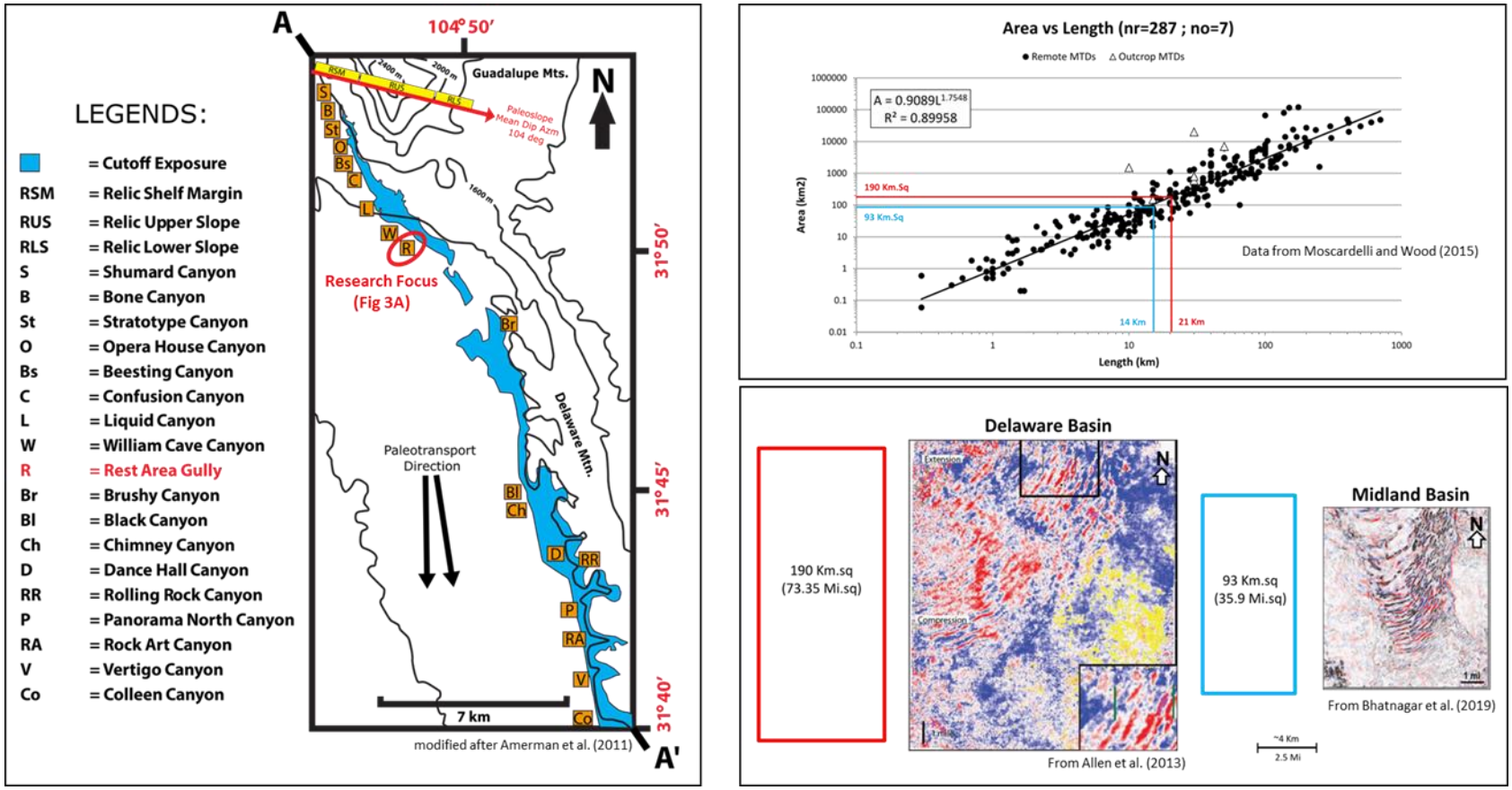

Figure 1.2 (A) Exposure map of the Cutoff Formation, Guadalupe Mountains: The research focus is in the Rest Area Gully Locality where the Cutoff MTDs exhibit compartmentalization. (B) The estimated size of the Cutoff MTDs: The lengths of the Cutoff MTDs is at least 14 km and 21 km according to slope- and transport-parallel measurements, respectively. Applying the morphometric relationship compiled by Moscardelli and Wood (2015) to the estimated MTD lengths, we estimate that the area of the Cutoff MTDs is at least 93 km^2 to 190 km^2, which measures are comparable to, if not larger than, the MTDs documented in the Delaware Basin (Allen et al., 2013) and the Midland Basin (Bhatnagar et al.,2019).

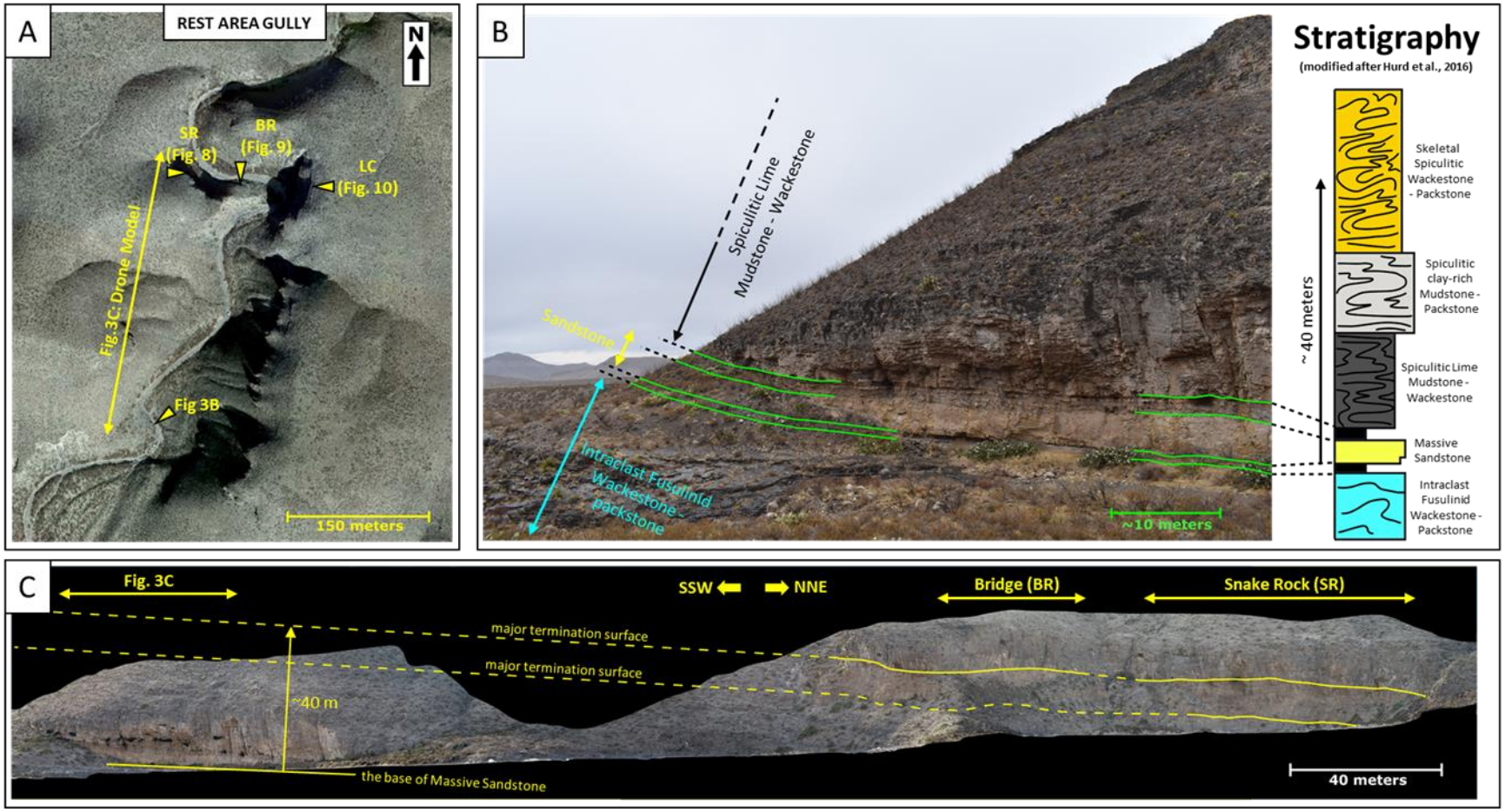

Figure 1.3 (A) Rest Area Gully: This research focuses on two cliff-face outcrops called Snake Rock (SR) and Lunch Cliff (LC). About 200 meters downstream from the SR and LC is the location of massive sandstone outcrop in figure 3B. (B) The units of interest overlay the massive sandstone unit (~3m), which is interpreted as high-density turbidite (non-MTD). The bedding orientation of this massive sandstone likely reflects the depositional dip. (C) Our drone model suggests that the dip of termination surfaces in the area of interest are similar to that of the massive sandstone.

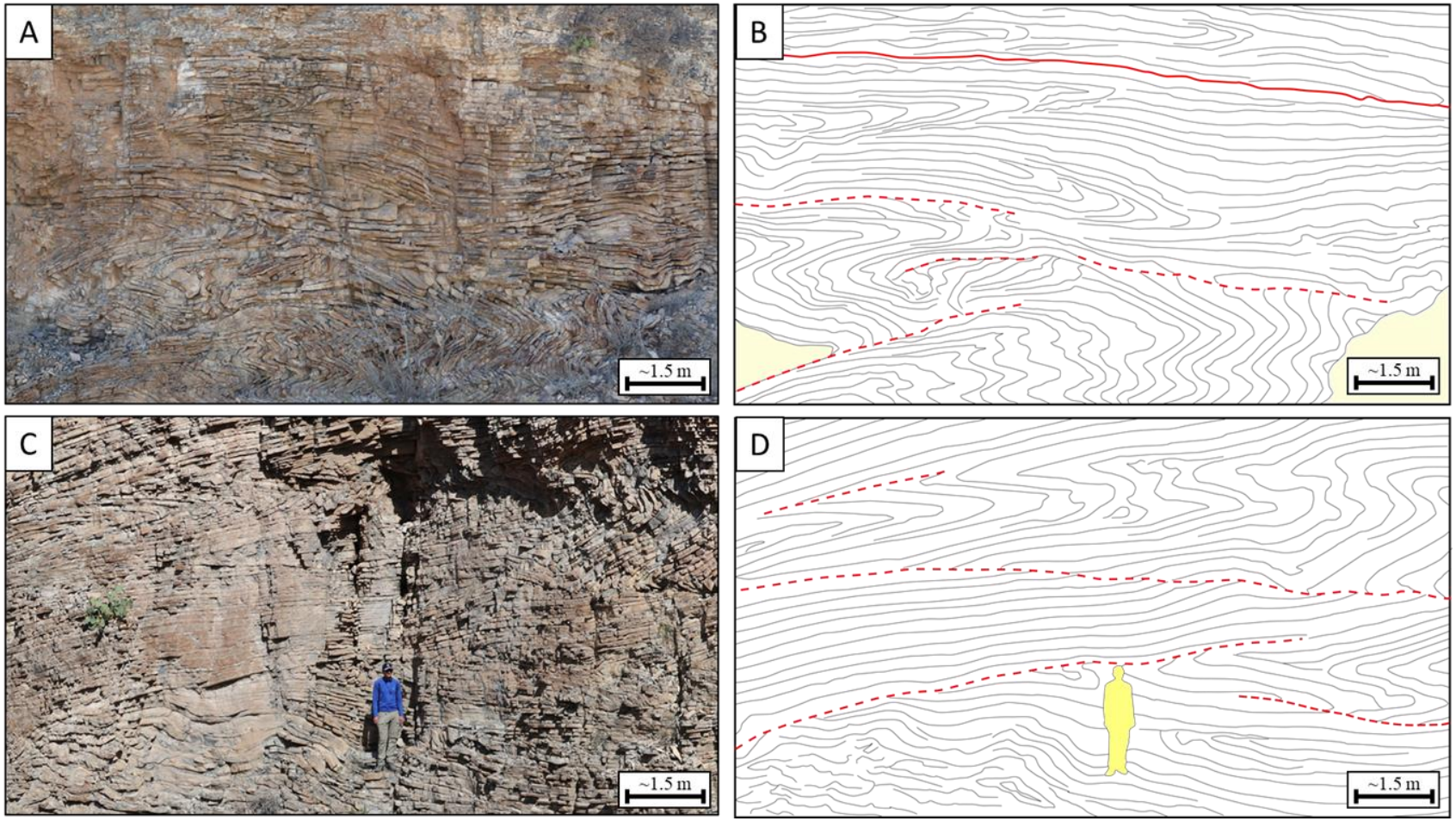

Figure 1.4 (A) Termination surfaces and complex folding in Snake Rock (uninterpreted). (B) Interpretation of figure 4A. (C) Termination surfaces and complex folding in Lunch Cliff (uninterpreted). (D) Interpretation of figure 4C.

1.3.3 Area of Interest

This research focuses on two main cliff-face outcrops in the Rest Area Gully locality (herein area of interest) (see Fig. 1.2A) – termed Snake Rock (SR) and Lunch Cliff (LC), and one outcrop that acts as a bridge (BR) between SR and LC (Fig. 1.3A). The outcrops expose several segments of the Cutoff MTDs that are separated by termination surfaces traceable across the outcrops, as well as other meter- to decameter-scale deformations, predominantly complex folds associated with minor termination surfaces that are laterally discontinuous (more in section 4) (Fig. 1.4). Internal truncations within fold limbs are also common, caused by high-intensity folding. The lithology generally consists of alternating resilient and fissile, mud-sized carbonate and siliciclastic composition (Fig. 1.4A, 1.4C). The fissile beds contain more clay-rich laminae, while the resilient beds are more carbonate rich and contain deformed microbeds that enable detailed field descriptions, especially in conjunction with thin section analysis. Hurd et al. (2016) reported a total of ~50 m of highly contorted units in the study area, which are underlain by turbiditic sandstones and shales (Fig.3 B and C). The orientations of major termination surfaces mapped from drone photogrammetry are similar to that of the massive sandstone interval, which suggests that these surfaces are quasi-parallel to original depositional dip (Fig. 1.3C) (the regional dip is 4° to the east).

1.4 Methods

We focus on the sub-seismic scale contrasts and/or similarities between MTD segments, including the lithofacies, microstructure types, and deformation orientation. The position of termination surfaces and the corresponding MTD segments were mapped in the field and transferred to photomosaics and digital outcrop models produced by drone photogrammetry. Detailed graphic logs record bed thickness, bed geometry (e.g., planar horizontal, folded),

microstructure types and lineation trends, fold axes, hand samples for thin section and XRF analyses, as well as termination surface locations (Table 1).

Table 1.1 Data Recapitulation

No	Item	Locations		Unit
		Snake Rock	Lunch Cliff	
1	Measured Section	5.4	10.5	Meters
2	XRF Samples (Resilient Beds)	39	56	
3	XRF Samples (Fissile Beds)	27	17	
4	Thin Sections	25	6	
5	Fold Axes	91	75	
6	Microstructure Lineations	287	111	
7	Drone Image	320 x 208		Square Meter
8	Photomosaic	48 x 20	125 x 40	Square Meter

1.4.1 Lithofacies

Since textural characteristics were not readily visible in the field, we documented only the weathering profile of beds, i.e., resilient vs. fissile, and we applied the natural outcrop color in the measured section log. The detailed lithofacies and microstructure characteristics were described from thin sections that were cut perpendicular to the bedding plane (also see Simabrata et al., part B). Furthermore, we also collected hand samples every ~20 cm while logging for X-ray fluorescence (XRF) analyses. The XRF samples were polished in order to expose a fresh, flat surface for analysis using a Bruker Tracer 5G at 15 and 50 kV with a Helium purge.

The XRF analyses in this research follow the premise that the primary elemental constituents in the area of interest are Calcium and Silicon, which are inversely proportional to one another ($R^2 = 0.94$, n = 138) and make up about ~40% of the total weight combined (Fig. 1.5A). We also include the prediction of relative clay abundance using the sum of Potassium,

Titanium, and Iron, which are demonstrably reliable as clay indicator when compared to thin sections (Fig. 1.6). In addition, the proportion of Potassium, Titanium, and Iron in our samples display excellent linear-proportional relationships that suggest these elements are largely dependent on each other (R^2 = 0.85 – 0.92, n = 138) (Fig. 1.5B, 1.5C), except for few outliers – e.g., Iron may come from pyritization instead of clay (see Fig. 1.5C). Silicon also exhibits poor correlation with clay indicator (R^2 resilient = 0.28, n = 94; R^2 fissile = 0.42, n = 42) (Fig. 1.5D), due to disruptions by silicification (especially in resilient beds), the abundance of siliceous bioclasts (e.g., radiolarians), or cannibalization by other diagenetic processes. We recognize that XRF measurements investigate only a small zone on a target bed, and hence not necessarily representative of the entire bed; thus, we also analyze the XRF data grouped by segment (using box plots) to more generally summarize inter-segment variability.

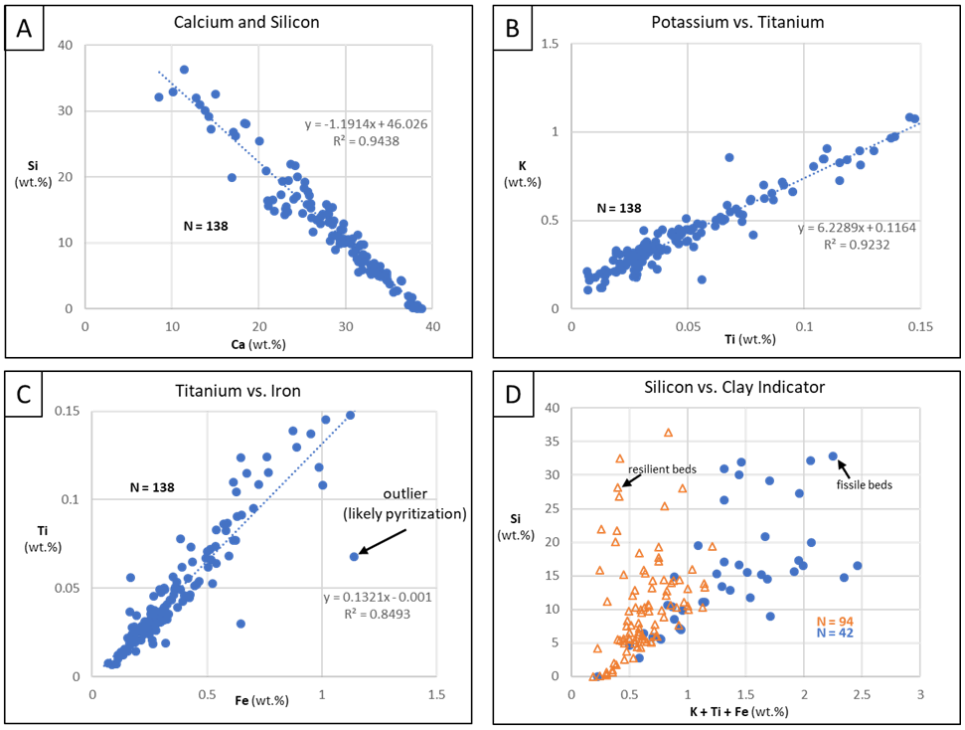

Figure 1.5 (A) Calcium vs. Silicon. (B) Potassium vs. Titanium. (C) Titanium vs. Iron. (D) Clay indicator vs. silicon.

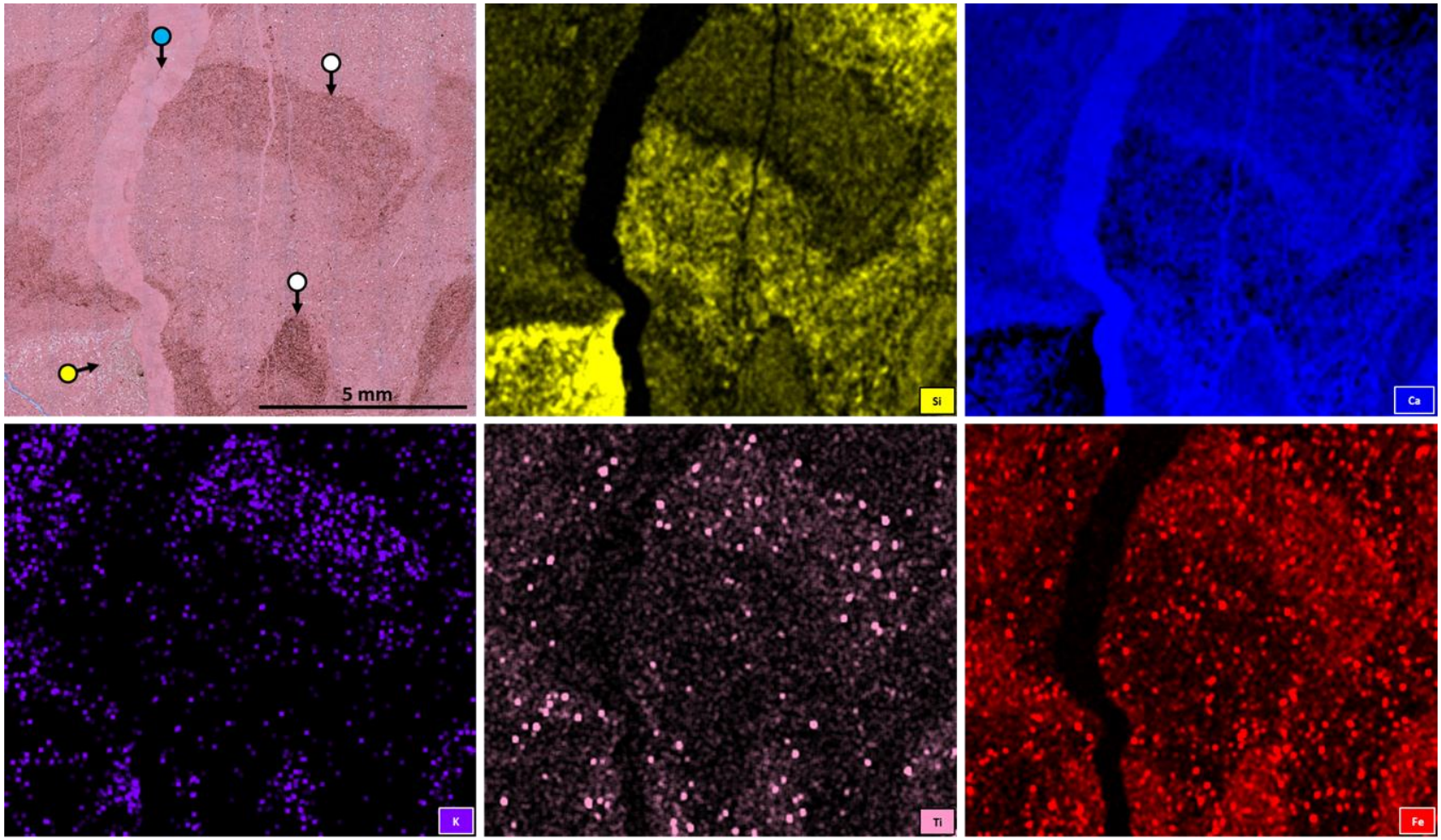

Figure 1.6 Thin section (top right) and composition masp in the same location (rest of the figures): Clayey to clay-rich packstone microbeds (white pin) contain high potassium (K), titanium (Ti), and iron (Fe). Highly silicified packstone microbeds (yellow pin) have relatively higher silicon (Si). The blue pin is calcite-cemented post-lithification fracture. The thin section location is given in Figure 6.

1.4.2 Microstructure Types and Deformation Orientations

All orientation measurements and interpretations in this research are treated as bidirectional / axial data (see Amerman et al., 2011; Simabrata et al., Part B). Microstructure types were recorded in the graphic log to record vertical variability, and microstructure lineations were measured from exposed bedding planes, with the trends displayed in 0° – 180° logs; because the orientations are bidirectional, a 0-180° log summarizes the measuremet. Some microstructure types and lineation trends were also extracted from thin sections oriented perpendicular and parallel to the bedding plane, respectively. Lineation trends and fold axes outside of the measured section locations were also collected (termed 'projected lineation' and 'projected folds') and plotted using rose diagrams. We interpret MTD paleotransport directions that are perpendicular to the mean axes of folds (Alsop and Weinberger, 2020), perpendicular to the mean trend of microfold and microboudin lineations, and parallel to the mean trend of microfracture lineations (Simabrata et al., part B). In addition, the degree of orderliness of fold axes and microstructure lineations are quantified using a 0 to 1 continuum scale called the H-index, where 0 corresponds to completely chaotic trends, while 1 corresponds to perfectly parallel trends (see derivation of H index in Simabrata et al., part B).

1.5 Result and Interpretation

1.5.1 MTD Architecture

Lunch Cliff (LC)

Lunch Cliff is divided into segments A, C, and D, which are bounded by major termination surface LC 0 and LC 2, respectively (Fig. 1.7). Three major termination surfaces (LC -2, LC -1, and LC 1) are also documented above and below the contact of lithofacies A-C that result in sub-segments. The sub-segments exhibit some lateral thickness variability but their full lateral extent

is unknown. Minor termination surfaces can be quasi-parallel to the major surfaces, or of moderate to high dip magnitudes. The low-dipping, minor termination surfaces are interpreted as internal shear surfaces and/or intra-fold truncations. Some of the moderate- to high-dipping minor surfaces are detached from major termination surfaces (e.g., southern part of LC 0 and LC 1), which we interpret as downslope-dipping thrust faults. The common folding styles are upslope-inclining folds (especially in segment C), recumbent folds, and sheath folds – which are concentrated inside the sub-segments.

Snake Rock (SR)

Snake Rock is divided into segments B, C, and D, separated by major termination surface SR 0 and SR 2, respectively (Fig. 1.8). Similar to Lunch Cliff, other major termination surfaces have been observed around the boundary of lithofacies B and C, forming sub-segments. Major termination surface SR -1 is truncated by SR 0, which indicates some lateral discontinuity of sub-segments. Minor termination surfaces with moderate to high dip are generally downslope-dipping, some of which are detached from the major termination surface SR 1 and are interpreted as thrust faults. Low-dipping, minor termination surfaces (almost parallel to the major termination surfaces) are less common. The prominent folding styles are upslope-inclining folds (typically in segment C), recumbent folds, and sheath folds, commonly associated with the sub-segments.

Bridge (BR)

The Bridge outcrop serves to clarify the relationship between segment A and B, which are found only in Lunch Cliff and Snake Rock, respectively. The Bridge outcrop (see Fig. 1.3A for the location) shows that segment B piggybacks on segment A, and the major termination surfaces of segment B are likely truncated above LC 0 (Fig. 1.9A and 1.9B) (in this figure, SR -1

terminates on LC 0). Our drone model projection indicates that the contact of segment A-B is buried about 1.5 to 2 meters beneath the Snake Rock outcrop. Major termination surfaces in the Bridge outcrop are closely-spaced and are dominated by sheath folds and mylonite-like lenses, which indicates intense shearing (Fig. 1.9D). Furthermore, this outcrop also demonstrates interface-mixing phenomenon, where one segment is incorporated into another along the bounding termination surface (i.e., LC 0) (Fig. 1.9C and 1.9D). The interface-mixing phenomenon is likely similar to mixing of sediments in MTD basal shear zones (see Cardona et al., 2020).

1.5.2 Correlation

In order to assess the segment architectures and to compare the lithofacies and deformational characteristics laterally between Snake Rock and Lunch Cliff, a robust correlation must be established. However, unlike non-MTD sediments, there is no well-formulated method for intra-MTD correlation, owing largely to intense deformation. In this research, we employ the well-mapped major termination surfaces as boundaries for correlation, which by nature can be more mechanical rather than sedimentological. The procedure involves tracing the major termination surfaces as point arrays from drone image, such that the acquired x-y coordinates, as well as the elevations of the point arrays, can be converted into 3D planes via triangulation (Fig. 1.10A). Triangulations are carried on point arrays that best capture the 3D shape of the surface, in this case, the Lunch Cliff is the most suitable because the outcrop is geometrically more curved than Snake Rock (see Fig. 1.10A). The 3D planes generated from the Lunch Cliff are then projected the point arrays of Snake Rock, and the plane to point errors are calculated using root mean square (RMS) method (Fig. 1.10B). The result of plane to point RMS errors are summarized in Table 2 (units in meters and the least RMS errors highlighted in green).

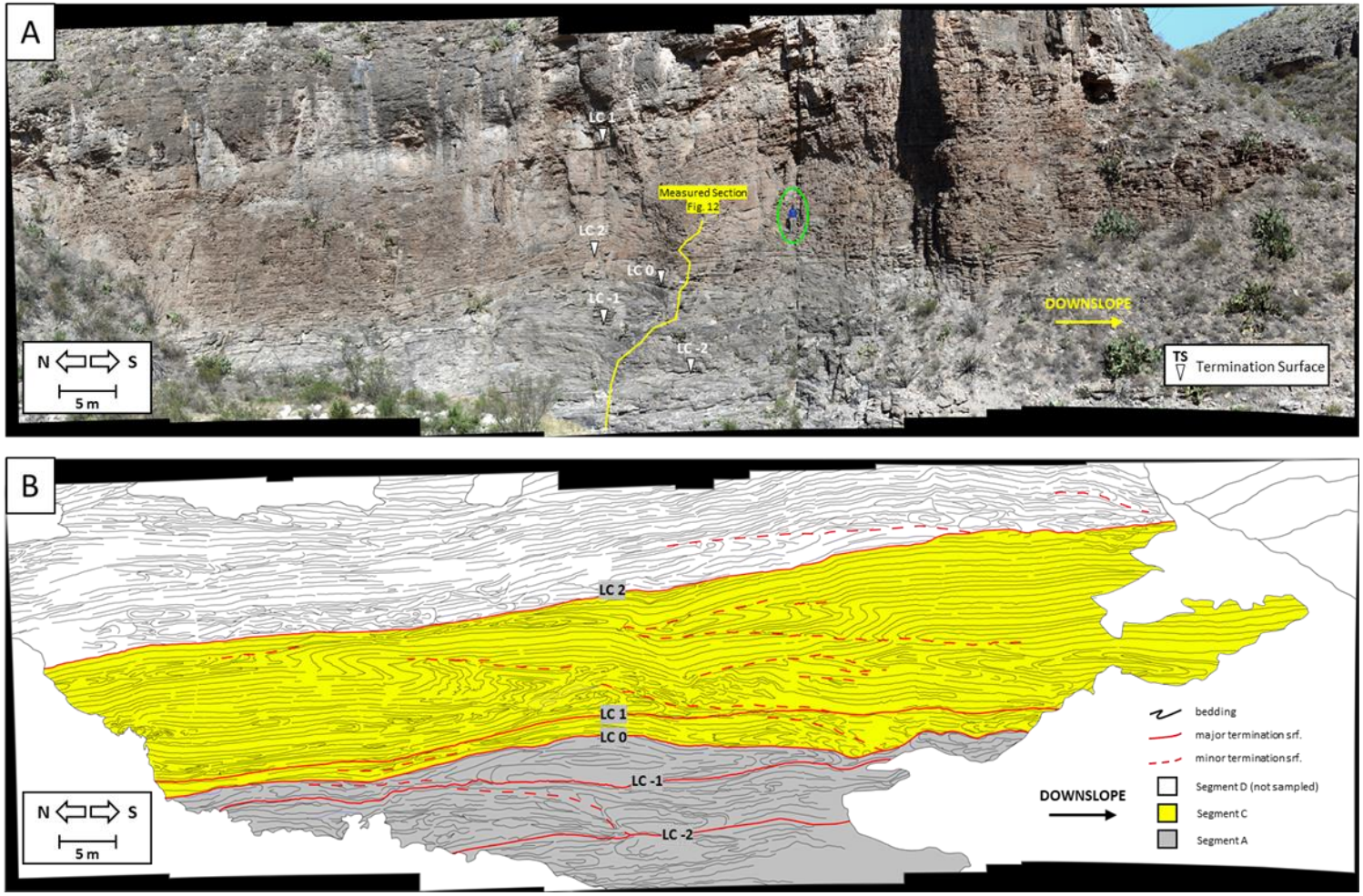

Figure 1.7 (A) uninterpreted Lunch Cliff outcrop: white arrows are the position of major termination surfaces. The yellow line is the location of measured section. The green circle is human for scale. (B) interpreted Lunch Cliff outcrop: Consist of segment A, C, and D (not sampled) that are bounded by major termination surfaces LC 0 and LC 2. Other major termination surfaces are observed around A-C segment contact, which result in closely-spaced sub-segments. Minor termination surfaces (dashed lines) can be high-dipping (thrust faults) and low-dipping (shear surfaces and intra-fold truncations). Some of the thrust faults are detached from the bounding termination surfaces, e.g., see the southern part of surface LC 0 and LC 1. Smaller intra-fold truncations are not shown here.

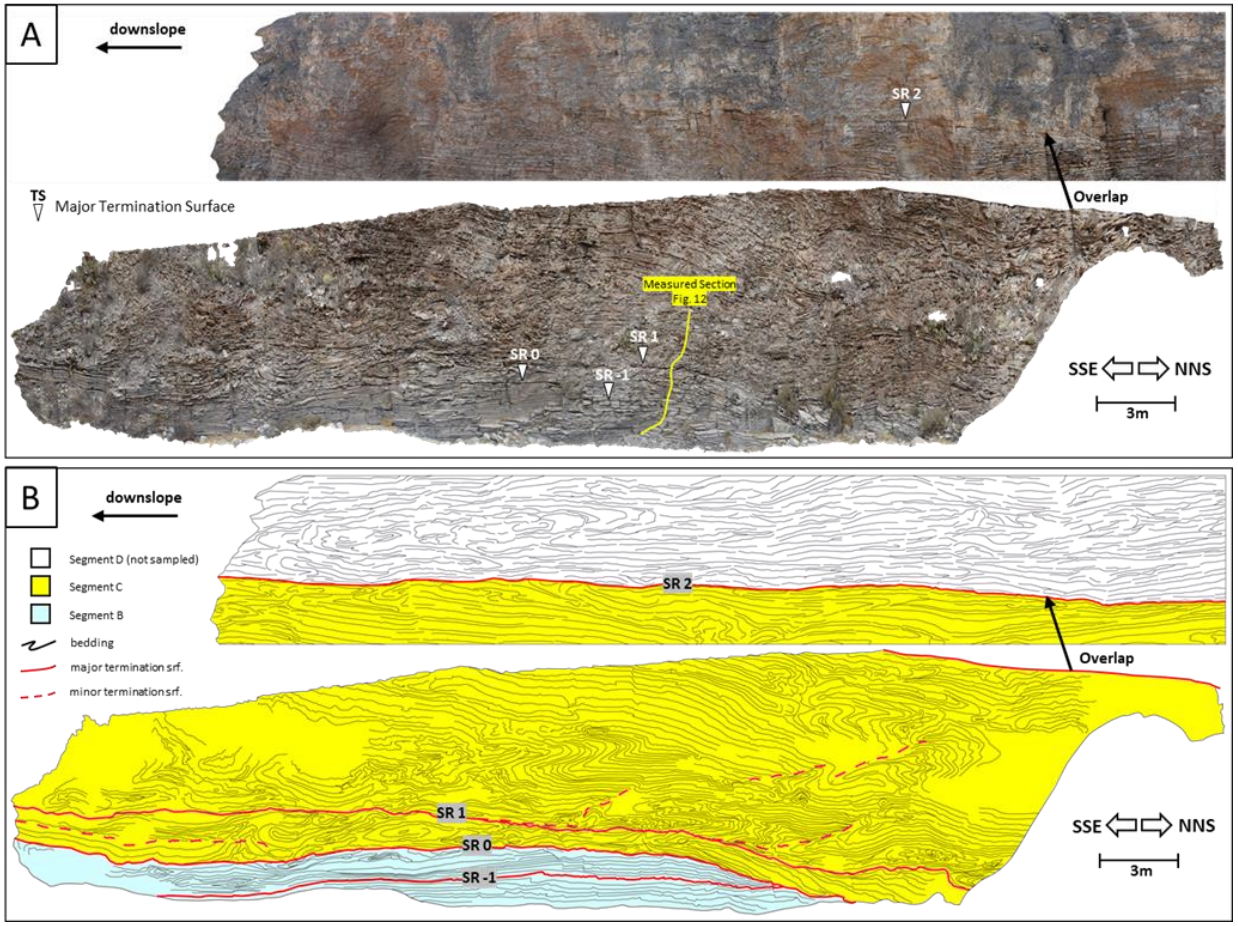

Figure 1.8 (A) uninterpreted Snake Rock outcrop: white arrows are the position of major termination surfaces. The yellow line is the location of measured section. The lower photomosaic overlaps with the upper one exactly at the uppermost termination surface SR-Top. (B) Interpreted Snake Rock outcrop: Consist of segment B, C, and D (not sampled) that are bounded by major termination surfaces SR 0 and SR 2. Other major termination surfaces are observed around B-C segment contact, which result in closely-spaced sub-segments. Minor termination surfaces (dashed lines) can be high-dipping (thrust faults) and low-dipping (shear surfaces and intra-fold truncations). Some of the thrust faults are detached from the bounding termination surfaces, e.g., see the northern part of surface SR 1. Smaller intra-fold truncations are not shown here.

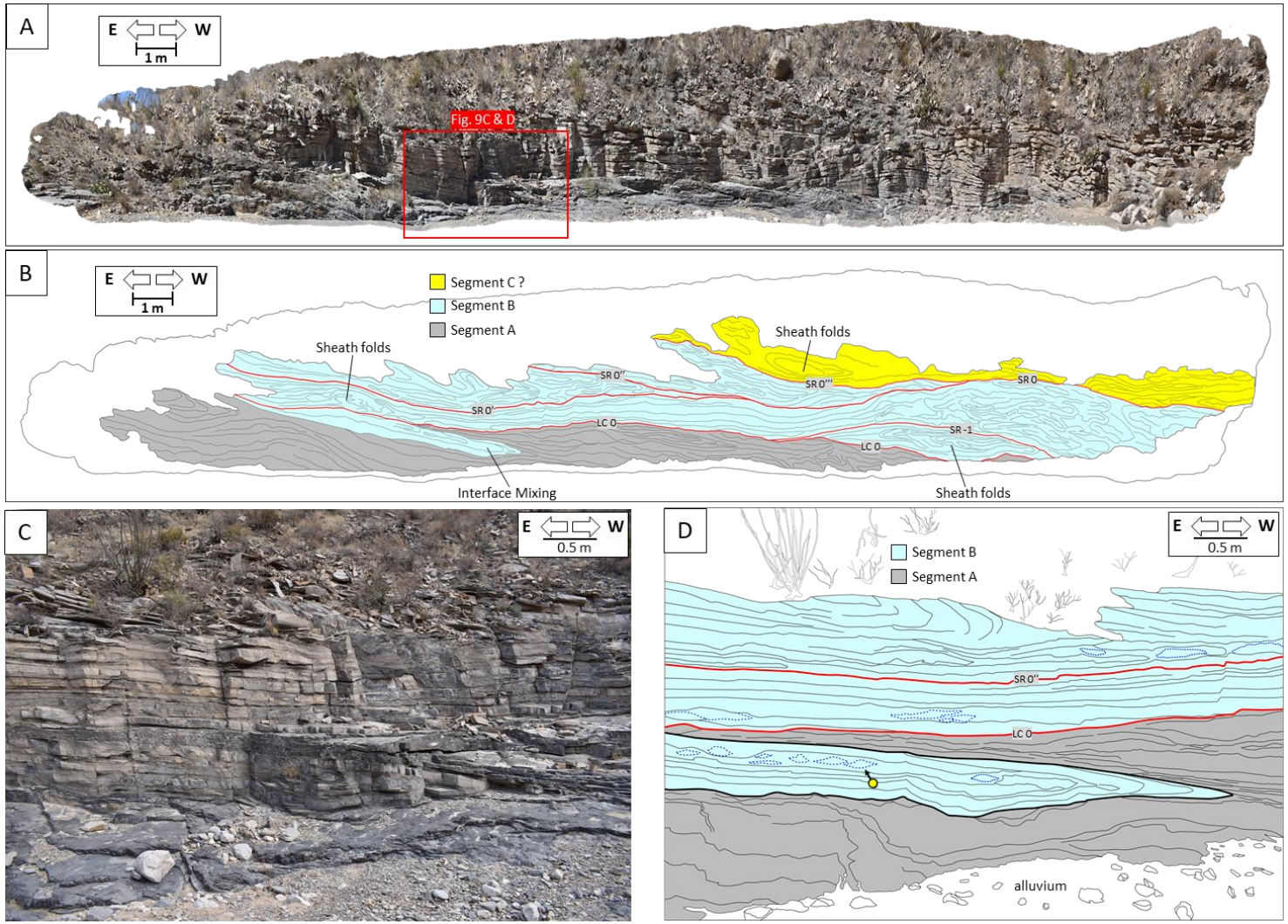

Figure 1.9 (A) Uninterpreted Bridge outcrop: Red rectangle highlights the zoom-in photo in Figure 9C and 9D. (B) Interpreted Bridge outcrop: Segment B piggybacks on segment A. Major termination surface SR -1 is truncated above LC 0. (C) Interface-mixing phenomenon (uninterpreted). (D) Interpretation of interface mixing: Segment B has been incorporated into segment A along major termination surface LC 0.

The statistical model suggests that the major termination surfaces in segment C of Snake Rock (SR 1, SR 2) and Lunch Cliff (LC 1, LC 2) are correlated within acceptable errors of 0.5 to 1 meter (Fig. 1.11, Fig 1.12). Segment C from both outcrops have similar thickness, i.e., ~ 8 - 10 meters, which is rather well-maintained laterally, and host folds that incline upslope, possibly accommodated by downslope-dipping thrust faults. Note that the spatial position between Snake Rock and Lunch Cliff (~150 meters away) is almost parallel to the strike of termination surfaces (dip: ~1° – 3°), and thus the likelihood of discovering the same surfaces across cliffs is very high. In contrast, while the statistical model also suggests the correlativity of major termination surfaces within segment A and B, the Bridge outcrop demonstrably shows that these surfaces are truncated on the A-B segment boundary (Fig. 1.11, Fig. 1.12). We interpret the sub-segments in the vicinity of segment margins as shear zone (damage zone). The resulting sub-segments are hereafter termed A1, A2, B1, B2, and so on, based the hosting segments and the spatial elevations (Fig. 1.11, Fig. 1.12).

Table 1.2 The summary of Root Mean Square error of plane - point arrays

			SNAKE ROCK (as point arrays)			
			Segment C		Segment B	
			SR 2	SR 1	SR 0	SR -1
LUNCH CLIFF (as planes)	Segment C	LC 2	1.017	10.251	12.251	13.058
		LC 1	10.022	0.509	1.618	2.406
	Segment A	LC 0	11.782	2.095	0.599	0.832
		LC -1	12.818	3.432	1.651	0.817

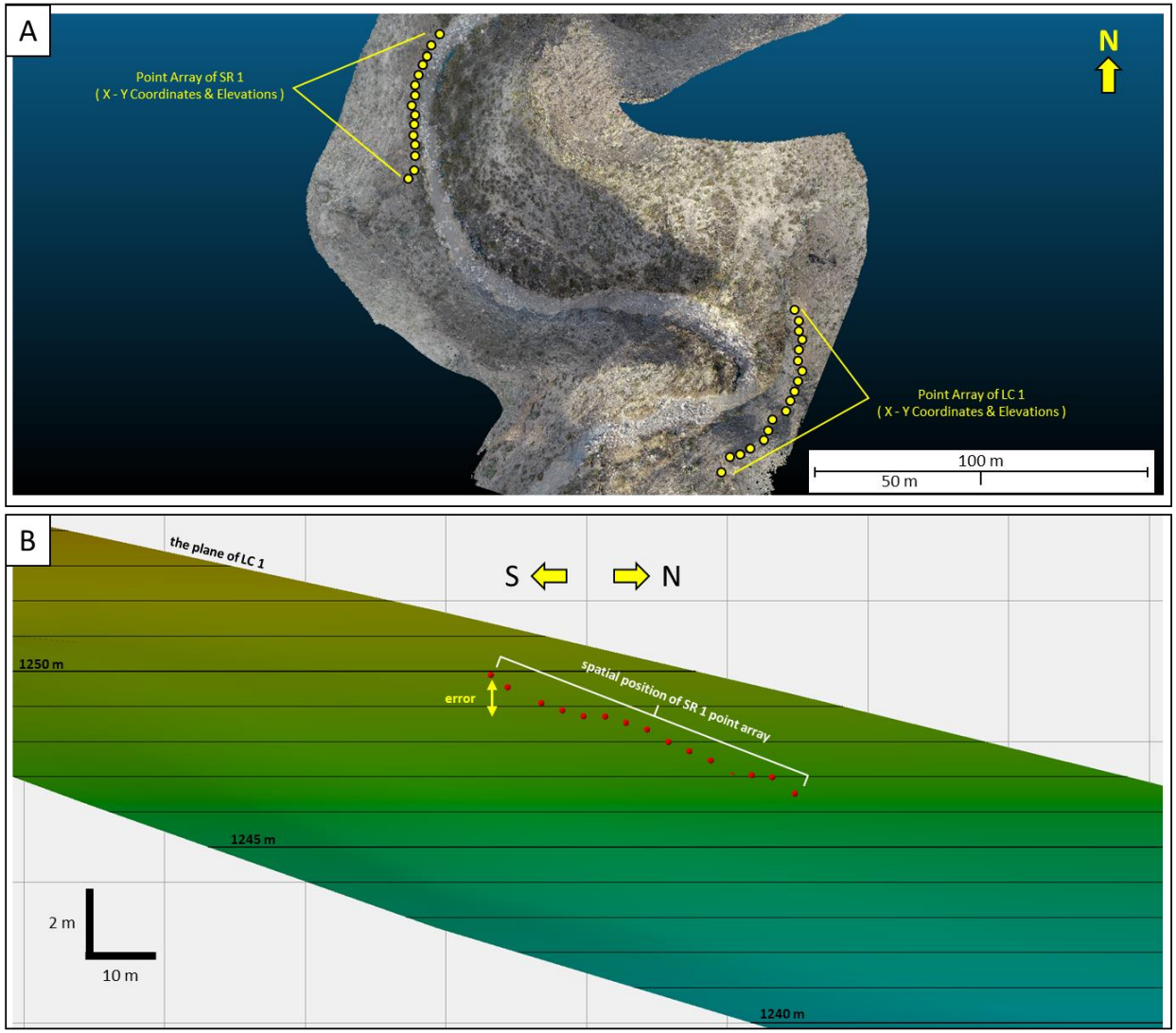

Figure 1.10 (A) examples of point arrays picked from the drone model. Point arrays in Lunch Cliff are more curved, owing to the shape of the cliff itself. This makes triangulation more suitable in Lunch Cliff. (B) The result of triangulations from Lunch Cliff are projected to Snake Rock point arrays, and the RMS error for each plane - point array pair.

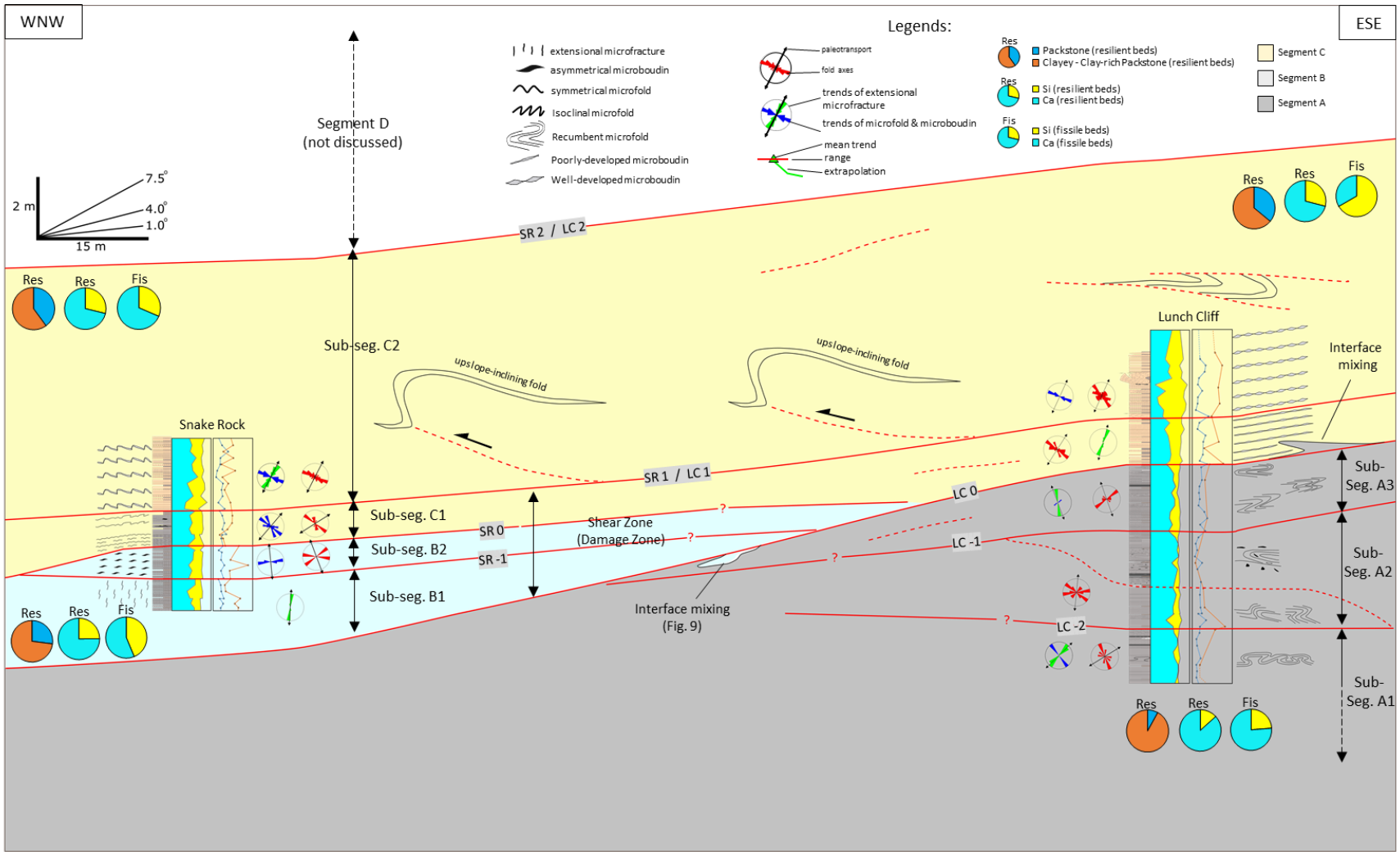

Figure 1.11 MTD architecture: The MTDs in the area of interest is divided into three segments based on their lithofacies, i.e., segment A, B, and C. The smaller segments formed around the contact between segments are referred as sub-segment A1, A2, B1, B2, etc., according to the hosting segments and the spatial elevations. The characteristic contrasts between segments and sub-segments are summarized in this figure, and are discussed in detail in the following sub-sections.

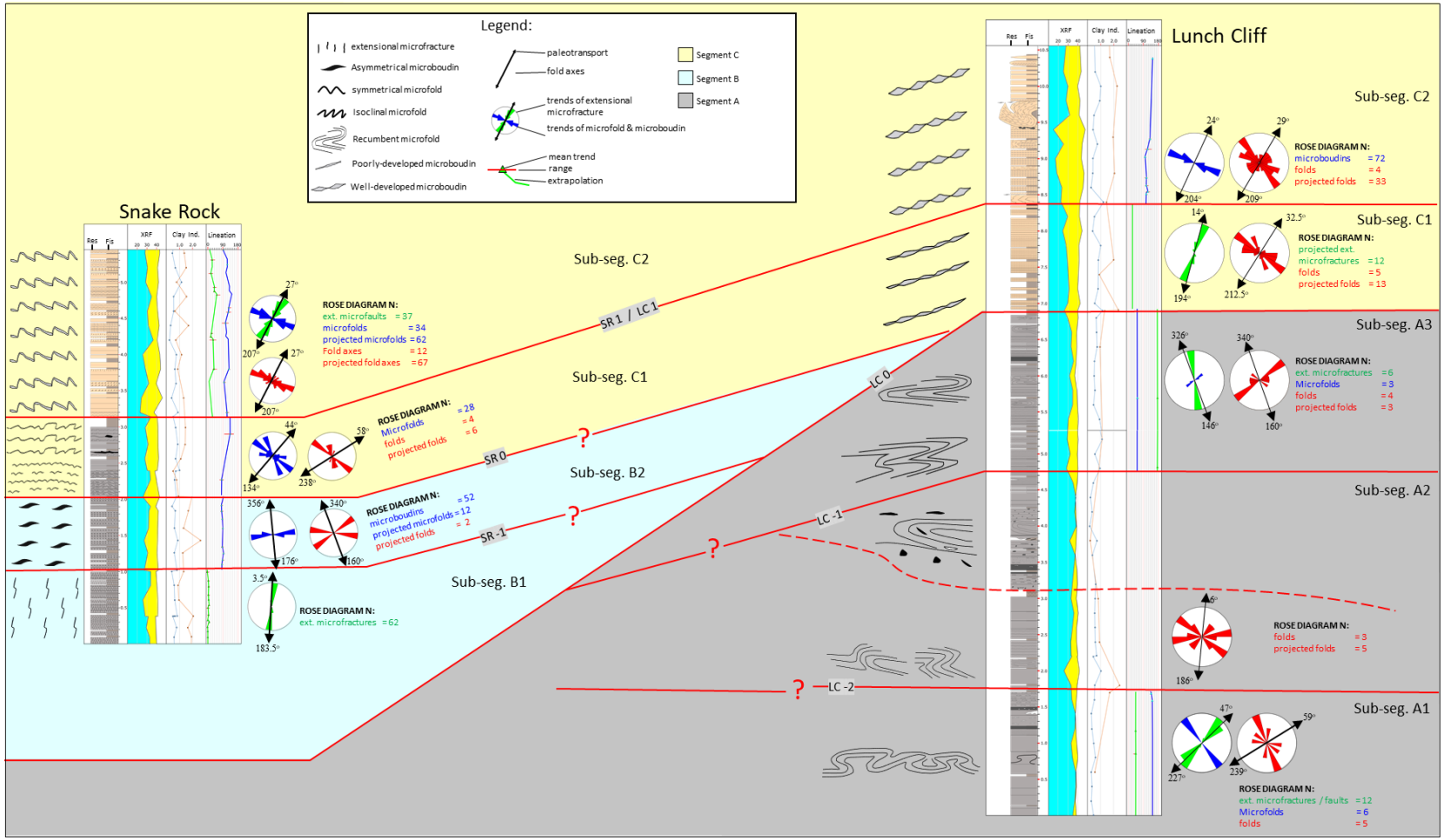

Figure 1.12 MTD architecture (borehole style): The MTDs in the area of interest is divided into segments based on their lithofacies, i.e., segment A, B, and C. The smaller segments formed around the contact between segments are referred as sub-segment A1, A2, B1, B2, etc., according to the hosting segments and the spatial elevations. The characteristic contrasts between segments and sub-segments are also summarized in this figure, and are discussed in detail in the following sub-sections.

1.5.3 Segment A

Lithofacies

The resilient beds of segment A are comprised of light-grey beds and occasional intercalations of black beds, associated with undeformed to slightly deformed dark-grey microbeds and thin white laminae (Fig. 1.14 – P1 through P6). Thin section analysis shows that the dark-grey microbeds are composed of sharp-based packstone that fine upward into clayey to clay-rich packstone, which have light-grey weathering color (Fig. 1.14 – P5). The lithofacies are locally associated with gravel-sized, semi-rounded intraclasts and rip-up clasts (Fig. 1.14 – P2 and P4). According to XRF data, the black-colored clasts are Calcium rich (~37.5 wt.%), but low in Silicon (<1 wt.%); while the light-colored clasts contain moderate Calcium (11 – 17 wt%), and high Silicon (28 – 36 wt.%). Based on the textural characteristics, the pre-failure depositional processes of these beds are likely a combination of turbidity currents and debris flows.

The lithofacies of segment A is defined by its ultra-low silicon content in both resilient (5.2 wt.%) and fissile beds (9.21 wt.%), which measure about half to one-third those in segment B and C (Fig. 1.13, see the log in Fig. 1.12). The resilient beds make up about 92% of the overall measured section (86% and 82 – 85% in segment B and C, respectively). The thickness proportion of relatively 'clean' packstone in the resilient beds is very low, ranging from 3% to 14%, with an average of 8% (n = 6) (27% and 36 – 40% in segment B and C, respectively) (compare Fig. 1.14 - P5, Fig. 1.15 – P.2, and Fig. 1.16 – P2), except for some localities with intercalations of dark beds, which can be as high as 27% or more.

Microstructure & Deformation Orientation

Most of microbeds in segment A are relatively undisturbed compared to the other segments. Some sparse microstructures documented include recumbent microfolds (Fig. 1.14 - P1, P6), symmetrical – open microfolds, microboudins (Fig.14 - P3), and microfractures (Fig. 1.14 – P5). There is no obvious microstructure variation between sub-segment A1, A2, and A3. However, fold axis and lineation measurements are very effective in distinguishing segments. The paleotransport direction in sub-segment A1, A2, and A3 notably vary from NE – SW, N-S, to NNW – SSE, respectively (> 40° difference).

1.5.4 Segment B

Lithofacies

The resilient beds of segment B are dominantly light-grey in color, associated with millimeter-scale, dark-grey microbeds (Fig. 1.15 – P1 through P5). The microbeds can be laterally continuous or discontinuous / detached, and exhibit offsets, depending on the corresponding microstructure types. Under thin sections, the lithology consists of stacked fining-upward packages with sharp bases that grade from grainstone – packstone (dark-grey weathering color) to clayey – clay-rich packstone (light-grey weathering color), which likely represent rhythmic turbidites deposited prior to the emplacement of the Cutoff MTDs (Fig. 1.15 – P2). In addition, some beds in Segment B1 contain 'granulose' packstone surrounded by clayey packstone 'matrix' (described in detail in Simabrata et al., Part B). Silicification, dolomitization, and pyritization occurs locally.

The XRF signatures of segment B is very similar to those of segment C, except that the clay indicator in fissile beds of the former is ~ 30% higher than the later (Fig. 1.13). The second defining characteristic is that the thickness proportion of relatively 'clean' packstone in segment

B ranges between 14% to 33%, with an average of 27% (n = 11), which are half that of segment C (mean: 36 – 40%). The resilient beds make up about 86% of the overall measured section, and therefore virtually identical to segment C in this department (82 – 85 %). Based on these evidences, we interpret the lithofacies in segment B as the sub-type of lithofacies in segment C.

Microstructure & Deformation Orientation

Segment B hosts a noteworthy variation of microstructure styles that enables distinction between sub-segment B1 from B2. Sub-segment B1 is comprised of almost exclusively extensional microfractures (with minor microboudins) that manifest as dark-grey 'tiger stripes' in the outcrop (Fig. 1.15 – P1 through P3). Under thin sections, the microfractures do not exhibit clear margins, are not grain-penetrative, and are filled with packstone – inside which some spicule bioclasts are oriented upward (Fig. 1.15 – P2) (see Simabrata et al., Part B). Some of the microfractures create offsets on microbeds, which qualify as normal microfaults. The extensional microfractures terminate abruptly below surface SR -1. In contrast, sub-segment B2 is dominated almost exclusively by asymmetrical microboudins that incline upslope, and are commonly associated with normal microfaults and detached isoclinal microfolds that verge downslope (also see Simabrata et al., Part B). Lineation and fold axis measurements between the two sub-segments do not exhibit noteworthy variation, i.e., $<10^{o}$ difference.

1.5.5 Segment C

Lithofacies

The resilient beds of segment C comprise alternating light-grey, dark-grey, and brown microbeds (Fig. 1.16 – P3 and P6). Under thin sections, the light-grey, dark-grey, and brown microbeds are identified as clayey to clay-rich packstone, packstone, and silicified packstone, respectively (Fig. 1.16 – P2). Sharp bases and fining upward features on packstone microbeds

are sometimes visible, but are sometimes absent. Silicification preferentially occurs within packstone and abruptly terminate close to the base of clayey – clay-rich packstone (Fig. 1.16 – P2) (see section 5.3). Pyritization and dolomitization are also present, though not as widespread as silicification. Based on the textural characteristics, lithofacies C likely originated from pre-failure turbidity currents. Note that silicification in lithofacies C may have been caused by pre-failure or post-failure diagenesis.

Lithofacies C in Lunch Cliff and Snake Rock share similar proportion of resilient beds (82% vs. 85%) in the measured sections, an almost identical proportion of packstone microbeds (40% vs. 36%) and clay indicators (resilient: 0.61 wt.% vs. 0.64 wt.%; fissile: 1.12 wt.% vs. 1.25 wt.%) (Fig. 1.13), which subtle differences can be attributed to lateral variability of lithology over 150 meters of distance. Note that silicification is widespread enough (gives off brown hue to the outcrops) to be easily seen on thin sections, but not necessarily enough to manifest in the XRF. For instance, although the highly silicified areas of thin section P2 (see Fig. 1.16) contain about 10 - 15% more silicon than the lightly silicified counterparts, the former areas occur only sporadically and therefore does not significantly alter the bulk XRF measurement. However, the Lunch Cliff counterpart of lithofacies C does exhibit an upward increase in silica (from 8.6 – 9.4 meter, see Fig. 1.16), which is likely caused by more intense silicification.

Microstructure & Deformation Orientation

Sub-segment C1 in Snake Rock hosts chaotic microfolds in the lower part (Fig. 1.16 – P1) and downslope-verging microfolds in the upper part. Sub-segment C2 has a wider variety of microstructures, which include predominantly microfolds that are greater in amplitude and wavelength compared to sub-segment C1 (Fig. 1.16 – P2, P3) (also see Simabrata et al., part B), which crests are inclining upslope – opposite to microfold inclination in sub-segment C1. Other

accessory microstructures include transform and normal microfaults, thrust microfaults, and microboudins. However, the microstructure styles of sub-segment C1 and C2 in Snake Rock do not correlate well with their Lunch Cliff counterparts. In Lunch Cliff, sub-segment C1 is dominated by poorly-developed microboudins and commonly associated with normal microfaults and localized microfractures, all of which make the hosting microbeds appear wavy to discontinuous, with pinching and swelling (Fig. 1.16 - P4). These poorly-developed microboudins seem to affect only thin microbeds (1 - 2 mm), while the thicker counterparts (10 - 20 mm) remain intact. In sub-segment C2, the microbeds are also invested by microboudins, but much well-developed compared to the previous sub-segment, which now affect both thin and thick microbeds (Fig. 1.16 – P5, P6). Microstructure lineations and fold-axis orientations between sub-segment C1 and C2 show distinctive vertical variations in Snake Rock (17° - 31° difference), but are relatively subtle in Lunch Cliff ($<10^o$ difference). The lateral continuity of deformation orientations from Snake Rock to Lunch Cliff rotates anti-clockwise in sub-segment C1, but is relatively well-maintained in sub-segment C2.

1.5.6 Recognition Criteria for MTD Segments

Lithofacies Contrasts

As exemplified in this research, segments can be predicted from the change of lithofacies characteristics, which encompasses but is not limited to: (1) the variation of XRF signatures such as Ca/Si ratios and clay mineral indicators, (2) changes in stacking patterns, i.e., the ratio of resilient and fissile beds, the thickness proportion of ‘clean’ packstone versus clay-rich packstone, and (3) differences in grain size and depositional textures (e.g., presence of intraclasts). These observations are consistent with recent outcrop and seismic studies that show how MTD compartments coincide with changes in lithofacies and seismic facies. In the

subsurface, these variabilities can be readily resolved using well logs, image logs (FMI) (e.g., Asmus and Grammer, 2013), and core data. Furthermore, segments identified from one well can be correlated to other wells using lithofacies, as the major termination surfaces separating segments can be traced up to a few kilometers in the Cutoff Formation (Amerman et al., 2011; Hurd et al., 2016). However, abrupt changes in thickness and/or termination may occur (e.g., Fig. 1.12), and caution is advised using well log data alone.

Microstructure Contrasts

The vertical contrast of microstructure styles can be used as proxies to identify sub-segments that are not resolved under lithofacies contrasts, albeit with mixed results. As shown in this research, some sub-segments can be easily identified from the change of microstructure styles, e.g., extensional microfractures in sub-segment B1 vs. asymmetrical microboudins in sub-segment B2; while other sub-segments show subtle to no microstructure contrasts, e.g., sub-segment C1 and C2 in Lunch Cliff differ only in the development of microboudins, and sub-segment A1 through A4 are devoid of microstructure contrasts. Furthermore, the contrast of microstructure styles is not a good proxy for intersegment correlation. Examples from sub-segment C1 and C2 in Snake Rock and Lunch Cliff show that microstructure styles can change significantly within a distance of 150 meters. In the subsurface, although the contrast of microstructures is rather difficult to resolve due to scale issues, cores and log image may still be useful. Sub-segments (thickness: 1 – 2 meters) identified from such methods should be expected to terminate over a relatively short distance (perhaps a few tens or hundred meters).

Deformation Orientation Contrasts

Identification of vertical sub-segments using the contrast of deformation orientation (i.e., paleotransport direction) also shows mixed results. In segment A, this method is capable of

resolving all three sub-segments with high degree of clarity, with over 40° of difference in the inferred paleotransport direction. On the other hands, the same method is not effective in segment B (<10° difference), and only somewhat effective in segment C (<10° – 31° difference). Furthermore, intersegment correlation using the similarity of paleotransport direction is inconsistent; for example, sub-segment C2 has consistent paleotransport direction at SR and LC, but sub-segment C1 varies by almost 30° between SR and LC. In the subsurface, the measurements of paleotransport indicators can be measured using FMI log or oriented cores (Fig. 1.12; also see Henry et al., 2018). Rose diagrams (e.g., Fig. 1.12) are particularly useful for microstructure lineations, where multimodality can help identify sub-segments (e.g., Fig. 1.17) due to the high H-index of microstructure lineations (0.73 – 0.97, this research).

Summary

Based on the outcrop analog in this research, MTD segments and sub-segments are best determined when all three approaches, i.e., the contrast of lithofacies, deformation styles, and deformation orientations, are applied in conjunction. The first step is to delineate and correlate segments using electrical borehole data, or other techniques that can distinguish lithofacies contrasts in MTDs such as FMI logs. Sub-segments can be further identified by examining the change of deformation styles (i.e., microstructure types) and deformation orientations. While some segments and sub-segments may be successfully resolved in one method and left unrecognized in the other, a combination of multiple approaches can enhance the likelihood of predicting compartmentalization in MTDs.

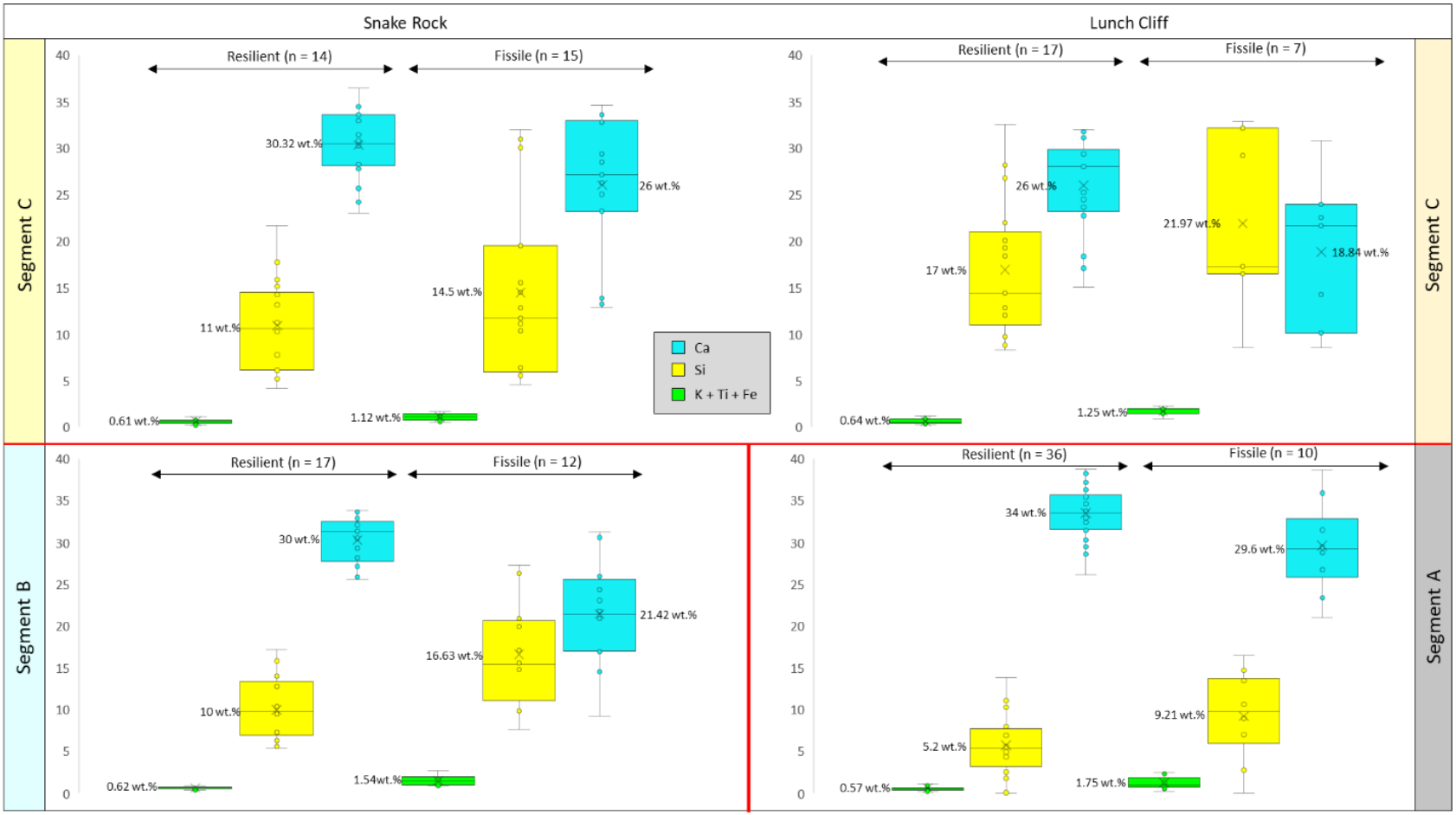

Figure 1.13 XRF data of resilient and fissile beds grouped according to the segments and outcrop locations.

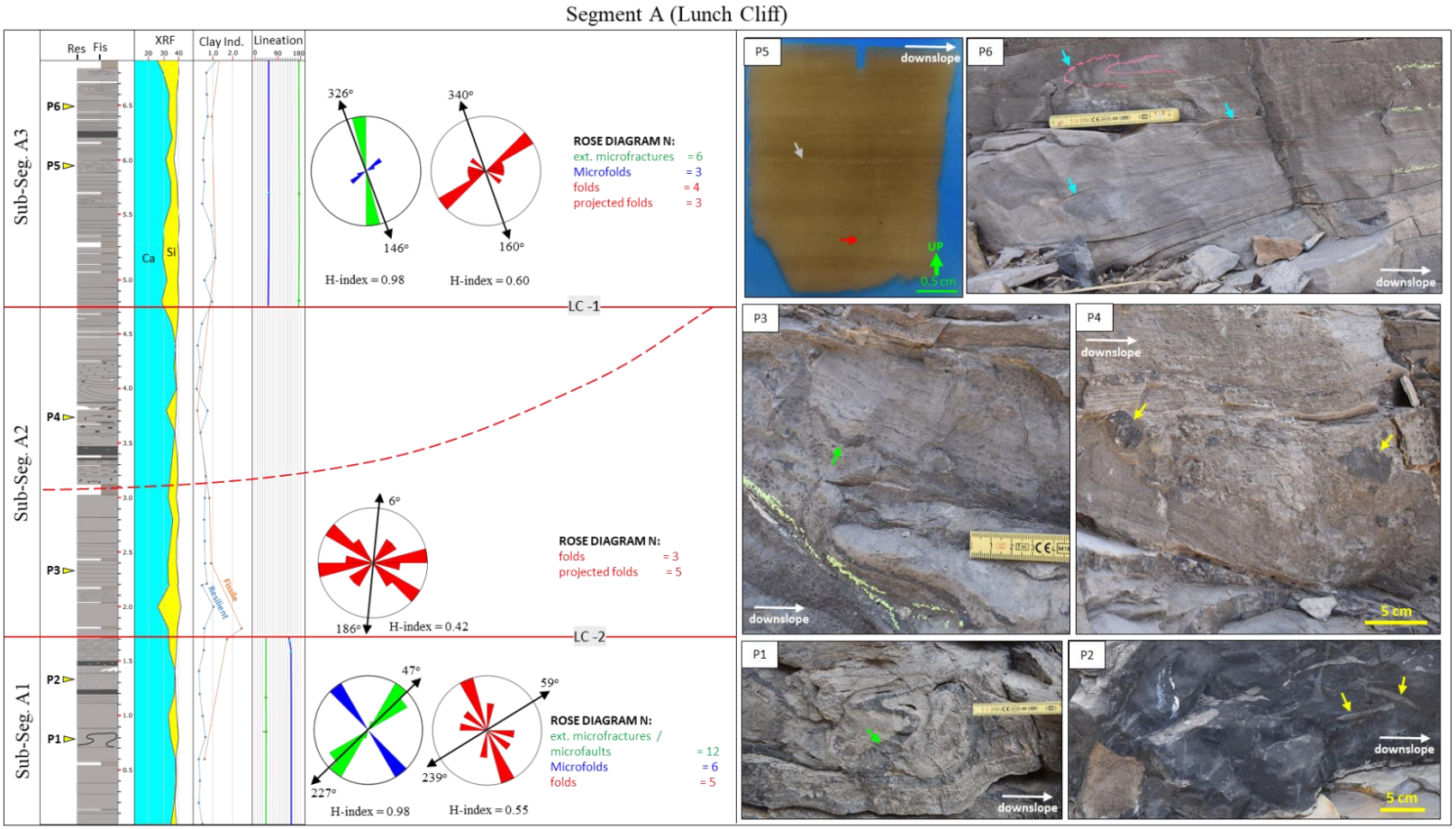

Figure 1.14 The log tracks are given as follows (from left to right): (1) sub-segment name, (2) lithology, deformation style, and the stratigraphic position of photos (right), (3) the proportion of Calcium and Silicon in resilient beds (wt.%), (4) clay indicators (wt.%) for resilient (blue line) and fissile beds (brown line), and (5) bidirectional lineation orientation -- left to right panel is 0 - 180 degrees of compass direction. The rose diagrams summarize the strike of extensional microstructures (green), microfolds and microboudins (blue), and fold axes (red). Photo: yellow arrows are gravel-sized clasts and ripped-up clasts. Green arrows are black beds and microbeds (high calcium, usually packstone). Blue arrows are recumbent microfolds. The grew arrow is sharp-based, fining upward packstone - grainstone. The red arrow is microfracture.

Segment B (Snake Rock)

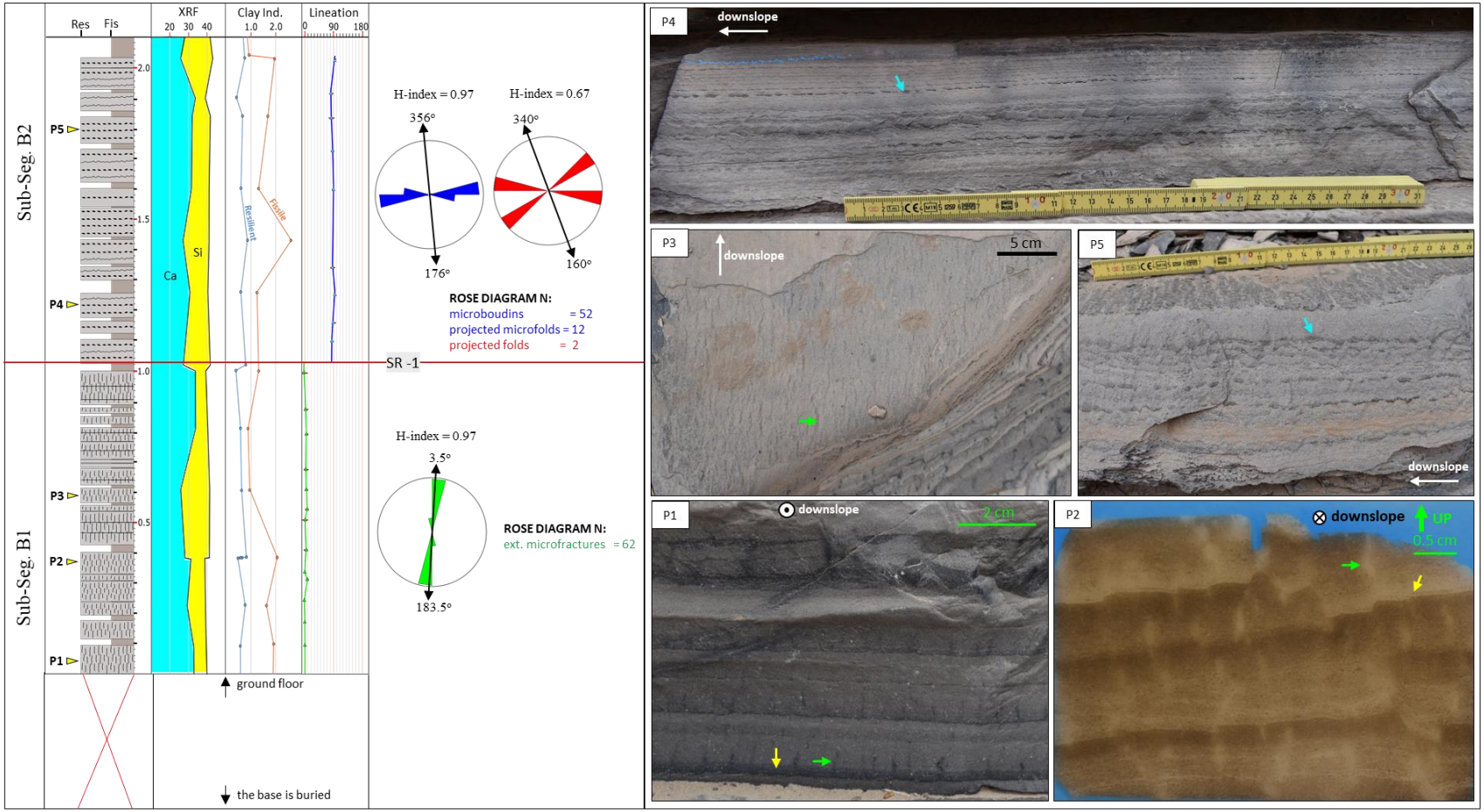

Figure 1.15 The log tracks are given as follows (from left to right): (1) sub-segment name, (2) lithology, deformation style, and the stratigraphic position of photos (right), (3) the proportion of Calcium and Silicon in resilient beds (wt.%), (4) clay indicators (wt.%) for resilient (blue line) and fissile beds (brown line), and (5) bidirectional lineation orientation -- left to right panel is 0 - 180 degrees of compass direction. The rose diagrams summarize the strike of extensional microstructures (green), microfolds and microboudins (blue), and fold axes (red). Photos: yellow arrows are sharp-based, fining upward packstone - grainstone. Green arrows are extensional microfractures. Blue arrows are asymmetrical microboudins.

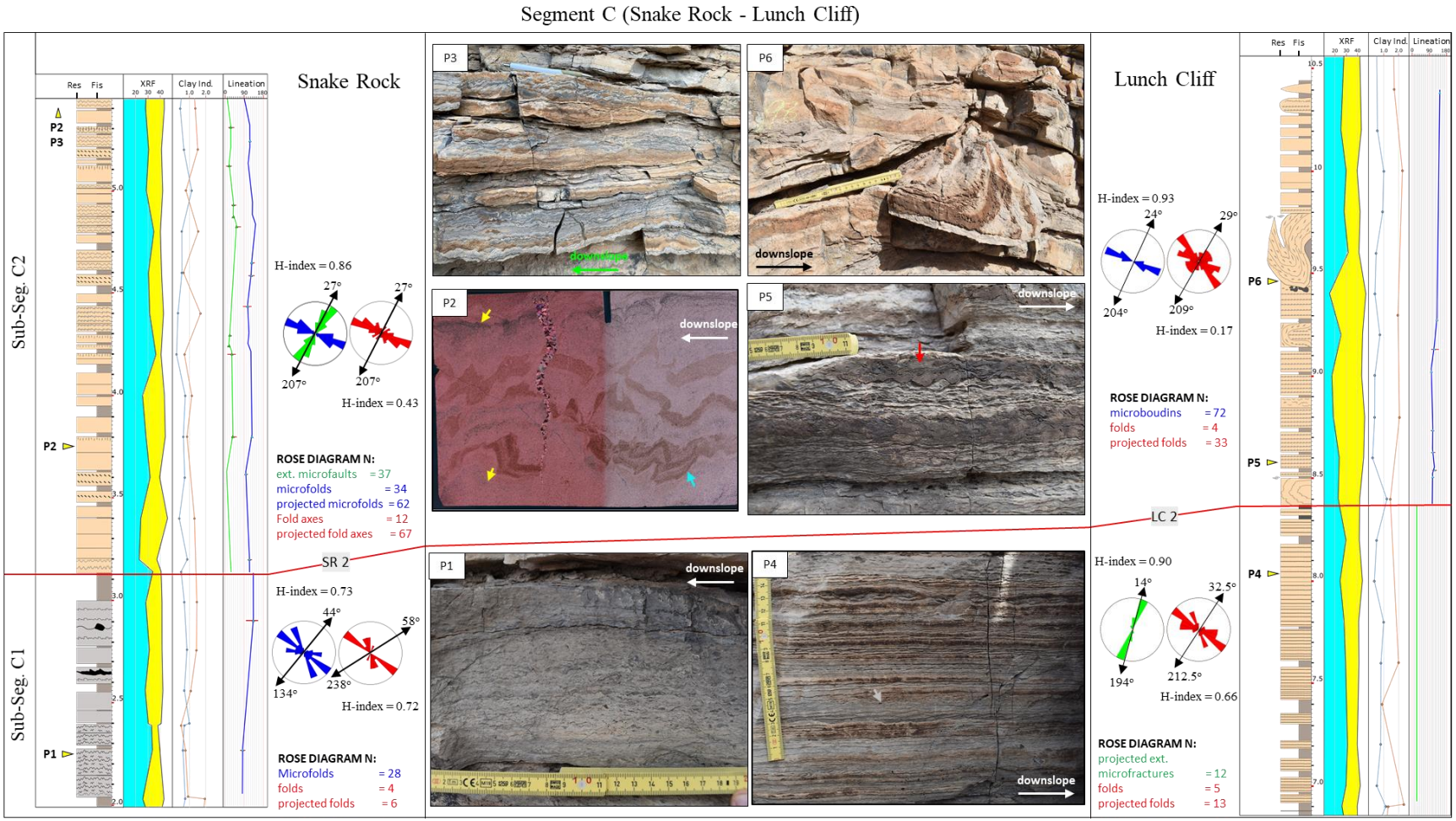

Figure 1.16 The log tracks are given as follows (from left to right): (1) sub-segment name, (2) lithology, deformation style, and the stratigraphic position of photos (right), (3) the proportion of Calcium and Silicon in resilient beds (wt.%), (4) clay indicators (wt.%) for resilient (blue line) and fissile beds (brown line), and (5) bidirectional lineation orientation -- left to right panel is 0 - 180 degrees of compass direction. The rose diagrams summarize the strike of extensional microstructures (green), microfolds and microboudins (blue), and fold axes (red). Photos: The grew arrow is normal microfault associated with poorly-developed microboudins. The red arrow is well-developed microboudins. Yellow arrows are silicified packstone.

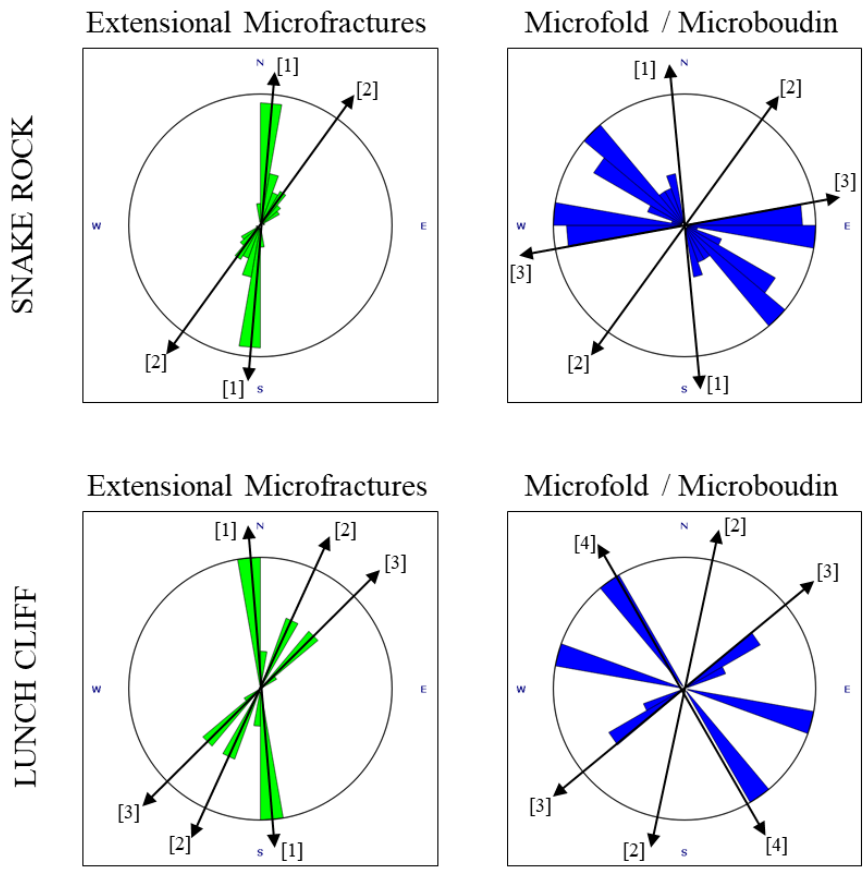

Figure 1.17 Bulk Plotting can be a powerful tool to predict the number of segments in MTDs. In this example, bulk plotting of extensional microfractures, microfolds, and microboudins reveal three and four segments in Snake Rock and Lunch Cliff, respectively. Note that the data-count (n) used in this procedure has been normalized to avoid over-representation of data from a particular segment.

1.6 Discussion

1.6.1 Kinematic Evolution of The Cutoff MTDs

The six possible origins of MTD compartmentalization briefly discussed in the introduction can be further simplified into three categories: (1) compartmentalization by the amalgamation of multiple mass-failures (includes hypothesis 1 - 4, see Introduction), (2) partial flow transformation, and (3) compartmentalization by internal deformation (i.e., a single MTD with internal shear surfaces). Here we further explore the possibilities of the first and third

simplified hypotheses to be applied in the Cutoff MTDs, and we also discuss how these hypotheses fit into the dataset acquired in this research and other studies elsewhere.

The existence of ‘drape’ intervals (non-MTD, organic-rich, carbonate mudstones) sandwiched between several MTD segments in the Cutoff Formation has been invoked as evidence for the multiple mass-failure hypothesis (Amerman et al., 2011). The localized nature of these drape intervals can be attributed to the infilling of preexisting paleotopography created by former MTDs, or to partial removal by subsequent erosive MTDs (Amerman et al., 2011). Furthermore, the coeval mass-failure hypothesis can satisfactorily explain the data collected in this research. Lithofacies characteristics tend to change between segments because the coeval mass-failure events were sourced from different localities. For instance, pulses of retrogressive failures would procedure segment amalgamation that exhibit ‘shallowing-upward’ trend, as the new sediment sources progressively retrograde toward the platform. Microstructure types can be distinctive across segments because independent MTD events experience different strain, and the lateral continuity is not well-maintained within the same segment due to strain partitioning across different morphodomains (e.g., Cardona et al., 2020). Deformation orientations also tend to change across segments due to the variations in paleotransport directions from event to event, yet the deformation orientations (paleotransport directions) are rather consistent within the same segment because it was deformed as a single body. Intense shear around the contact of segments formed a damage zone that resulted in sub-segments. These sub-segments behaved like individual MTDs, which stress regime and deformation were isolated from one another.

While the kinematic of coeval mass-failure can be inferred directly from the intercalation of non-MTD units between segments, the internal deformation hypothesis (i.e., single MTD with interval shear surfaces/zones) is much more difficult to prove. Nonetheless, the existence of

internal shear surface/zones has been strongly supported by a seismic study on a mega block (350 m of maximum height, 13 km^2 of area) in the Espirito Santo Basin, SE Brazil (Fig. 1.18C) (see Gamboa and Alves, 2015). The mega block is compartmentalized into two segments (upper and lower) by a within-block shear surface, which is unlikely the product of multiple amalgamated MTDs (Fig. 1.18A). The upper segment of the mega block hosts large-scale fault-propagation folds (FPF), detached from the termination surface, much similar to those observed in our research. In addition, the termination surface is also offset by series of normal faults (Fig. 1.18B). These observations indicate that the within-block termination surface predates both the FPFs and the normal faults, i.e., formed early during the mass-failure event – similar to the model proposed by Le Goff et al. (2020). Furthermore, the within-block termination surface also bounds two contrasting seismic facies, suggesting that its formation may be promoted by the contrast of lithofacies characteristics. In our area of interest, the compartmentalization of the Cutoff MTDs can also be explained in the similar manner: (1) Initially, a failure occurred on sediment mass that contained multiple high-order lithofacies packages, (2) during the early stage of emplacement, these contrasts in lithofacies triggered the formation of shear zones that compartmentalized the failed mass into segments and sub-segments, (3) Mechanical slip facilitated by termination surfaces allowed these segments and sub-segments to decouple, and (4) the decoupling of segments and sub-segments promoted differential strain and deformation (akin to the contemporary flow-cell model; see Alsop and Marco, 2014; Nugraha et al., 2020), which gave rise to the contrasts of microstructure types and deformation orientations (Fig. 1.18D). The only observation the internal deformation hypothesis cannot explain is the presence of non-MTD intervals draped between segments. Notwithstanding, the two simplified hypotheses discussed here are not mutually exclusive, and the Cutoff MTDs may have undergone both mechanisms.

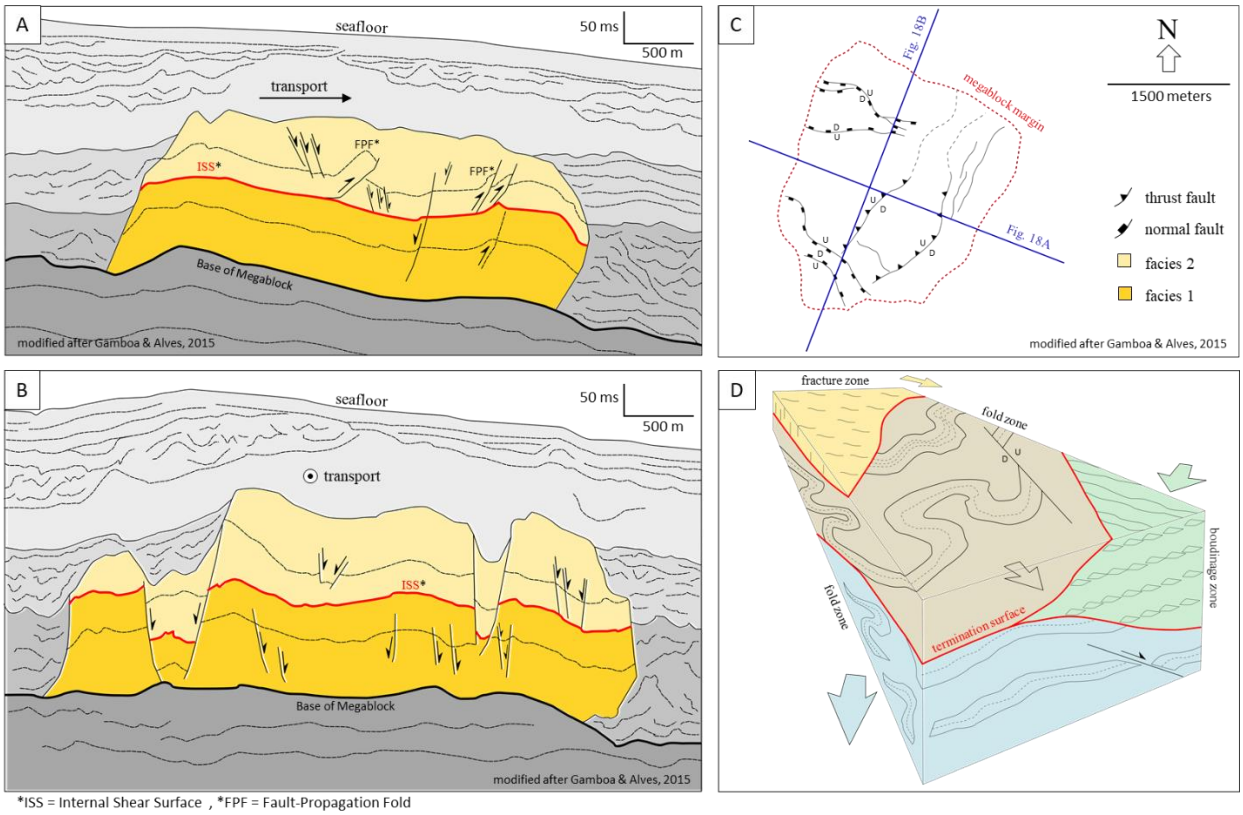

Figure 1.18 (A) Transport-parallel section: The within-block Internal shear surface (ISS) separates the megablock of two distinctive seismic facies. Fault-propagation folds (FPF) are detached from the ISS. (B) transport-perpendicular section: The within-block ISS is offset by series of normal faults. Based on the deformation architecture, the within-block ISS likely predates both the FPF and normal faults. (C) Map of mega-block. (D) Segments bounded by termination surfaces behave like individual MTDs with distinct stress regime, deformation characteristics, and relative transport directions - similar to the contemporary flow-cell model. Large arrows indicate transport directions. The schematic diagram is also applicable to high-order segments.

1.6.2 Grain-fabric Alignments and Anisotropy

The long axes of elongated grains in MTDs are aligned perpendicular to the transport direction, which has been demonstrated in outcrop and subsurface studies using magnetic-fabric anisotropy (e.g., Kanamatsu et al., 2014; Weinberger et al., 2017). However, previous studies do not consider the variability of grain-fabric alignments between segments and/or sub-segments. This study presents an such opportunity due to the abundance of sponge spicule bioclasts in the

area of interest. Four bedding-plane-parallel thin sections collected in Snake Rock indicate that the orderliness (H-index) and dominant trend of spicules vary quite notably from one sub-segment to another (Fig. 1.19). We predict that differential shear experienced by each sub-segment controls the intersegment heterogeneity of H-index (also see Simabrata et al., Part B), with the shear vertex rests on the segment boundaries. Note that H-index increases with average spicule long-axis lengths, and has relatively higher values in clay matrix compared to carbonate mud (Simabrata et al., Part B). The disparities of H-index between sub-segments remain true when the grain lengths and matrix types are hold constant (Simabrata et al., Part B). Therefore, this observation can potentially serve as another parameter to recognize the compartmentalization of MTDs in the subsurface.

The alignment of grain-fabric in MTDs can promote anisotropy of mechanical (e.g., strength, elastic moduli) and petrophysical properties (e.g., directional permeability), which are of critical concern in the assessment of reservoir and seal quality. Anisotropy direction is governed by the dominant trend of fabric alignment (see Saroglou et al., 2003; Barton and Quadros, 2015), and the strength of anisotropy is likely dependent on the orderliness (H-index) and the relative abundance of elongated grains within rock fabric (Simabrata et al., Part B). In the area of interest, the abundance of sponge spicules is relatively constant (~12%), but the dominant trends and the H-index vary between sub-segments (Fig. 1.19), which illustrates how the anisotropy of mechanical and petrophysical properties in compartmentalized MTDs can be extremely complex in sub-seismic scale. This issue becomes even more intricate when the variations of microstructure types and trends are taken into consideration, e.g., microfracture vs. microfold zones.

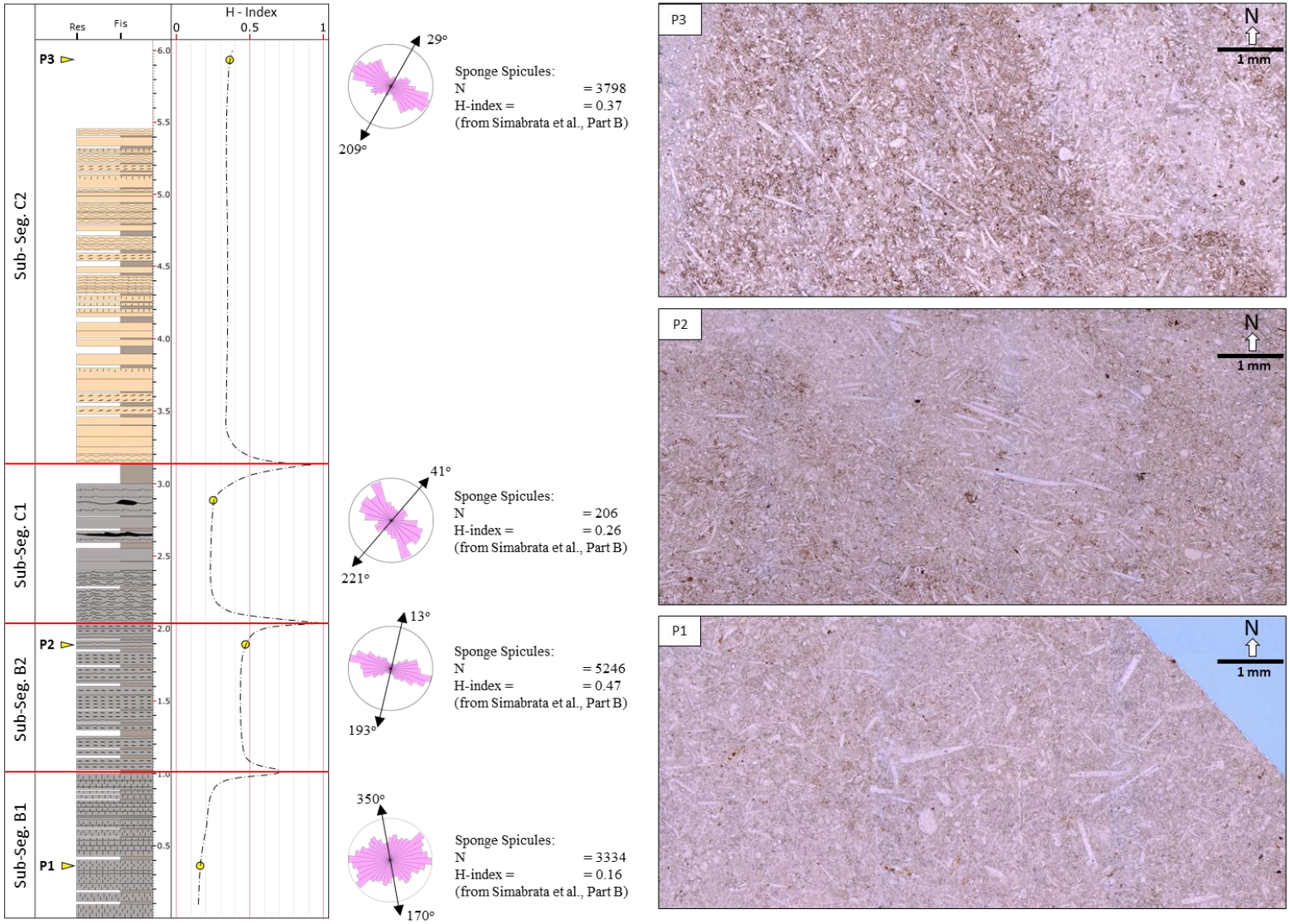

Figure 1.19 Grain-fabric alignments between segments: dot-dash line is the predicted trend of H-index. Note the spikes of H-index on termination surfaces.

1.6.3 Silicification and Flow Barrier

Although silicification occurs throughout the area of interest, our data indicates that this diagenetic process is particularly more widespread in lithofacies C, which gives the unit brownish hue (Fig. 1.7A and Fig. 1.8A). Thin section evidence shows that the silicification in lithofacies C preferentially occurs on packstone microbeds and appears 'sealed' by the clayey to clay-rich counterpart (Fig. 1.20A). In other locations within the same thin section, the silicification are highly concentrated along specific pathways within packstone lithology (Fig. 1.20B), commonly near the upper boundary of packstone (Fig. 1.20C). Based on these observations, we suspect that the diagenetic process was driven by silica-rich fluid (e.g., You et al., 2018). Higher permeability in packstone allowed for circulation of saturated fluid and the ensuing precipitation (also see Pisani et al., 2022). The concentration of silicification along specific pathways indicate highly permeable zone within the packstone lithology. Enhanced silicification in the upper part of packstone beds is probably caused by upward fluid migration that was deflected along the bedding-plane of impermeable clayey – clay-rich packstone. Consistent with the thin-section interpretation, the brown hue of segment C terminates abruptly to semi-abruptly on termination surface LC 0 and SR 0 probably because these bounding surfaces have sealing properties, or the underlying lithofacies types (A and B) are inherently more impermeable (also see Souza et al., 2021). In the context of reservoir characterization, the presence of multiple MTD segments and their associated termination surfaces (regardless of their genetic origin) can therefore serve as lateral hydraulic barriers, and/or potentially as lateral conduits (thief zones) if the permeability of segments or termination surfaces are anomalously high.

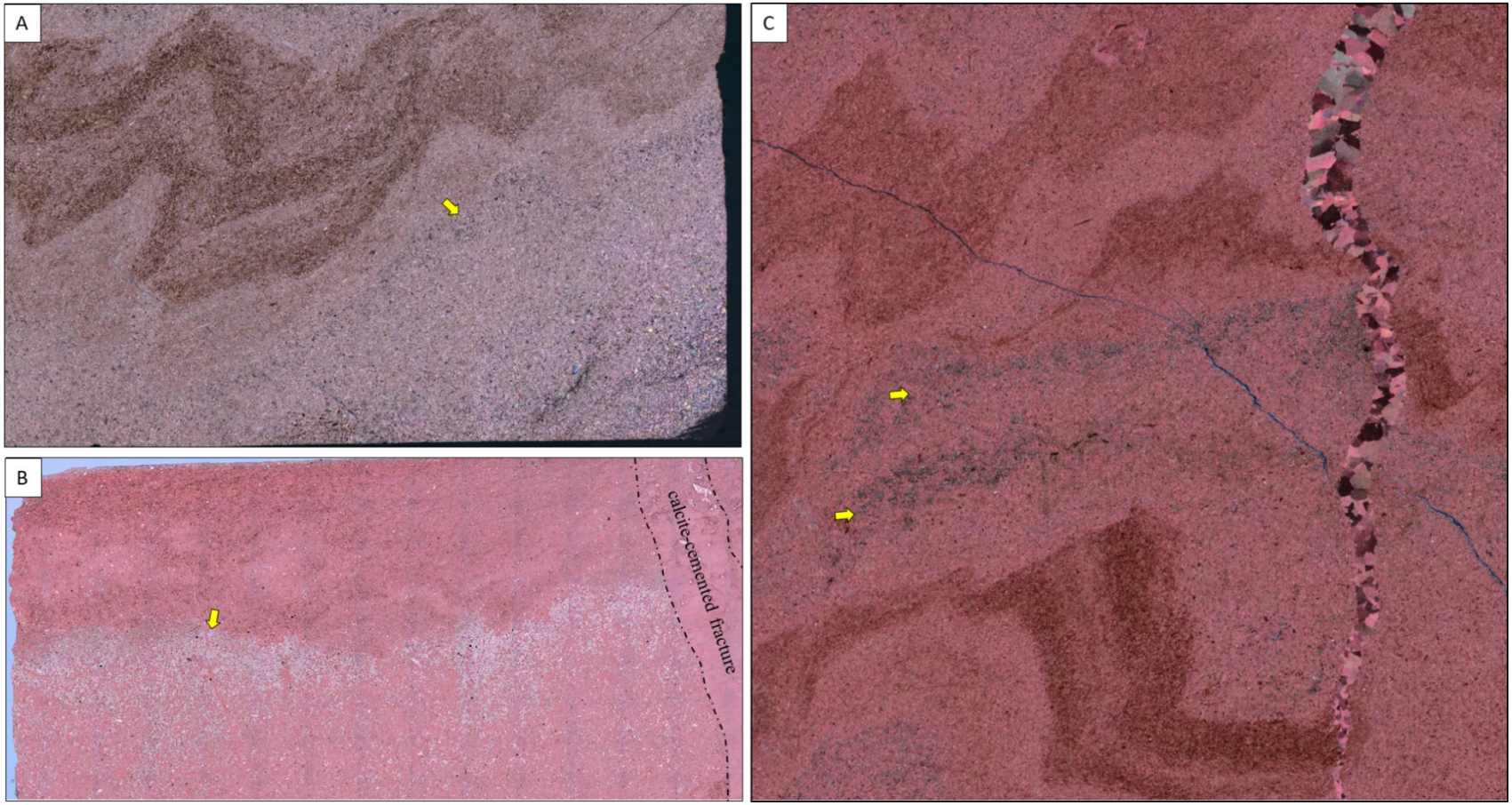

Figure 1.20 (A) Thin section without red alizarin (cross-polarized light): The black zones are silicified packstone, which terminate abruptly at the base of clayey packstone (yellow arrow). (B) Thin section with red alizarin (plane light): white areas are silicified packstone, which terminate abruptly at the base of clayey - clay-rich packstone (yellow arrow). (C) Thin section with red alizarin (cross-polarized light): yellow arrows indicate silicification along two highly permeable paths within packstone.

1.7 Conclusions

Mass-transport deposits in the area of interest (the Cutoff Formation) are compartmentalized into three segments (termed segment A, B, and C), bounded by major termination surfaces. Sub-segments are observed along the contact of segments, which we interpret as a shear zone (a damage zone). Our research shows that:

1. Segments can be identified from the contrast of lithofacies characteristics, which include XRF signatures (e.g., calcium vs. silica, clay indicator), stacking patterns, and possibly depositional texture. The similarity of lithofacies can be utilized as a proxy to conduct intersegment correlation. However, lithofacies contrasts are not effective in recognizing sub-segments formed within the shear zone.
2. Sub-segments can be discerned, with mixed results, from vertical variation of microstructure types, e.g., extensional fractures vs. microfolds. However, this technique is likely not useful for intersegment correlation.
3. Deformation orientations (as the indicator of paleotransport directions) can also identify vertical sub-segments, albeit with mixed results, but is sometimes reliable for intersegment correlations.
4. The abovementioned approaches can be utilized to borehole data such as electrical logs, image logs (FMI), and oriented samples (e.g., cores). We show that applying all the methods in conjunction increases the likelihood of identifying MTD segments in the subsurface.

Identification of segments can have broad implication on the subsurface formation evaluation, including reservoir characterization and seal-potential assessments. Grain-fabric alignment and microstructures in MTDs promote the anisotropy (and heterogeneity) of

mechanical and petrophysical properties. Termination surfaces (shear surfaces / zones) can either act as baffles or barrier to fluid flow.

CHAPTER 2

GRAIN-FABRIC ALIGNMENTS IN MIXED CARBONATE-SILICICLASTIC MASS-TRANSPORT DEPOSITS: THE CUTOFF FORMATION, PERMIAN BASIN, TEXAS

2.1 Abstract

Mass-transport deposits (MTDs) undergo fabric modification during emplacement that results in alignments of elongated grains. Grain-fabric alignments promote mechanical and petrophysical anisotropy, which has broad implications in hydrocarbon extraction, carbon sequestration, and geohazard assessment. These implications are likely more pronounced in carbonate MTDs where the proportion of elongated grains can be much higher with greater aspect ratio compared to siliciclastic counterparts. However, the characteristics of grain-fabric alignments are currently underexplored. In this research, we inspect the predictive properties of grain-fabric alignments that include three-dimensional orientation, fine-scale heterogeneity, as well as the control of grain lengths and clay mineral.

This study focuses on the outcropping Cutoff Formation – a mixed carbonate-siliciclastic mass-transport deposits (MTDs) emplaced on the relic Leonardian Slope, Permian Basin. The Cutoff MTDs contain prolific spicule bioclasts (prolate-shaped), which enabled qualitative and quantitative grain-fabric analysis. Investigation of over 29,000 spicule grains from oriented thin sections leads to the following conclusions: (1) the long-axes of elongated grains are parallel to bedding trends, which can be horizontal or tilted/folded, (2) the long-axes are, in general, transverse to paleotransport direction, (3) the fine-scale trends and wellness of alignment (H-index) of elongated grains are heterogeneous across samples, as well as within the same sample,

(4) H-index increases with greater grain lengths (i.e., aspect ratios are likely constant), and the presence of clay mineral, and (5) H-index is likely controlled by differential strain between MTD zones (segments) and/or variation in microstructure types. These results improve our understanding of grain-fabric alignments in MTDs, which can help predict anisotropy. The method employed in this research can be applied to other similar fabric alignment phenomena globally.

2.2 Introduction

Mass-transport deposits/MTDs are important elements in deep-water sedimentary succession in both marine and lacustrine depositional systems (Posamentier and Walker, 2006; Sammartini et al., 2019) and play an important role in energy resource and geohazard assessments (Clare et al., 2016). MTDs are found in a wide spectrum of sedimentary basins, including those containing siliciclastic, mixed carbonate-siliciclastic, and carbonate sediments, and also in volcanic settings (Moscardelli and Wood, 2016). Mass-transport deposit facies reflect a broad spectrum of processes related to their complex flow rheology, including slides, slumps, and debris flows, as well as associated turbidites (Posamentier and Martinsen, 2011). Components of these deposits range from mud-sized material to km-scale rafted blocks. The roles of MTDs as reservoirs or seals in petroleum systems are controlled by the pre-failure source composition (Posamentier and Martinsen, 2011), emplacement-induced faults and fractures (Ferrill et al., 2014; Gamboa and Alves, 2015), and fabric modification during transport (e.g., Day-Stirrat et al., 2013). Fabric modification can include the incorporation of the underlying substrates by MTD basal-shear processes (Cardona, L.J. Wood, et al., 2020), shear-induced consolidation and densification (Shipp et al., 2004; Sawyer et al., 2009; Dugan, 2012), rearrangement of clay fabric and pore structures (Day-Stirrat et al., 2013), and alignments of

magnetic fabric, which generally correspond to the orientation of magnetic grains (e.g., Schwehr et al., 2007; Meissl et al., 2011; Kanamatsu et al., 2014; Weinberger et al., 2017; Alsop et al., 2020).

Alignments in rock fabric (e.g., fossil orientations, metamorphic foliation) generate anisotropy on petrophysical properties (e.g., permeability) and mechanical properties (e.g., wave propagation, elastic modulus, strength), with the maximum and minimum values usually coinciding with either the direction parallel or transverse to the alignments (e.g., Saroglou et al., 2003; Özbek, 2009; Barton and Quadros, 2015; Backeberg et al., 2017; Nabawy, 2018; DeReuil et al., 2019; Sato et al., 2019). Petrophysical anisotropy in the subsurface can impact production performance, behavior of water and gas injection wells, and sealing potential in conventional reservoirs and carbon sequestration (e.g., Armitage et al., 2011; Nourollah et al., 2015; Henderson and Pena, 2017; Mao et al., 2020). Mechanical anisotropy can affect initiation, propagation, containment, and geometry of artificial fractures in unconventional hydrocarbon extraction (e.g., Khan et al., 2012; Waters et al., 2012; Zeng et al., 2019; Wang et al., 2021), and control slope stability for geohazard assessment (e.g., A. L. O'Neill, 1963; Huang et al., 2016).

Consistent with field and modeling studies, anisotropy promoted by grain-fabric alignments in MTDs has implications for petrophysical and mechanical heterogeneity, but the primary controls on grain-fabric alignments in MTDs are poorly understood. Furthermore, carbonate MTDs may have an even higher probability to be anisotropic due to the abundance of elongated skeletal grains compared to their siliciclastic counterparts. This research contributes on improving the predictability of grain-fabric alignments in mixed carbonate-siliciclastic MTDs, with emphasize on the following key questions:

1) What is the best model to represent the three-dimensional orientation of grain-fabric in MTDs?
2) Are grain-fabric alignments heterogeneous (e.g., across different samples, under different scales)?
3) Are grain-fabric alignments controlled by the styles of microstructures (i.e., deformation confined within a single bed, Amerman et al. 2011), the presence of clay, and grain lengths?

This paper addresses these key questions not only qualitatively, but also in quantitative manner that is commonly overlooked. In addition, we demonstrate how our research supports the interpretation from earlier study regarding the origin of microstructures and grain-fabric alignments in the area of interest. We also discuss how this study (1) improves the paleotransport interpretation of the Cutoff MTD, (2) proposes factors that may impact anisotropy, (3) provides a model to predict grain-fabric alignments from different datasets (e.g., seismic), and (4) helps delineate the direction of future studies.

2.3 Geological Context

2.3.1 Regional

The Permian Basin was formed during the Carboniferous due to collision of the Laurentia and Gondwana Continents along the Marathon - Ouachita Thrust Belt, which overprinted the ancestral Precambrian Tobosa Basin (Galley, 1958; Horak, 1985; Yang and Dorobek, 1995). Differential subsidence and uplift of basement blocks divided the Permian Basin into the Delaware and Midland sub-basins, which are separated by a Northwest-to-Southeast trending Central Basin Platform (Hills, 1984b; Horak, 1985; Yang and Dorobek, 1995) (Fig. 2.1A). The Cutoff Formation was deposited on the northern shelf margin of the Delaware Basin during the

late Leonardian regional shoreline transgression and the subsequent regression/progradation during the early Guadalupian (Kerans and Fitchen, 1995). Deposition of the Cutoff Formation was strongly controlled by the inherited paleo-topography of the underlying Leonardian shelf margin (Hurd et al., 2016) (Fig. 2.1B). The Cutoff Formation is bounded by unconformities at its top and base, with the most significant erosion focused near the shelf edge (Harris, 1987).

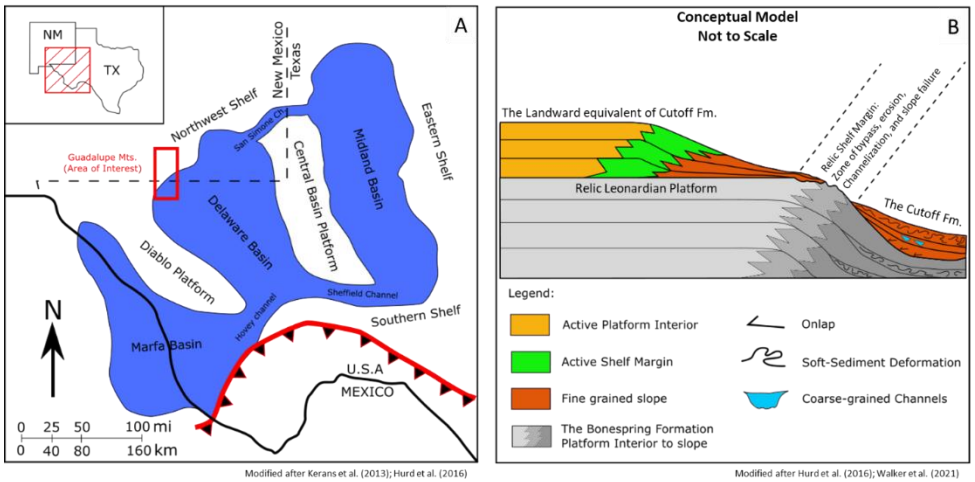

Figure 2.1 (A). Basin Configuration: The Permian basin is divided into the Delaware Sub-basin and the Midland Sub-basin by the Central Basin Platform. The research area is signified by the red square (Guadalupe Mts.). (B) A simplified diagram adopted from Hurd et al. (2016) and Walker et al. (2021): the deposition of Cutoff Formation had been influenced by the drowned Leonardian Platform and Shelf Margin.

2.3.2 The Cutoff MTD

Mass-transport deposits of the Cutoff Formation (fine-grained carbonate and siliciclastic) are concentrated in the upper part of the succession and have been studied in both proximal (Hurd et al., 2016) and distal locations (Amerman et al., 2011) to some details. The large-scale (meters to decameters) deformations are comprised of open symmetrical folds that become increasingly recumbent basinward, and truncation/termination surfaces (Amerman et al., 2011; Hurd et al. 2016). The termination surfaces generally dip between 0^0 - 30^0, can be of local- or

regional-scale, sometimes serve as a boundary between different deformation styles and lithofacies, and have been interpreted as faults / internal shear surfaces (see Le Goff et al., 2020), and/or glide planes separating different mass-transport events (interpreted as 3 to 6 events) (Amerman et al., 2011; Hurd et al., 2016). The multiple MTDs hypothesis is supported by the existence of localized, seemingly undeformed intervals draping on some termination surfaces (Amerman et al., 2011) (also see Armitage et al., 2009), which suggest pulses of coeval mass failures. The MTD-related microstructures (centimeter- to millimeter-scale) documented in the Cutoff Formation include microfolds, microboudins, normal and reverse microfaults, and tension gashes, all of which are confined within single beds, form lineation when intersecting their host bedding planes, and are unevenly distributed throughout the outcrops (Amerman et al., 2011). Zones of abundant microstructures are bounded by termination surfaces (Amerman et al., 2011). The paleotransport direction of the Cutoff MTDs inferred from fold axes and shortening lineations is N-S to NNW-SSE (Amerman et al., 2011), while extensional lineations give ENE - WSW. This study references only to the N-S to NNW-SSE paleotransport direction, as the methods are more well-established (see Strachan and Alsop, 2006; Alsop and Weinberger, 2020). The paleotransport direction of the Cutoff MTDs is therefore oblique to the paleoslope (Fig. 2.2), similar to an upper Leonard MTDs documented in the Midland Sub-basin (see Bhatnagar et al., 2019). Post-lithification overprinting that occurs within the units has distinctive trends as compared to the soft-sediment deformation (Amerman et al., 2011): (1) Regional flexure in the basin trends WNW in the southern part and NW in the northern portion, (2) minor post-Guadalupian deformation has NE-SW shortening trend (Erdlac, 1993), and (3) kilometer-length normal faults, which penetrate through several formations, dominantly strike NW (Hills, 1984b; Kullman, 1999).

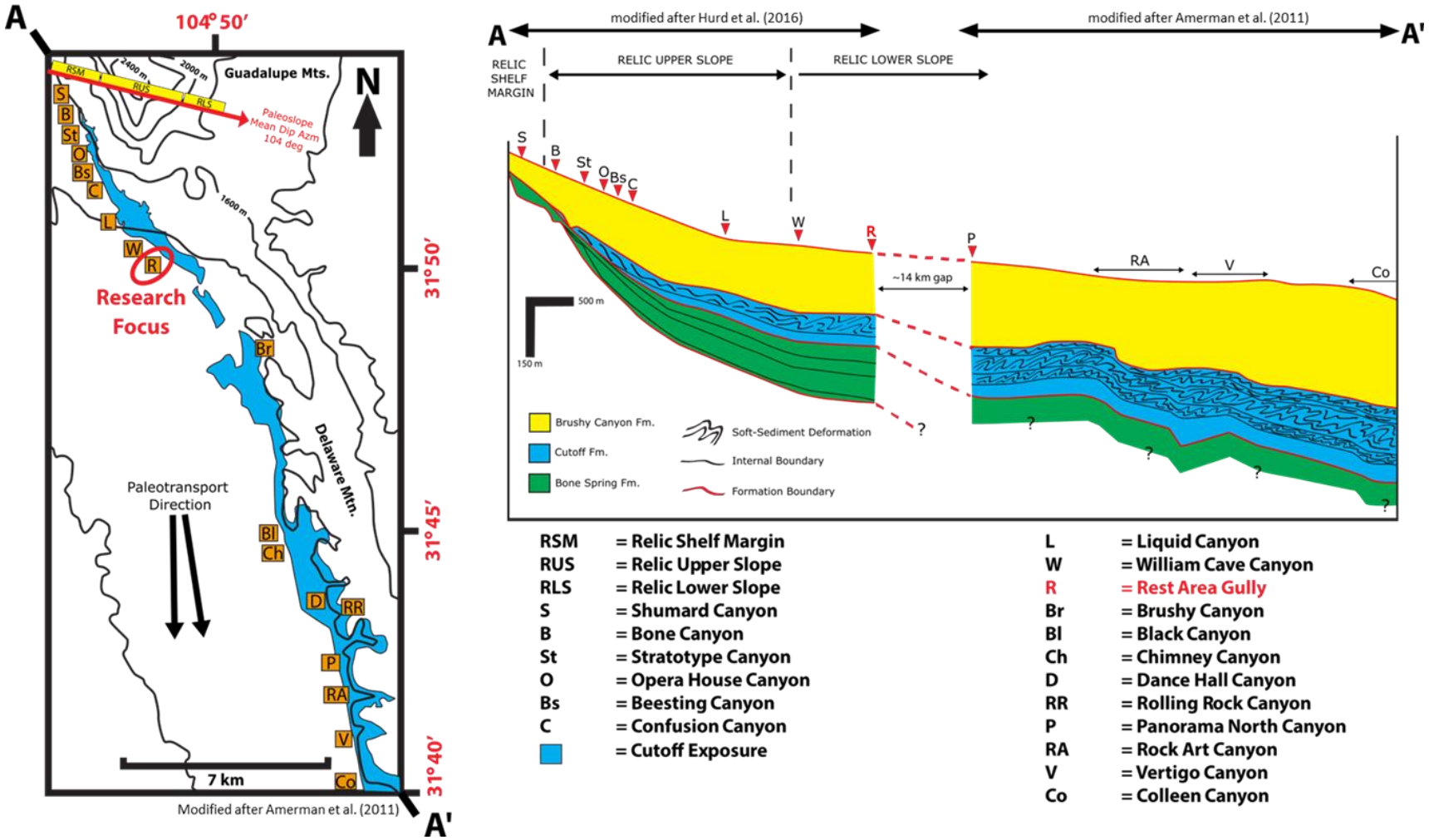

Figure 2.2 The Stratigraphy of Cutoff Formation has been mapped in detail by Amerman et al. (2011) and Hurd et al. (2016). The multi-scale deformations in the unit of interest are confined within the top portion of the Cutoff Formation. The deformation intensity increases basinward. The overall paleotransport direction is N-S to NNW - SSE, which is oblique to the paleoslope. This study focused on the Rest Area Gully locale (relic lower slope).

2.3.3 Area of Interest

Our study focuses on a 15 m thick cliff-face outcrop (the Snake Rock) of the Rest Area Gully locale (Fig. 2.2) (herein area of interest) where the Cutoff Formation is well-constrained paleogeographically and has excellent exposure (see Simabrata et al., Part A). The lithofacies in general consists of centimeter- to millimeter-thick, clay-rich and carbonate-rich packstone to wackestone (Dunham, 1962), with prolific silt-sized sponge spicules and minor bioclasts that include radiolaria, ostracods, and foraminifera (also see Hurd et al., 2016). Termination surfaces manifest as thin fissile layers that cut through beds and slump folds, and can merge into adjacent horizontal beds when traced. These surfaces partition the outcrop into three segments with distinctive lithofacies characteristics (termed B, C, and D), and several sub-segments that are rich in microstructures (Fig. 2.3) (see Simabrata et al., Part A). This research focuses on three sub-segments, which characteristics are described as follows:

(1) Sub-segment B1 consists of alternations of light-gray resilient limestone and thinner dark-grey fissile limestone. This zone is dominated by extensional microfractures that have the appearance of ‘tiger stripes’ and are darker than the surrounding material, very similar to ‘tension gashes’ described by Amerman et al. (2011). The spacing of extensional microfractures ranges from 5 – 10 mm. The microfractures dominantly strike N-S, with vertical dip.

(2) Sub-segment B2 consists of alternating beds of light-grey resilient limestone, with darker cm- to mm-scale internal sedimentary packages (herein microbeds), and thin dark-grey fissile limestone. The darker microbeds in resilient limestone layers form primarily asymmetrical microboudins and small isoclinal microfolds. The wavelengths of the

microstructures are about 1 – 5 mm, with an amplitude range of 1 – 2 mm. The microstructures dominantly strike W-E and dip gently upslope.

(3) Sub-segment C2 comprises light-brown resilient limestone (with dark-grey to light-grey microbeds) alternating with dark-grey fissile limestone. The main microstructures are large isoclinal microfolds that involve several microbeds in resistant limestone, associated with microboudins and extensional microfractures. The wavelength of large microfolds is 15 mm in general, with an amplitude range of 8 – 10 mm. The microfolds overall strike NW – SE coupled with relatively steeper dip compared to those of Sub-segment B2.

The siliceous components are responsible for the color variations and differential weathering observed in the field. The profusion of spicule grains (prolate-shaped) allow for detailed inspections of grain-fabric alignments in the Cutoff MTD. For this research, we collected one representative oriented sample (resilient beds) from the sub-segments of interest (see Fig. 2.3). Oriented samples for the fissile counterparts are difficult to recover and therefore not included in our study. In addition to the microscopic characterizations, we also measured the orientations of outcrop-scale slump folds, isoclinal microfolds, and extensional microfractures in all sub-segments to assist our interpretations.

2.4 Methods

We utilized spicule long-axis orientations to model the mean trend, mean plunge, and wellness of grain-fabric alignments. The mean trend and plunge of spicules reveal their three-dimensional configurations. Alignment wellness can be used as a metric to discern the effect of different long-axis lengths, clay mineral, and microstructure types on grain-fabric alignments.

The methodology in this research is tailored to collect spicule data that can represent the whole thin sections, as well as the internal fine-scale heterogeneity.

2.4.1 Sample Preparation and Analysis

For each oriented sample, large-format (7.62 x 5.08 cm) thin sections were cut in three orientations: 1) parallel to the bedding plane, 2) parallel to the strike of the observed microstructures (herein strike-parallel) and 3) perpendicular to the strike of the observed microstructures (herein strike-perpendicular) (Table 1). The thin sections are 15μ thick with blue epoxy to highlight porosity, and half of each thin section was stained with alizarin red to indicate calcite or dolomite content. All thin sections were photographed using a high-resolution digital microscope (Keyance – VHX 700 Series) at 300x magnification.

For analysis of spicule orientation, each high-resolution thin-section photograph was divided into a grid, with 'slice' area of 2000 x 2000 pixels each (about 5 mm^2; Fig. 2.4). Using a Python script, we collected spicule orientation from every other row and column (counted from the top left corner, see Fig. 2.4) of the thin sections. We utilized a grid of 100 open circles overlain on each slice, and measured spicules that intersected these circles in order to reduce measurement bias (Fig. 2.4), similar to the Gazzi-Dickinson point-counting method for sandstone petrography (Graham et al., 1976; Dickinson and Suczek, 1979; Ingersoll, 1984). We also sampled the short-axes of spicules in thin section C2[BED] for aspect ratio calibration. In addition, we also collected a secondary dataset with larger slice area (4000 x 4000 pixels, or ~20 mm^2) and 225 circles per slice. This secondary dataset enables the acquisition of a sufficiently large sample-size in each slice for comparing spicule orientations with different matrix compositions.

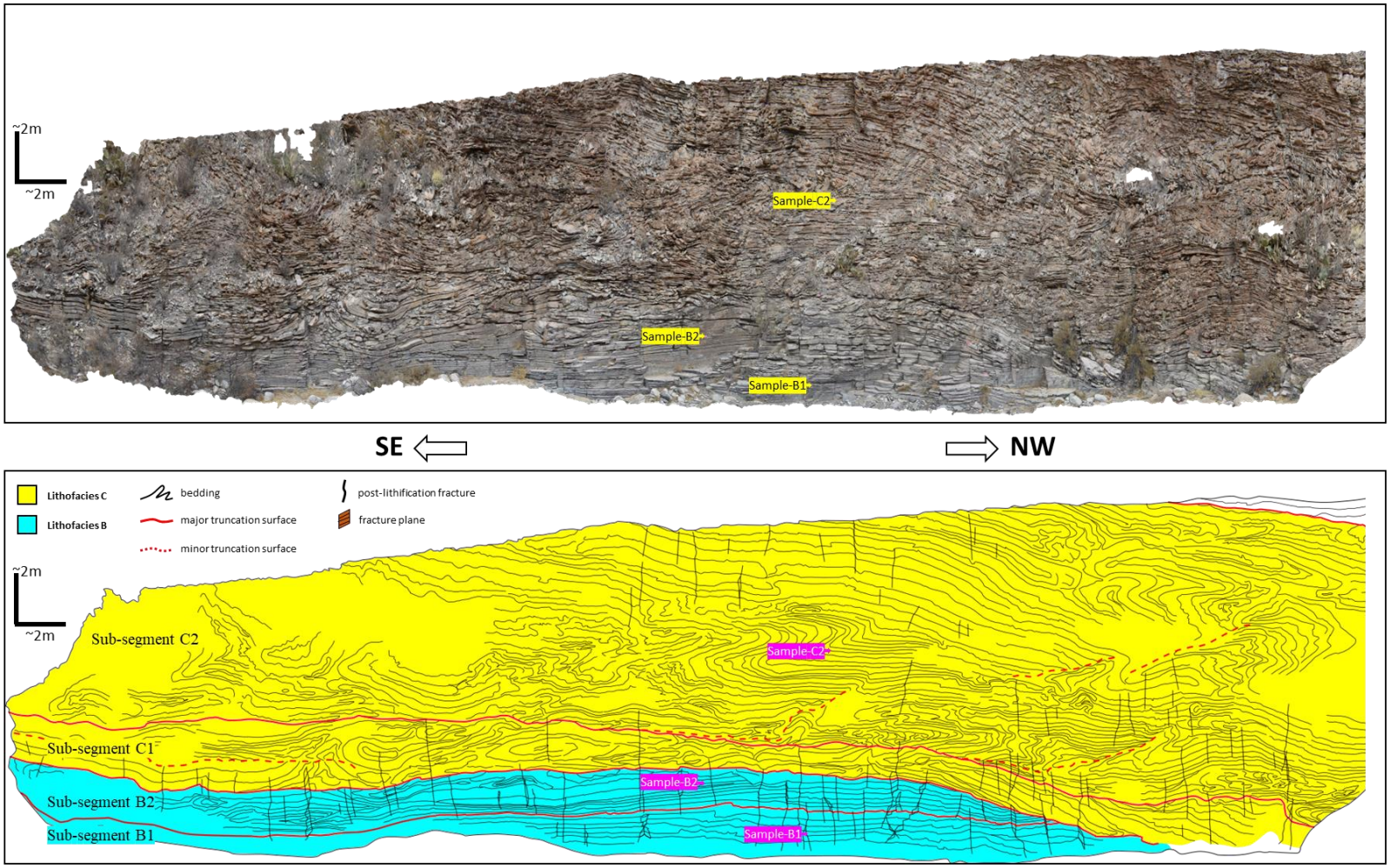

Figure 2.3 The Uninterpreted (upper figure) vs. interpreted (lower figure) outcrop photomosaic of the area of interest: The outcrop is divided into three segments with distinct lithofacies characteristics, i.e., segment B, C, and D (segment D is not shown), as well as sub-segments termed B1, B2, C1, and C2. This research focuses on sub-segment B1, B2, and C2. Sub-segment B1 is dominated by extensional microstructures, similar to tension gashes observed by Amerman et al. (2011). Sub-Segment B2 are dominated by asymmetrical microboudins and small asymmetrical (isoclinal) microfolds, while C2 is dominated by large asymmetrical (isoclinal) microfolds. Note that sample B2 represents predominantly small asymmetrical microfolds.

Table 2.1 Summary of Data Availability: All thin sections in this table are in cross-polarized light. Cartoons to the right illustrate the plane orientations of strike-parallel and strike-perpendicular thin sections.

Segment Name	Microstructure Type	Outcrop Image	Perpendicular to the Strike of Microstructures	Parallel to the Strike of Microstructures	Bedding Plane Thin Sections	
Sub-Segment B1	Extensional Microfractures		B1 [PERP] - 0 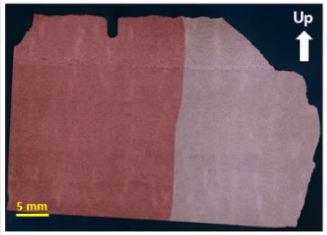	B1 [PAR] - 90 	B1 [BED] 	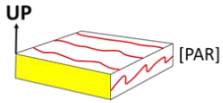
Sub-Segment B2	Small Isoclinal Microfolds		B2 [PERP] - 290 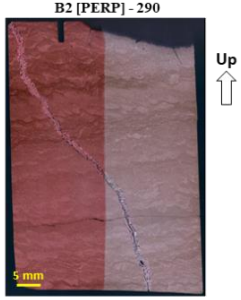	B2 [PAR] -200 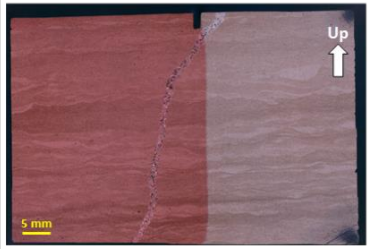	B2 [BED] 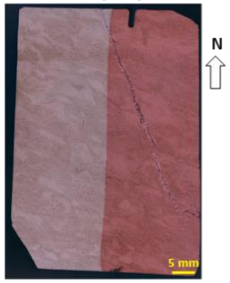	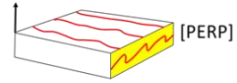
Sub-Segment C2	Large Isoclinal Microfolds		C2 [PERP] - 316 	C2 [PAR] - 46 	C2 [BED] 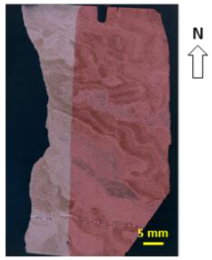	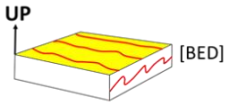

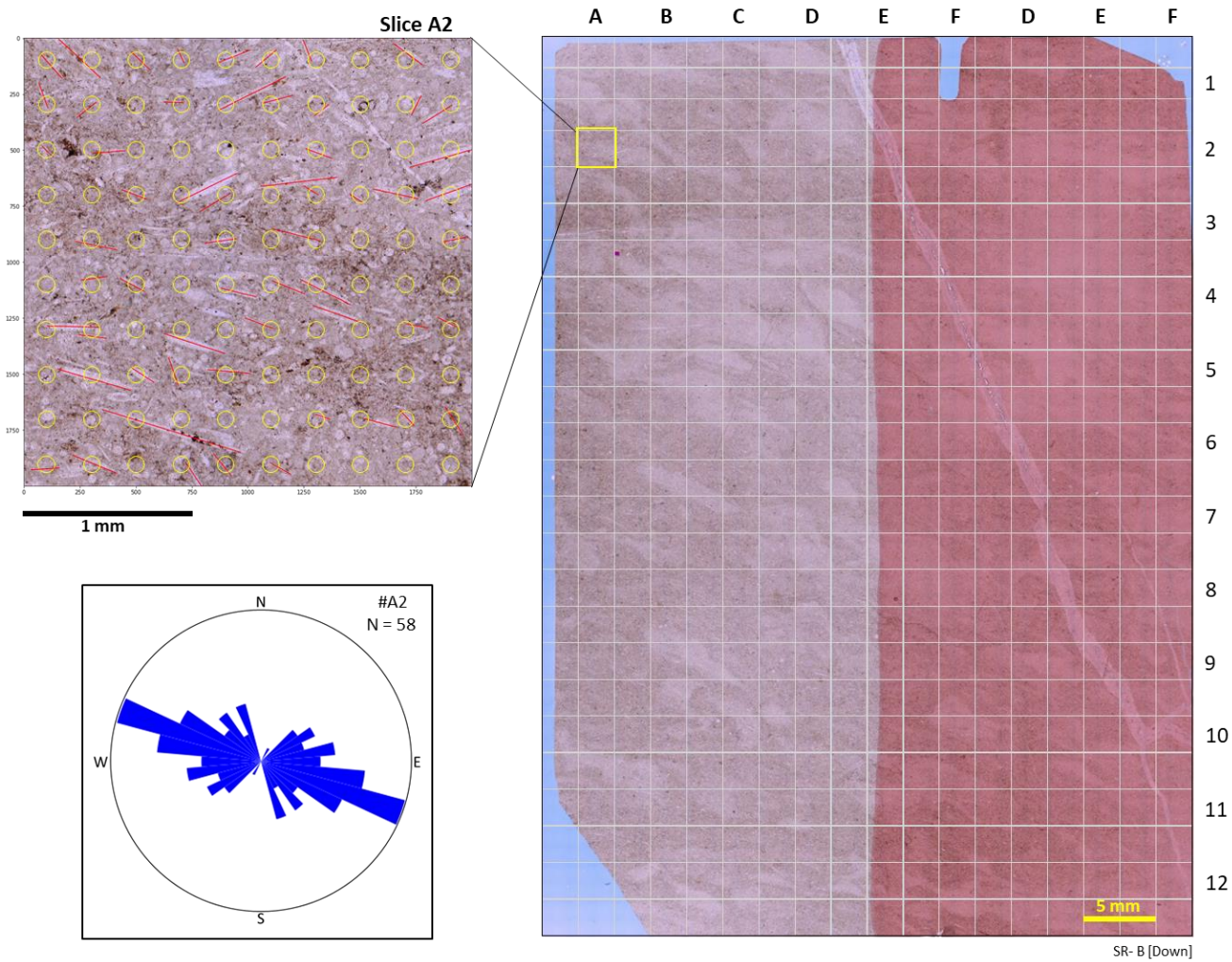

Figure 2.4 The right-hand figure illustrates how each thin section is divided into grid of slices. The observed and measured slices were coded as rows (A, B, C, …F) and columns (1, 2, 3,… 12). The upper left figure is the zoom-in of slice A2. One hundred circles were assigned to emulate point-counting. The measurements from each slice were plotted to a rose diagram and analyzed quantitatively.

We recognize that we are measuring the 3D orientation of spicules on a 2D plane, and that some spicules that are perpendicular to the thin section plane are not counted, as they appear circular (Fig. 2.4). While high-resolution 3D imaging may result in more accurate orientation, we did not have access to such techniques for our samples. We mitigate these issues using a statistical analysis of the three thin-section orientations for each sample.

2.4.2 Quantification of Spicule Orientations

Spicule orientations are axial measurements (bidirectional), and as such we compute the azimuth of each spicule and its 180° counterpart (e.g., 045° and 225°) using the pair of points that defines the spicule orientation. We employed vector projection to delineate two important parameters of spicule alignments used throughout the paper: (1) the dominant / mean orientation of spicules, and (2) the wellness of alignments.

Suppose that we have a series of axial measurements (θ1, θ2, ... θn) and an arbitrary line (δ) plotted to a cartesian coordinate (Fig. 2.5A). Assuming the lengths of all lines are equal to one, the mean of squared projections (P^2_{avg}) of all azimuth data (θn) compared to the arbitrary line δ is given as:

$$P^2_{avg} = \frac{1}{n} \Sigma \left(\mathrm{Sin}\Theta n.\mathrm{Sin}\delta + \mathrm{Cos}\Theta n.\mathrm{Cos}\delta\right)^2 \qquad (2.1)$$

A line that represents the dominant trend (α line) of the dataset gives the largest P^2_{avg}. Conversely, a line that is normal to the dominant axis, herein subordinate axis (Ω line), gives the least P^2_{avg}. A constant P^2_{avg} in all compass directions indicates circular symmetry of axial data (i.e., no dominant axis) (Fig. 2.5B). Solving for the maxima of P^2_{avg} (first-order derivative), we get:

$$\frac{dP^2\text{avg}}{d\delta} = 0$$

$$\delta\,\text{max} = \alpha\ line = \frac{1}{2}\ Arctan\left(\frac{Avg\ [Sin2\theta n]}{Avg\ [Cos2\theta n]}\right) \tag{2.2}$$

If we define the bidirectional error (B-Err) as the mean angle difference between the axial data (θn) and the dominant axis (α line), the mathematical expression can be written as:

$$\text{B-Err} = \frac{1}{n}\Sigma\ \text{Arccos}\ |sin\theta n.sin\alpha\ \ + cos\theta n.cos\alpha| \tag{2.3}$$

Note that absolute value is added to take out the excess 180 degree from conjugate axial data of the opposite quadrants, a necessity for bidirectional datasets (similar to mean squared error calculations for unidirectional datasets). The dominant axis (α line) and the subordinate axis (Ω line) also give the minimum and maximum angle of error (B-Err), respectively (Fig. 2.5B). Therefore, the α line provides a least-error axis that can be a proxy for the mean of axial data. As axial data approaches circular symmetry, the value of B-Err becomes closer to 45 degree.

Finally, we define that the difference between maxima and minima of mean squared projections (ΔP^2_{avg}) is a measure of alignment wellness, such that ΔP^2_{avg} =1 indicates that all axial data are in perfect alignment, while ΔP^2_{avg} = 0 indicates that the axial data are of circular symmetry (Fig. 2.5C). Solving for ΔP^2_{avg}, we get:

$$\Delta P^2_{avg} = (P^2_{avg}\ \text{max} - P^2_{avg}\ \text{min})$$

$$\Delta P^2_{avg} = \sqrt{Avg[Sin2\theta n]^2 + \ Avg[Cos2\theta n]^2}\ ,\quad \text{for}\ \alpha = (\Omega \pm 90) \tag{2.4}$$

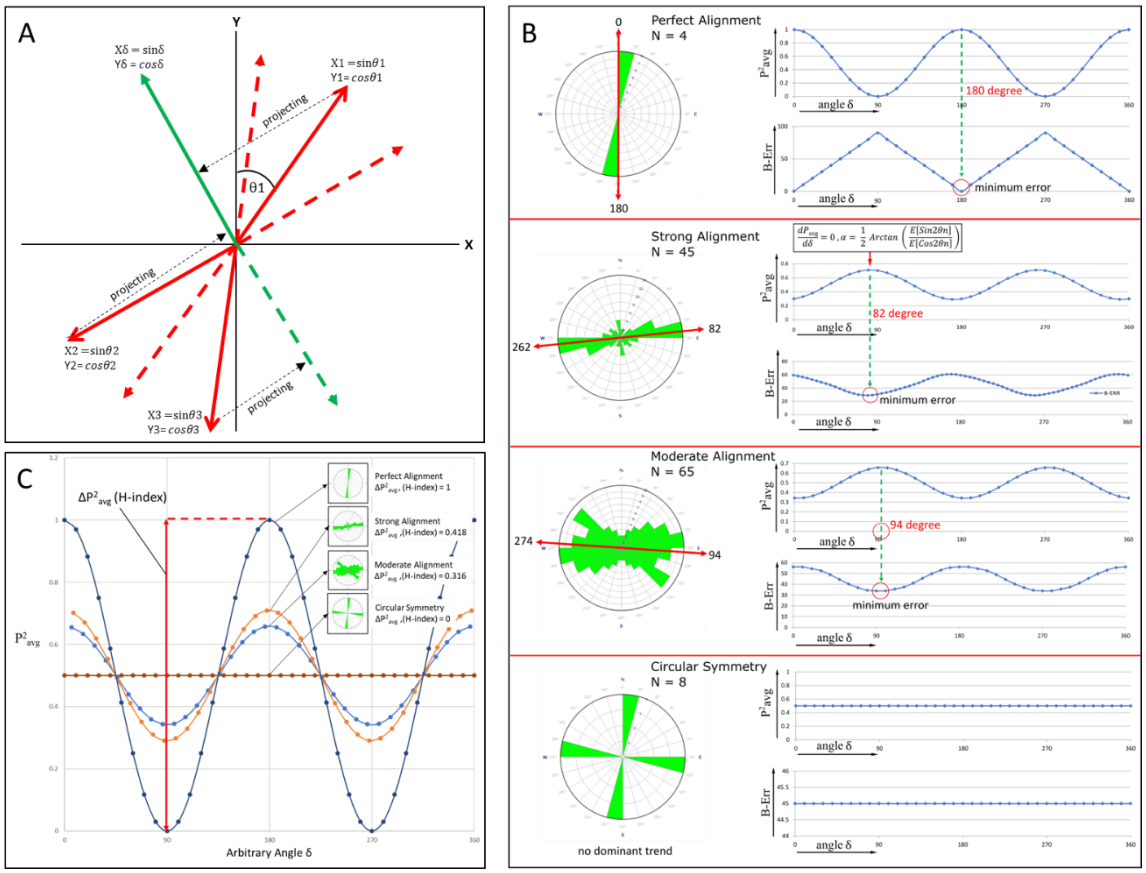

Figure 2.5 (A) This figure illustrates how axial data (red lines) are projected to an arbitrary line (green line). Dashed lines are conjugates of lines from the opposite quadrant. (B) Empirical examples from two real spicule measurements and two artificial data: Axial mean in this research is defined as the direction that gives maximum value for average of squared projections (P^2_{avg}), and at the same time gives lowest B-Err (similar to standard deviation). A condition of where no dominant direction exists is mathematically represented by a constant P^2_{avg} and B-Err. (C) When the peak of P^2_{avg} from all datasets shown in Figure 3B are normalized to 180° angle, we see that the difference of peak and through of P^2_{avg} (H-index) shrinks as the data become more and more dispersed around the circle.

Note that ΔP^2_{avg} in axial data is essentially the double-angle version of R in unidirectional data, which is commonly used for the same purpose as ΔP^2_{avg} (see Pewsey et al., 2013, page 32). From this section onward, the wellness of alignment ΔP^2_{avg} will be referred as H-index. H-index is also inversely proportional to B-Err, such that half the value of H-index translates to twice B-Err value, and hence twice as disorderly. Note that this method is also applicable to other types

of 2D axial data, and can be expanded into 3D space to characterize bidirectional 3D alignments, such as poles of fracture planes and metamorphic foliation.

2.5 Results

2.5.1 Lithofacies and Microstructure Types

Descriptions of lithofacies and microstructures in this sub-section focus on microscopic observations that encompass the lithologic texture based on Dunham (1962), as well as microstructure dimensions, orientation, and associated features. The lithofacies modifiers 'clayey' and 'clay-rich' are based entirely on qualitative visual inspections.

A. Sample B1 (Extensional Microfractures)

Sample B1 consists of granulose packstone encased in clayey packstone 'matrix', as well as fining-upward microbeds with sharp bases (Fig. 2.6A, B, C, and D). Small fractions of the grain and matrix have been silicified and pyritized. The microfractures are discontinuous vertical sheets that have both length and height of ~1 cm, and thickness of ~ 1 mm, and the interior is filled with packstone. The microfracture walls are poorly defined, not grain-penetrative, and more clearly visible under cross-polarized light. Spicule grains inside some of the microstructures are aligned parallel to sub-parallel the microfracture walls. The overall strike of microfractures in sample B1 is 166° – 346° with vertical dip, while the microbeds are parallel to the bedding plane (dip ~0°).

B. Sample B2 (Small Isoclinal Microfolds)

Sample B2 consists of thin packstone microbeds with fining-upward trends and sharp bases, interbedded with clayey packstone and clay-rich packstone (Fig. 2.7A, B, and C). Minor diagenesis includes silicification, pyritization (Fig. 2.7D) and calcite-filled fractures (Fig. 2.7A, B). Microfolds that deform the packstone microbeds are discontinuous (laterally

detached), have tapered edges, and are associated with normal to thrust microfaults, and microboudins. Some microbeds have been rotated and overturned, and the isoclinal microfolds prominently verge toward the south-southwest (the interpreted paleotransport direction, Fig. 2.7A). The overall strike of small isoclinal microfolds measured in sample B2 is 117°, with a mean dip of ~ 22° South.

C. Sample C2 (Large Isoclinal Microfolds)

Sample C2 consists of packstone, with thin interbeds of clayey packstone and clay-rich packstone (Fig. 2.8A). Neither fining-upward nor sharp bed bases are observed in Sample C2. Silica replacement zones are present at the base of clayey packstone microbeds and pyritization occurs locally (Fig. 2.8A, C). The isoclinal microfolds in sample C2 are larger and more continuous than those in sample B2. The minor microstructure association includes normal, thrust, and strike-slip microfaults, as well as a possible injection feature (Fig. 2.8A). The laterally detached edges of folded microbeds are tapered. Several calcite-filled fractures are present (Fig. 2.8A, B). The overall strike of large isoclinal microfolds in sample C2 is 120°, with a mean dip of ~ 38° North.

2.5.2 Spicule Orientations

To represent the 3D orientation of spicules, we use three thin sections from each sample whose planes are normal to one another (Table 1). Hereafter, the term ‘plunge’ refers to spicule orientation in strike-parallel and -perpendicular thin sections, while the term ‘trend’ refers to spicule orientation in bedding-plane thin sections. Furthermore, the term ‘overall’ (e.g., overall mean spicule trend, overall H-index) represents the entire thin section, while the term ‘local’ or ‘fine-scale’ (e.g., local mean spicule trend, fine-scale H-index) refers to individual slices (see Fig. 2.4).

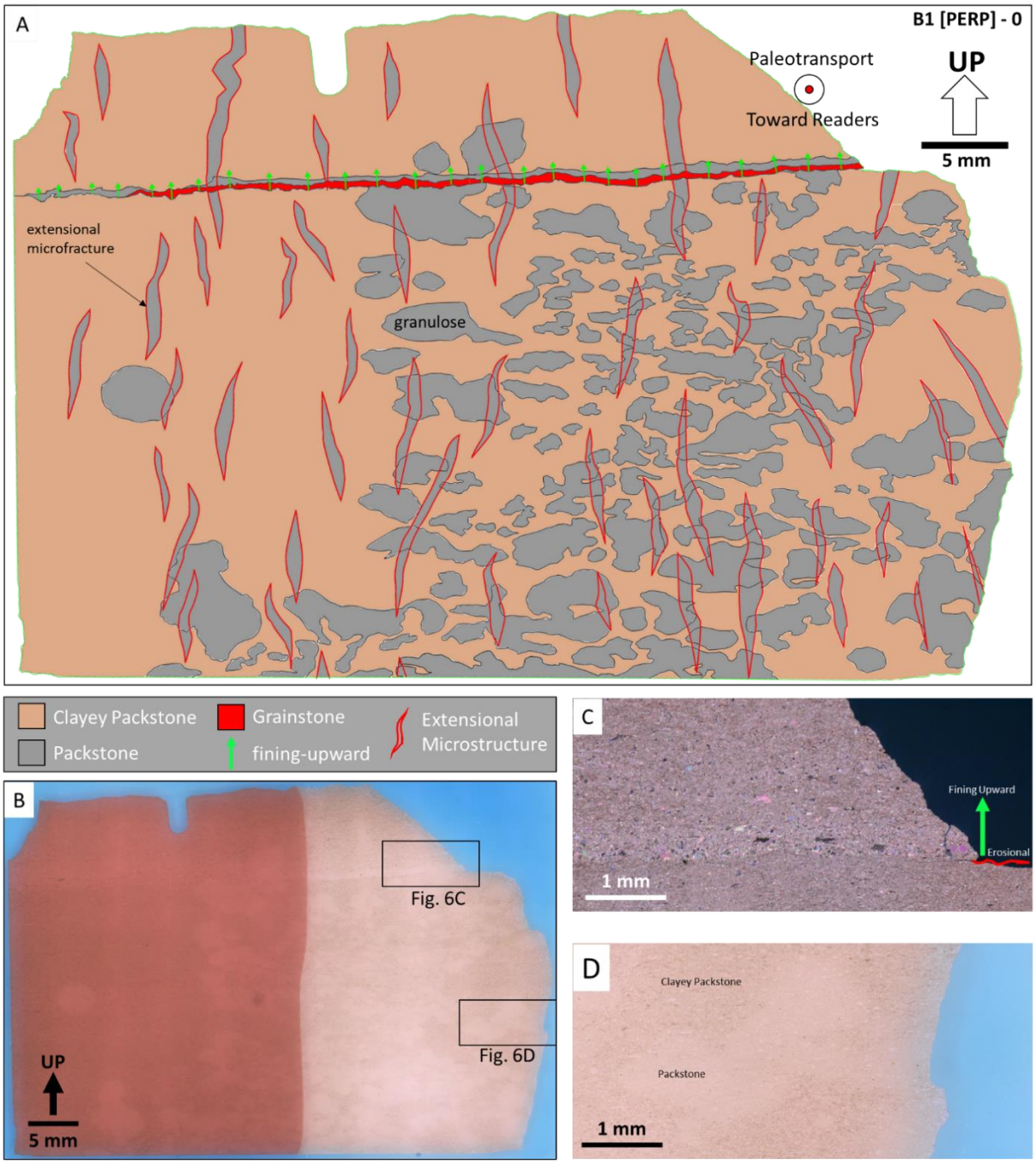

Figure 2.6 (A) An example of interpreted thin section, B1 [PERP] - 0: The lithofacies consist of granulose packstone, surrounded by clayey packstone 'matrix'. The most prominent microstructures are packstone-filled extensional microfractures; highly discontinuous with typical length and height of ~1 cm or less, and width of about 1 mm. These microfractures are only visible in cross-polarized light. (B) Uninterpreted thin section B1 [PERP] - 0: the two small boxes represent the zoom-out versions of Fig. 2.6C and Fig. 2.6D. (C) Fining-upward microbed with an erosional base. (D) Contrast between granulose packstone and clayey packstone.

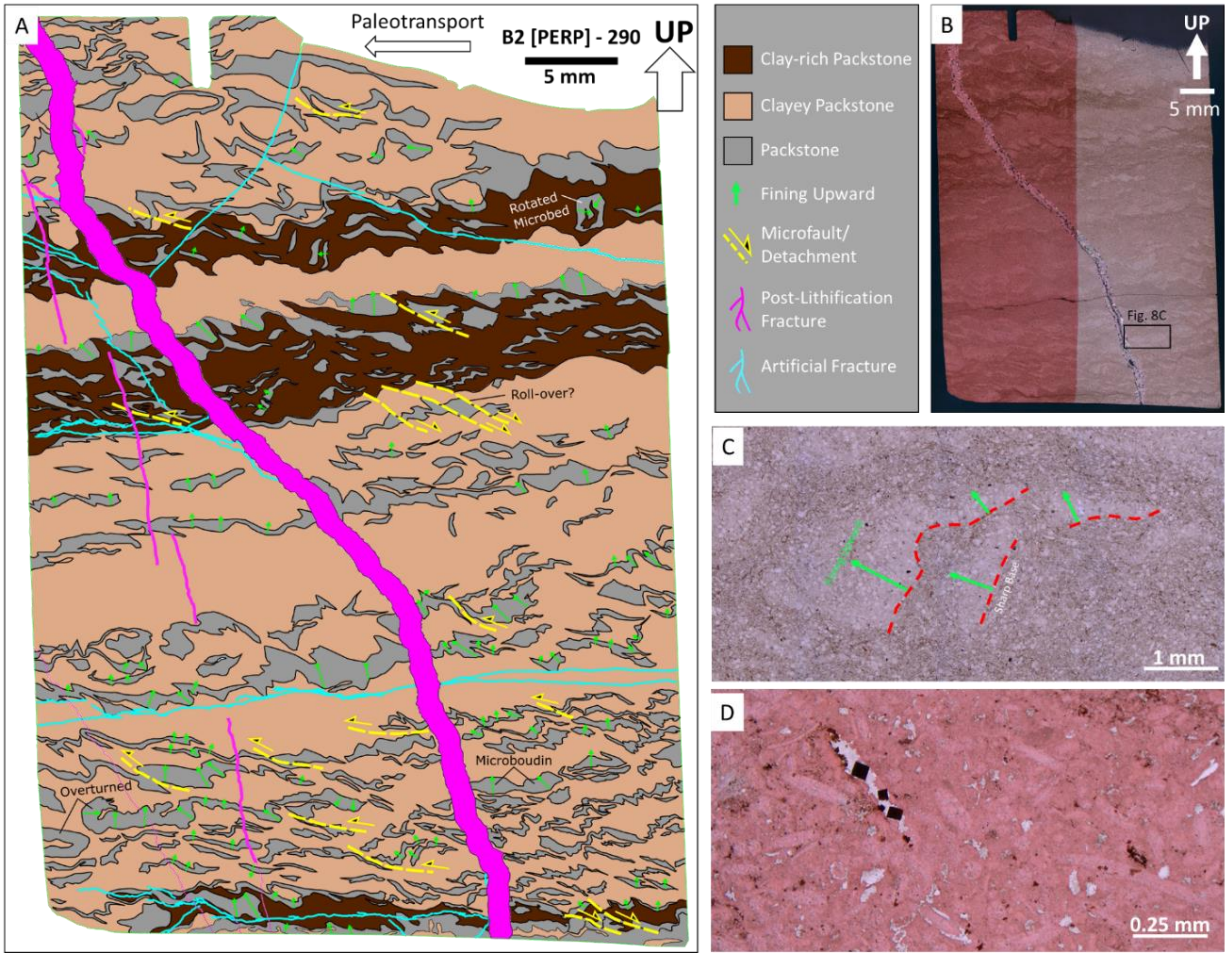

Figure 2.7 (A) An example of interpreted thin section, B2 [PERP] - 290: The dominant lithofacies are clayey packstone, followed by clay-rich packstone, and packstone with fining-upward features and sharp bases. The microstructures are isoclinal microfolds that verge downslope. Isoclinal microfolds involving packstone microbeds are discontinuous (detached) with tapered edges. Minor microstructures include thrust and normal microfaults, and microboudin. (B) Uninterpreted thin section B2 [PERP] - 290: The two small boxes represent the zoom-out versions of Fig. 2.7C. (C) Detached microbeds with fining-upward sequence and sharp bases. (D) Replacement - from thin section B2 [BED]: Red zones are dominantly calcite, white zones are silicified, and black zones (opaque) are pyritized.

A. Strike-parallel perspective

The overall mean spicule plunge in sample B1[PAR]-90 and B2[PAR]-200 are essentially horizontal (~0°), with overall H-index of 0.83 and 0.76, respectively, coinciding with the dip of microbeds as measured in the thin sections, which are also horizontal (~0°)

(Fig. 2.9A and Fig.2.10A). Close inspection of individual slices reveals that the fine-scale (5 mm^2) spicule orientations also follow the local apparent-dip variations, e.g., B1[PAR]-90 slices A6 to L6 (Fig. 2.9A) and B2[PAR]-200 slice A3 to L3 (Fig. 2.10A). The spicules in sample C2[PAR]-46 are plunging 25° NW and 25° SE, with an overall mean of ~0° (overall H-index = 0.38). Local spicule plunges also follow the local apparent-dip of microbeds, e.g., slices F4 to H4 (Fig. 2.11A), and therefore similar to the pattern observed in the former two samples.

B. Strike-perpendicular perspective

The overall mean spicule plunges in sample B1[PERP]-0 is about horizontal (~0), strongly in agreement with the overall mean apparent-dip of microbeds as observed in the thin section (Fig. 2.9B). Spicules measured in sample B2[PERP]-290 and C2[PERP]-316 are plunging overall 21.6° toward NNE (overall H-index = 0.48) and 36.5° SW (overall H-index = 0.23), respectively. These values are only slightly deviated from the overall mean of apparent-dip of microbeds observed in the respective thin sections (Fig. 2.10B and 2.11B). Spicule alignments in individual slices in sample B2[PERP]-290 and C2[PERP]-316 are more chaotic, and sometimes tilted opposite to the overall mean plunge in accordance to the change of local apparent dip (e.g., slice F4 in Fig. 2.11B). This variation results in much lower overall H-index in B2[PERP]-290 and C2[PERP]-316 as compared to sample B1[PERP]-0. The key observation from the strike-perpendicular perspectives is that the plunges of spicules reflect the apparent-dip of microbeds in which they are measured, and therefore consistent with the strike-parallel perspectives. The implication of this finding extends to the measured trends of spicules in bedding-plane perspective, which require dip-correction / restoration in order to accurately quantify the H-index.

C. Bedding-plane perspective

The local mean spicule trends in sample B1[BED] are quasi-perpendicular to the local strike of extensional microfractures (Fig. 2.9C). Only a few slices show parallel to sub-parallel orientation with respect to the local microstructures, e.g., B1[BED] slice #C2, A5, D6, E8 (Fig. 2.9C). These local trends are reflected in the overall trend, with the overall mean spicule trend 260° – 80° (WSW - ENE), (H-index of 0.16), essentially transverse to the overall mean strike of extensional microfractures (346° – 166°) (Fig. 2.9D, Fig. 2.12A). A dip correction is not necessary for sample B1 because the microbeds are horizontal.

In sample B2[BED], the local mean spicule trends are parallel to sub-parallel to the local strike of isoclinal microfolds (Fig. 2.10C). Variations in local mean spicule trend are influenced by the local microstructure strike adjacent to them, e.g., compare B2[BED] slice A10, B10, C10, and D10 (Fig. 2.10C). The overall mean spicule trend dues $283^{0°}$– 103° (WNW – ESE), with H-index of 0.47. This well-aligned spicule trend deviates only 14° from the mean strike of microstructures (297° – 117°) (Fig. 2.10D, Fig. 2.12B). Applying dip correction does not change the orientation or the H index significantly (by 2° and 0.03, respectively).

The local mean spicule trends in sample C2[BED] are in strong agreement with the local strike of isoclinal microfolds, as shown in Figure 2.11C. Furthermore, slices that cover areas with high strike curvature, (e.g., C2[BED] slice B4, and G7) (Fig. 2.11 C, Fig. 2.12C), show more chaotic and sometimes multimodal orientations, and thus exhibit a low local H-index. In contrast, areas with low curvature have strongly unimodal orientations and high local H-index (e.g., C2[BED] slice C6, and D7) (Fig. 2.11C, Fig.12C). The overall mean spicule trend is 299° – 119° (H-index = 0.37), within 3° of the overall mean strike of

microstructures (Fig. 2.11D). Dip correction does not affect the overall mean trend, but notably decreases the H-index from 0.37 to 0.26 (Fig. 2.11D).

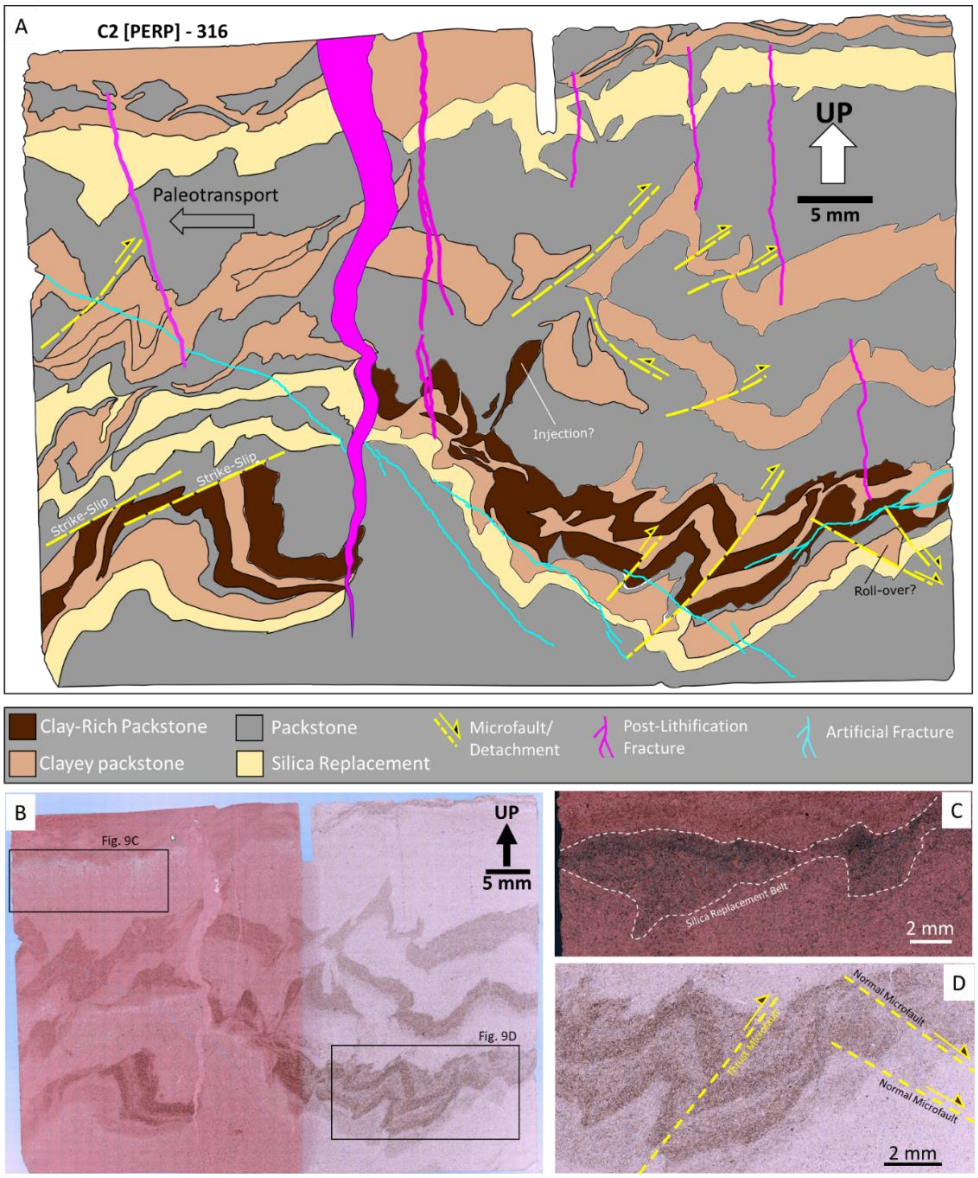

Figure 2.8 (A) An example of interpreted thin section, C2 [PERP] - 316: The composition consists of alternating clayey and clay-rich packstone, surrounded by packstone. Silica replacement belts commonly occupy the base of clayey packstone microbeds. The dominant microstructures are isoclinal microfolds (larger and more continuous than sample B2), with the crests verging upslope. Minor features are thrust, normal, and strike-slip microfaults, as well as a possible injection. (B) Uninterpreted thin section C2 [PERP] - 316: The two small boxes represent the zoom-out versions of Fig. 2.8C and Fig. 2.8D. (C) Silica replacement belt under cross-polarized light. (D) Thrust and normal microfaults.

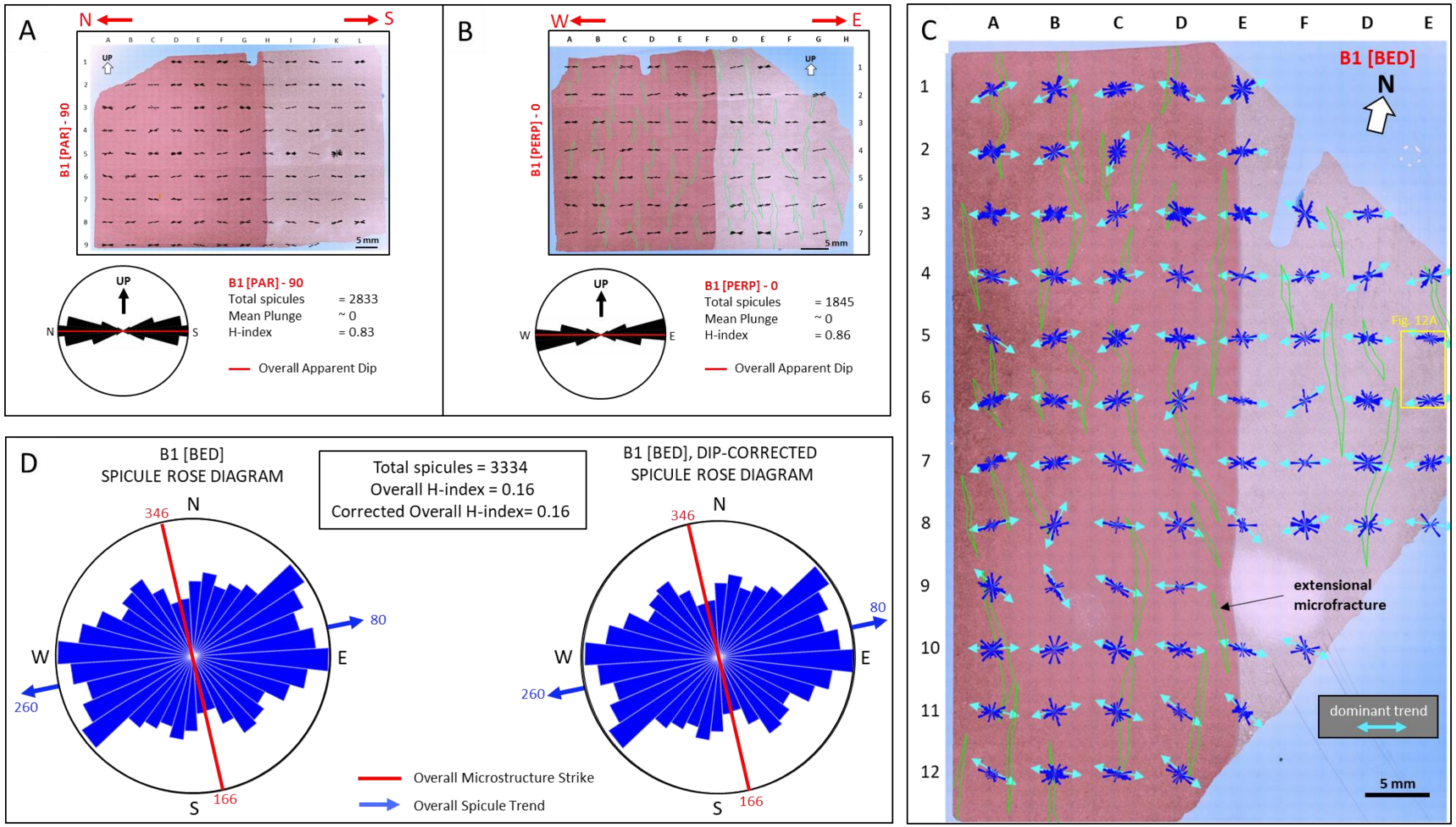

Figure 2.9 (A) The mean spicule plunge in B1[PAR]-90 is horizontal, strongly following the apparent-dip of microbeds. (B) The mean spicule plunge in B1 [PERP]-0 is also horizontal, mimicking the apparent-dip of microbeds. (C) In the bedding-plane thin section, B1 [BED], the fine-scale spicule trends are overwhelmingly perpendicular to the direction of microfractures, albeit with minor parallel to sub-parallel variants. (D) The Original vs. dip-corrected rose diagram of spicule trends observed in B1 [BED].

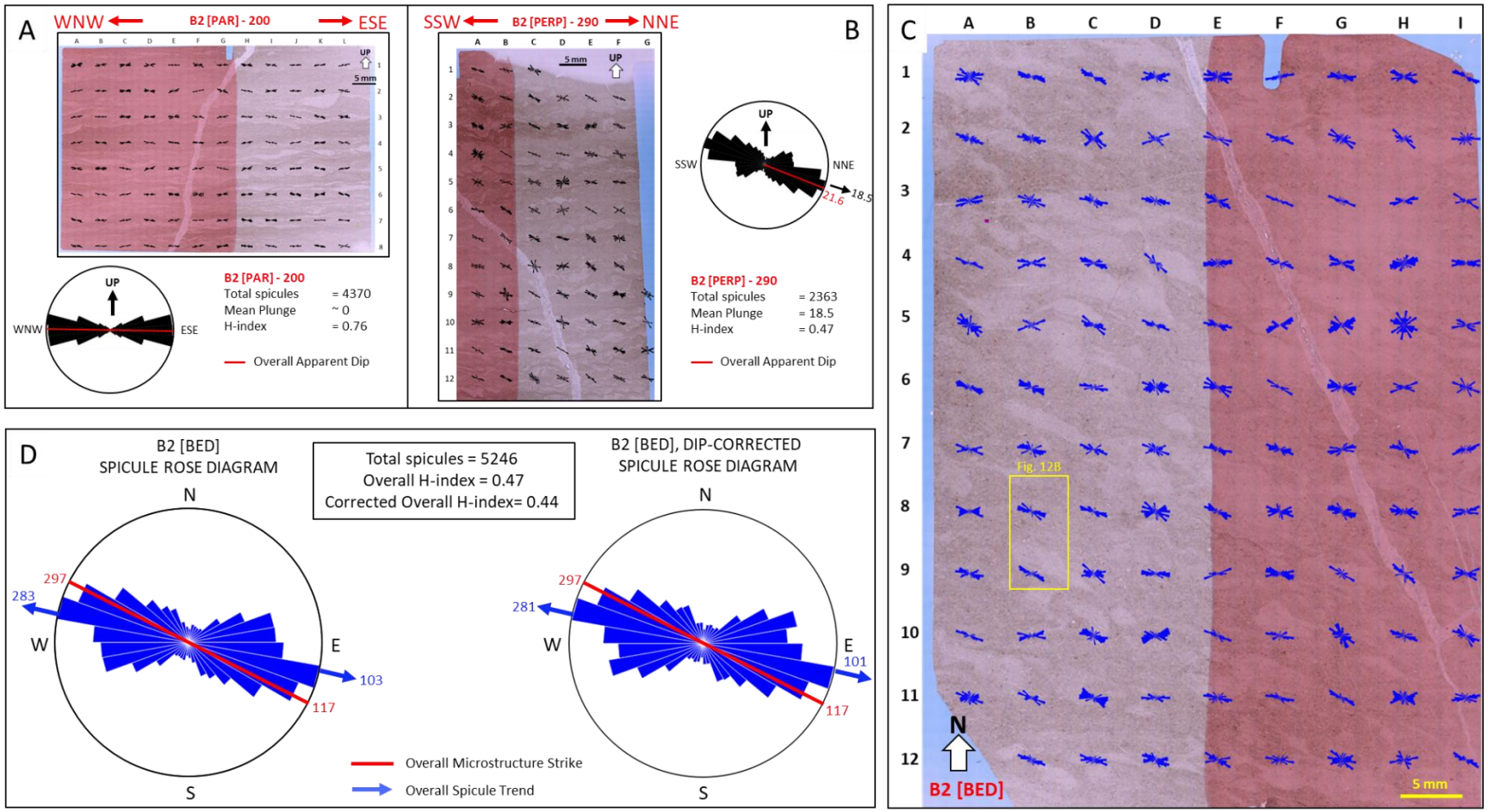

Figure 2.10 (A) The overall mean spicule plunge in B2 [PAR]-200 is about horizontal, similar to the overall mean apparent-dip of microbeds. In fine-scale, the plunge varies in accordance to the local apparent-dip of microbeds. (B) The overall mean spicule plunge in B2 [PERP]-290 almost coincides with the overall mean apparent-dip of microbeds. In fine-scale, the plunge varies in accordance to the local apparent-dip. (C) The bedding-plane thin section B2 [BED] shows that local mean spicule trends are mostly parallel to the local strike of microfolds. (D) The Original vs. dip-corrected rose diagram of spicule trends observed in B2 [BED].

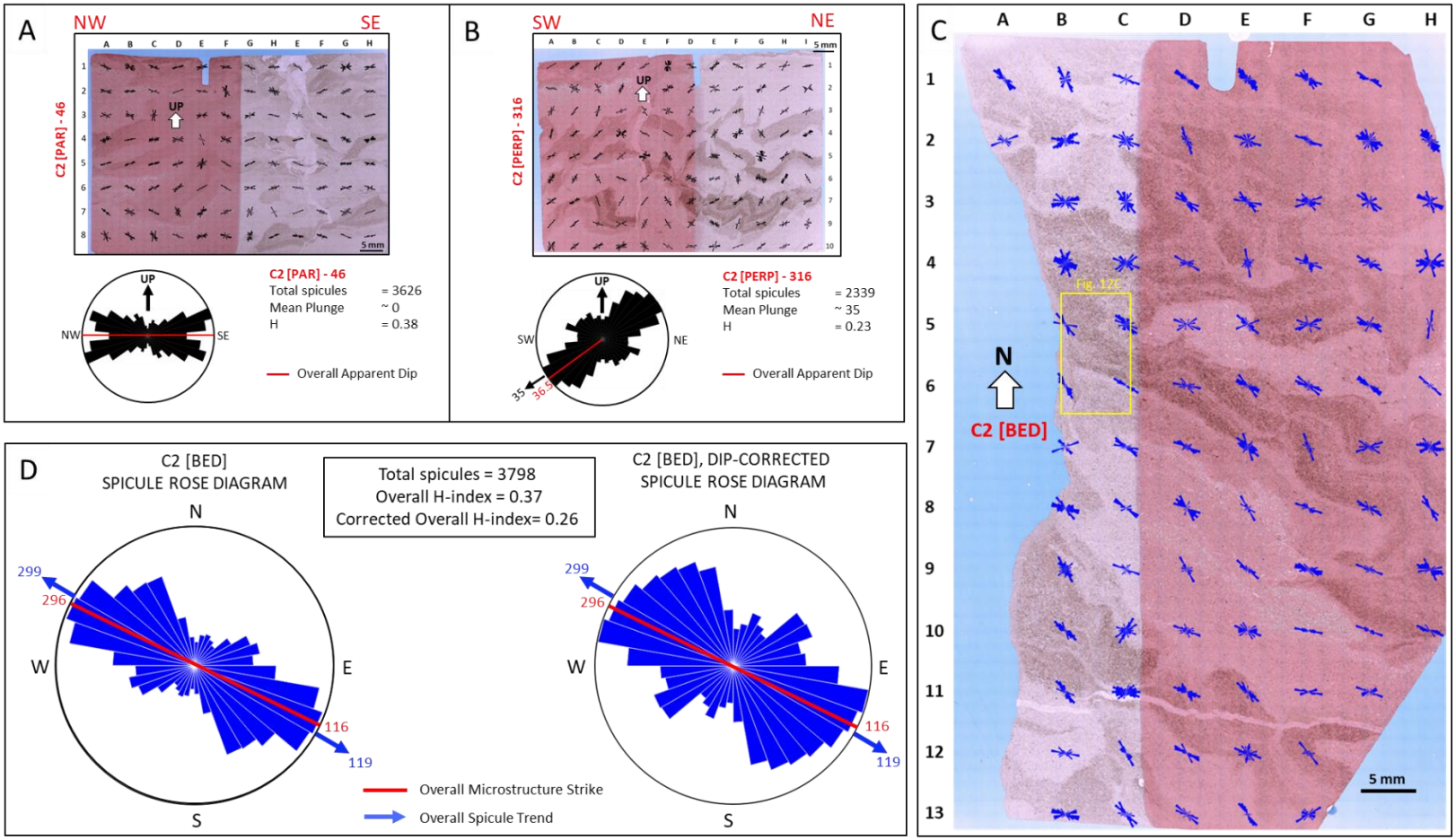

Figure 2.11(A) The overall mean spicule plunge in C2[PAR]-46 is about horizontal, similar to the overall mean apparent-dip of microbeds. In fine-scale, the spicules are plunging to two directions, NW and SW, following the attitude of their local microbeds. (B) The overall mean spicule plunge in C2[PERP]-316 almost coincides with the overall mean apparent-dip of microbeds. In fine-scale, the plunge variability reflects the local apparent-dip in which the spicules are measured. (C) Local mean spicule trends observed in C2[BED] are following the local strike of microfolds. The wellness of alignments seems to be dependent on the strike curvature of microfolds. For example, spicule alignments on the crestal area, where the curvature is high (e.g, slice #B4), are generally more chaotic than on the flank (e.g., slice E7). (D) The original vs. dip-corrected rose diagram of spicule trends observed in C2[BED].

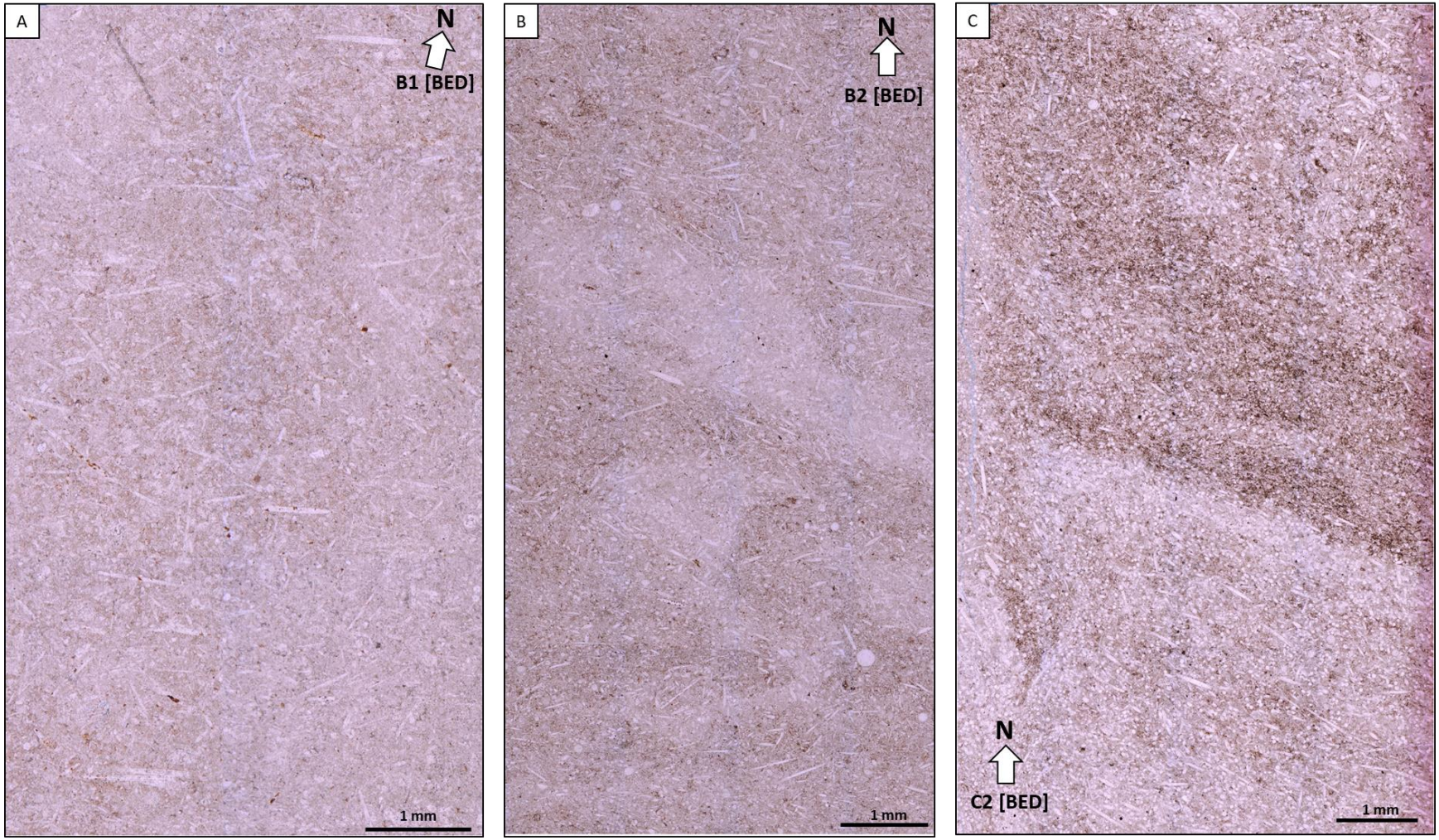

Figure 2.12 (A) A sample zoom-in figure, roughly covering slice E5 and E6: spicule trends are transverse to the strike of microfractures. (B) A sample zoom-in figure, roughly covering slice B9 and B10: spicule trends are parallel to sub-parallel to the strike of microfolds. (C) A sample zoom-in figure, roughly covering slice B5, B6, C5, and C6: spicules on the limbs of microstructures (low curvature) are more well-organized (unimodal), while spicules on the crest of microstructures (high curvature) are more chaotic (multimodal).

2.5.3 Spicule Abundance, Length, and Aspect Ratio

Spicules are the most abundant in bedding-plane thin sections, and the least abundant in thin sections oriented perpendicular to the overall mean spicule trends (Table 2). The difference in abundance is because more spicules are harder to identify (e.g., appear circular) in thin section planes that are of high obliquity with respect to the preferred spicule orientations. The grain abundance therefore supports our analysis that spicules are preferably aligned parallel to the microbeds and have a preferred compass trend. Because of this preferred orientation, the proportion of elongated grains is best determined from bedding-plane thin sections. Following this reasoning, spicules compose 12% of the samples analyzed in this study using Gazzi-Dickinson methods for calculating grain abundance (Ingersoll, 1984).

Table 2.2 Summary of Spicule Abundance

Thin Section	Relative to Microstructure Strike	Relative to the Dominant Spicule Trend	Spicule Count	Image slices counted	Mean spicules / slice
B1 [BED]	Bedding-Plane	Bedding-Plane	3334	76	44
B1 [PERP] - 0	Perpendicular	Parallel	1845	68	27
B1 [PAR] - 90	Parallel	perpendicular	2833	110	26
B2 [BED]	Bedding-Plane	Bedding-Plane	5246	107	49
B2 [PAR] - 200	Parallel	Parallel	4370	103	42
B2 [PERP] - 290	Perpendicular	perpendicular	2363	73	32
C2 [BED]	Bedding-Plane	Bedding-Plane	3798	87	44
C2 [PAR] - 46	Parallel	Parallel	3626	96	38
C2 [PERP] - 316	Perpendicular	perpendicular	2339	107	22
TOTAL			**29754**		

Spicule length is log-normally distributed, with mean values of 135 to 211 microns (Fig. 2.13). The spicule lengths measured in the thin sections parallel to the preferred spicule trend are consistently higher than those measured in the thin sections oriented perpendicular to the

preferred spicule trend (Fig. 2.13). Similar to the geometric reasoning used for grain abundance, more spicules appear shorter, if not circular, in thin section that are highly oblique to the preferred spicule direction. The grain length distributions also corroborate our observation that spicules are aligned parallel to microbeds and have a preferred compass trend. Note that although the bedding-plane thin sections provide the best visibility for spicule abundance, spicule length distributions in the bedding-plane thin sections vary depending on the magnitude of microbed deformation; for example, sample C2[BED] has the lowest length distribution compared to the cross-sectional thin sections due to its high microbed dip (see Fig. 2.11B).

The short-axes of spicules have positive correlation with respect to the long-axes. Short-axis lengths are normally distributed, with a mean of 13 microns and a standard deviation of 4.8 microns. The estimated spicule aspect ratios (long-axis percentiles divided by short-axis percentiles) are quite constant at ~ 10 (Table 3), suggesting that spicules in the Cutoff MTD follow a constant growth.

Table 2.3 Long- to Short-axis Percentile-Percentile Ratios

C2[BED]			
Percentile	Percentile Value		P - P Ratio
	long-axis (N = 60)	short-axis (N = 60)	
P10	75.97	8.23	9.23
P20	90.11	9.97	9.04
P30	98.04	10.57	9.27
P40	111.49	11.18	9.97
P50	125.06	12.29	10.18
P60	139.40	12.84	10.86
P70	156.11	13.60	11.48
P80	178.56	15.96	11.19
P90	216.03	22.16	9.75

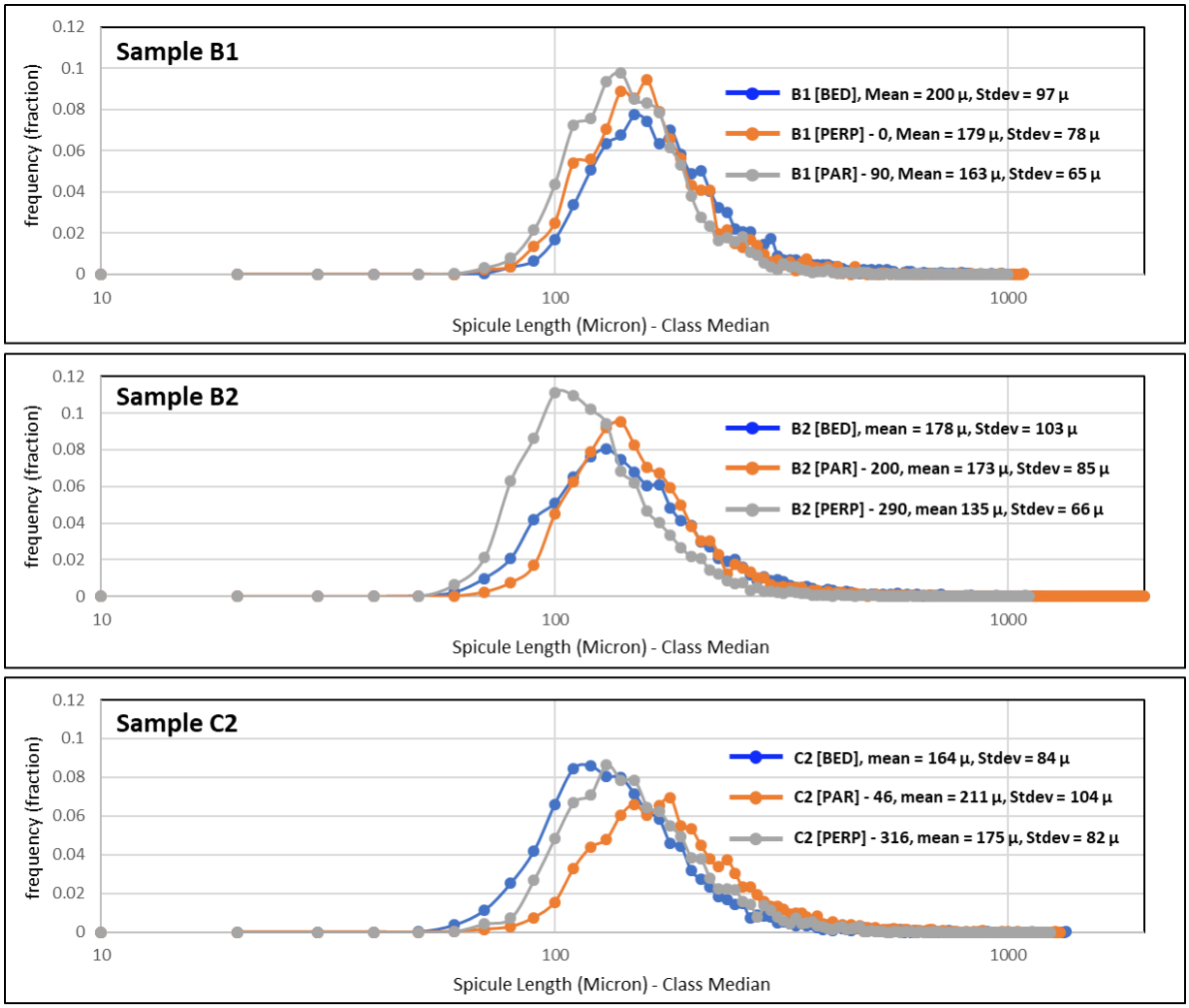

Figure 2.13 Distributions of spicule lengths in all samples: The measured spicule lengths are grouped into classes with 10-micron increments. The class medians are taken as the x-axis and the class frequency as the Y-axis. The differences in length distributions between thin section orientations are due to the obliquity of observation planes with respect to the long-axes of spicules.

2.5.4 Quantitative Analysis of Spicule Trends

We utilize the bedding-plane thin sections to quantify the variability of spicule trends, which emphasizes on comparing H-index in different scales, across samples, and by spicule lengths. The results of these two analyses will be presented as (1) irrespective of matrix-type (from the primary dataset), and (2) sorted by matrix types (from the secondary dataset).

A. H-Index Distribution

The previous sub-section highlights how the overall mean spicule trend in each sample has a distinctive corrected overall H-index, i.e., sample B1 = 0.16, sample C2 = 0.26, and sample B2 = 0.44, from the lowest to the highest respectively. Although the distributions of corrected local H-index show that this rank order holds true in general; the mean of corrected local H-index actually increases compared to the overall, i.e., slightly in Sample B1 and Sample B2 (from 0.16 – 0.2 and 0.45 – 0.49, respectively), but dramatically in sample C2 (from 0.26 to 0.37) (Fig. 2.14A). These differences can be explained by the variations of local spicule trend related to the strike sinuosity of microstructures. For example, microstructures in Sample B1 and Sample B2 have low strike sinuosity, such that the overall H-index is representative of the local H-index. However, microstructures in Sample C2 has a complex strike sinuosity, thus the resulting overall mean H-index is much lower than most local areas due to the averaging of complex microstructure (and thus spicule) orientations across the thin section. This finding complicates grain-fabric prediction in an MTD because the same overall spicule orientations can result from high local H-index with high strike sinuosity or low local H-index with low strike sinuosity (Fig. 2.14B). In addition, sample B2 and C2 have higher standard deviation as compared to sample B1, and therefore have a larger variety of local H-index (Fig 14A). These differences in standard deviation are in part influenced by the interaction between spicules and microstructure curvature, i.e., high local H-index (unimodal spicule trend) in low-curvature local microstructures, and low local H-index (multimodal spicule trend) in high-curvature local microstructures (described in section 4.2 C).

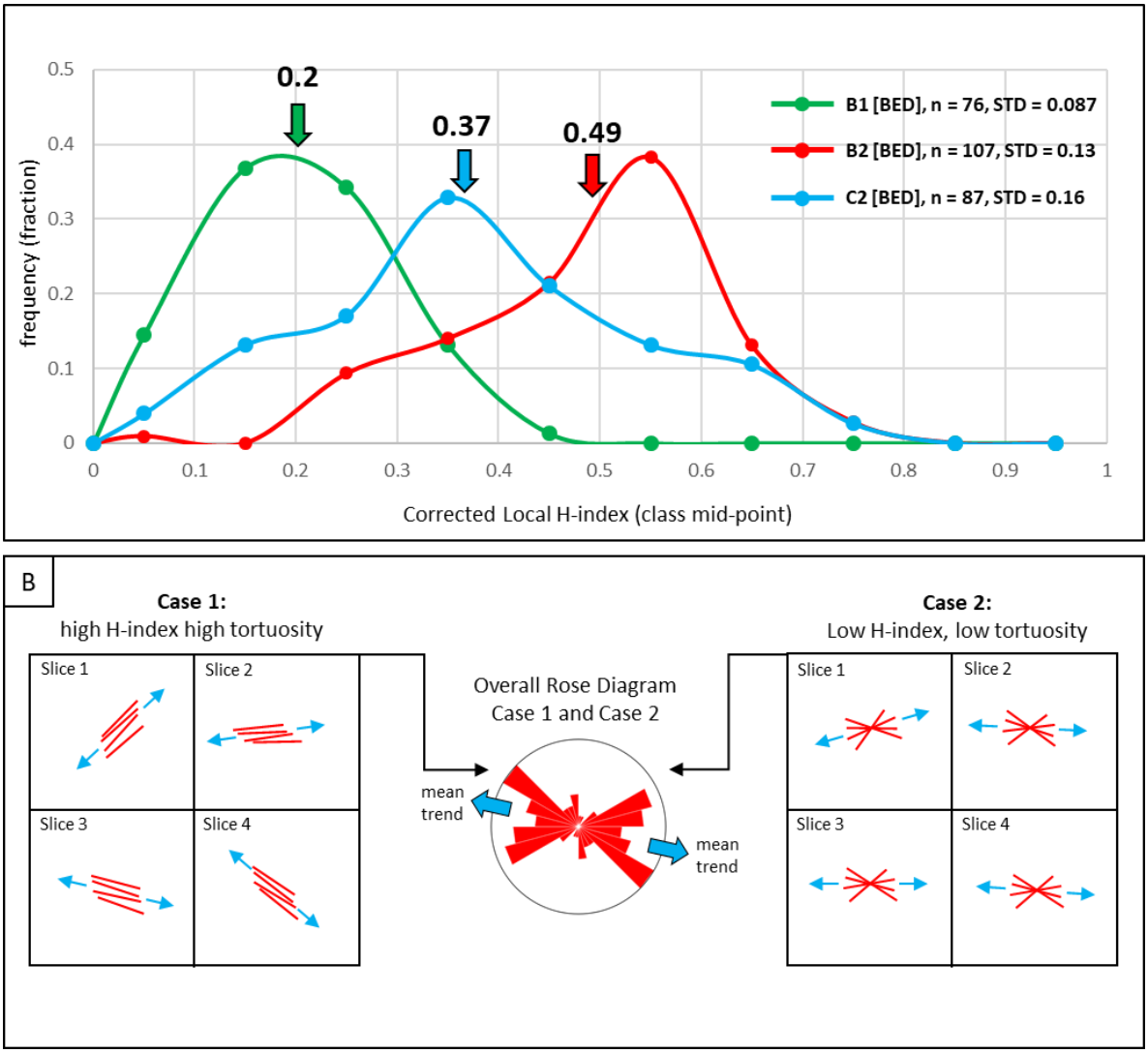

Figure 2.14 (A) Frequency distribution of dip-corrected H index for all bedding-plane thin sections: The calculated H index from individual slices is grouped into classes with 0.1 increments. The H index class mid-points are taken as the x-axis and frequencies as the y-axis. The upside-down arrows represent the averages of H-index calculated from the histogram, and the number of data (n) is essentially the total number of slices in the thin sections. (B) Case 1: elongated grains are well-organized in the individual slices but show more variability of local mean trends (high strike sinuosity). Case 2: elongated grains are poorly organized in individual zones, but have less variability of local mean trends. Both cases give the exact same rose diagram, with identical overall trend and H-index.

B. H-index and spicule length relationship

Cross-plots of overall H-index sorted by spicule lengths indicate that longer spicule grains tend to be more well-aligned than shorter grains. This observation holds for uncorrected (Fig. 2.15A) and dip-corrected H-index values (Fig. 2.15B). Although the trendline slopes of all samples are rather similar, the y-intercepts are distinctive, with sample B2 being the highest (~0.4), followed by sample C2 (~0.25) and sample B1 (~0). In conjunction with length distributions, y-intercept is also an important metric that directly controls the resultant overall H-index. While in this quantitative analysis we assume the trendlines to be completely linear, they can also become flattened as the grain lengths approach certain thresholds (see cross-plot B2[BED] and C2[BED]).

Note that the correlation coefficients tend to be higher in sample B1, and followed by sample B2 and C2. The disparity of correlation coefficient between samples can be explained as follows: (1) that measurements in sample B1 give true lengths (horizontal microbeds), while measurements in sample B2 (dip = 22°) and C2 (dip = 38°) yield apparent lengths, which are extremely difficult to correct, if not impossible; (2) the variations of local trend are more prominent in sample C2 (microstructures with high strike sinuosity); (3) the flattening of H-index as the grain lengths approach maximum – observed in sample B2 and C2.

C. Does Matrix Type Affect Spicule Orientation?

We separate two matrix types (micritic group for packstone lithofacies and argillaceous group for clayey and clay-rich packstone lithofacies) to test the effects of lithology/ mineralogy on spicule orientations. Note that the identification of clayey and clay-rich packstone is entirely visual, which renders them difficult to separate. We only collected data

in slices that have both micritic and argillaceous matrix, thus it is a dataset with some selection bias, but nonetheless informative.

Trendlines of grain length to H-index cross-plots show clear separations between matrix types in sample B2 and C2, with the argillaceous groups being generally higher in H-index compared to the micritic groups (Fig. 2.16A). However, mean spicule length in the argillaceous groups are consistently lower than in the micritic groups by 3%, 9%, and 14% for sample B1, B2, and C2, respectively. Consequently, the inherently high trendline positions of the argillaceous groups are counterbalanced by their shorter mean lengths, such that the resulting mean H-index for the argillaceous groups remain similar to the micritic groups (Fig. 2.16B). In Sample B1, trendline separation between matrix types are not observed, likely because there is not enough clay mineral (lack of clay-rich packstone; Fig 2.6A) to generate any noticeable differences.

Thus far, we have shown that H-index depends not only on grain lengths, but also on the presence of clay mineral. However, these two factors still cannot fully account for the disparity of H-index distributions across samples. If we consider only the H-index distributions of micritic groups in sample B1, B2, and C2 (see Fig. 2.16B), such that clay effect is nullified, the differences of mean H-index between sample B1 – B2, B1 – C2, and B2 – C2 are 96%, 37%, and 28% respectively, yet the differences of mean lengths in the secondary dataset are only 7.5%, 2.5%, and 4.6% respectively. Therefore, there is likely another factor(s) that dictates the H-index of grain-fabric alignments, which we interpret as the result of differential strain between MTD sub-segments and/or variation in microstructure types (see Simabrata et al., Part A).

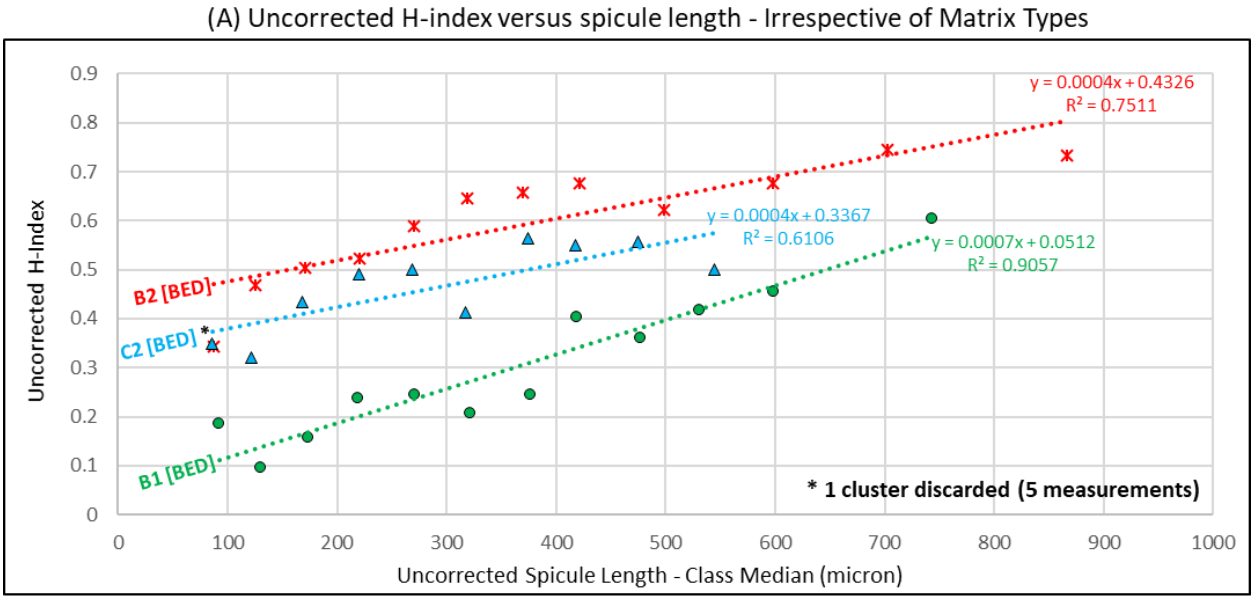

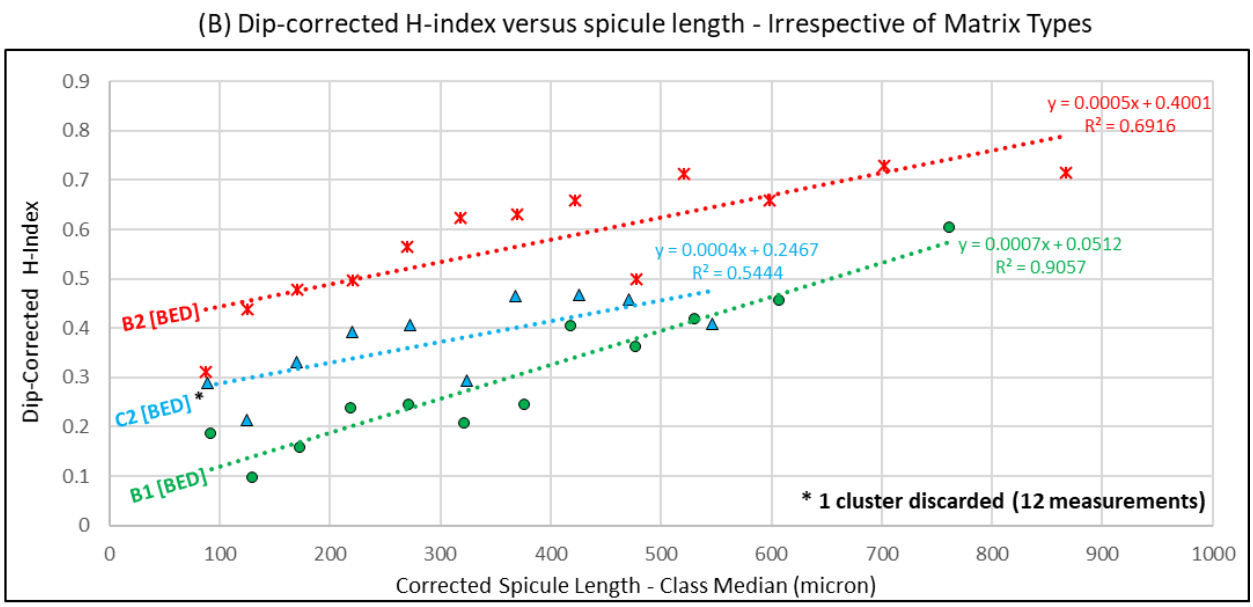

Figure 2.15 The spicule lengths are grouped into classes with 50-micron increment. In some cases, two classes or more are merged until the combined frequency (n spicule) is at least 20. The spicule data in a class must originate from multiple slices to prevent locality bias. For each length class, the H-Index was calculated and plotted against the class median of spicule length. The results of these procedures show that longer spicules are better aligned compared to the shorter counterparts. These observations are true for uncorrected (Fig. 2.14A) and dip-corrected (Fig. 2.14B) H-index. In sample B2 [BED] and C2 [BED], the H-index seems to flatten as the length groups approaches maximum.

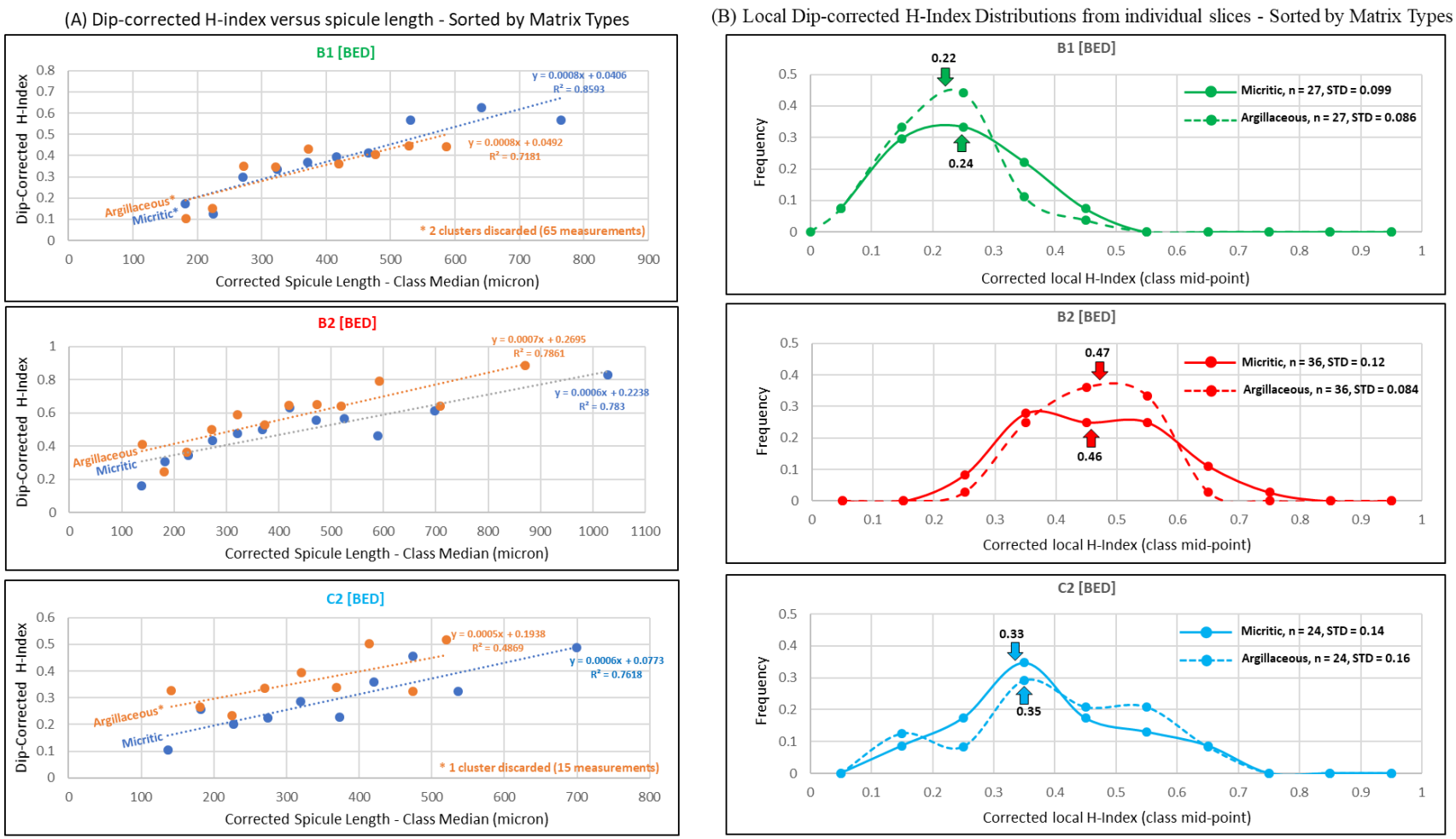

Figure 2.16 (A) Spicule length to H-index cross-plots, sorted by matrix types: The argillic groups show higher trendline positions compared to the micritic groups. The separation is very subtle in sample B1[BED], likely due to its lower clay content (lack of clay-rich packstone). This observation indicates that H-index is dependent not only on grain length, but also the presence of clay. (B) Dip-corrected H-index distributions from individual slices: The inherently high trendline position of argillic groups are counterbalanced by their relatively lower overall lengths. As a result, there is no significant difference in H-index distribution mean between argillic and micritic groups.

D. Resampling Test

Important quantitative metrices presented in this study are (1) mean spicule orientation, (2) wellness of alignment (H-index), and (3) linear relationships (y-intercept, trendline slope) between grain length and H-index. We employed data resampling to test if these metrics are dependent on sample size. The primary dataset was resampled at 10, 20, 30, and so on, up to 90 open circles per slice, with 10 resampling iterations each. The four quantitative metrics were recalculated for each iteration, and the standard deviation of outcomes are compared. The result of this test shows that mean spicule trend, H-index, and trendline y-intercept are very stable, while trendline slope is extremely volatile even under large sample-size. For other similar future studies, we recommend 30 or more open circles per slice to compute mean grain orientation and H-index, and 70 or more open circles per slice to compute grain length to H-index trendline properties. In addition, our data suggests that the observed slice number can be downsized to 25% (e.g., reduce 76 slices to 19, with 30 open circles per slice) and still provides an accurate estimation for mean grain orientation and H-index.

2.6 Discussion

2.6.1 The Origin of Microstructures

Based upon their outcrop-scale characteristics and distinctive deformation trends, the microstructures in the Cutoff MTD have been interpreted as the products of syn-emplacement deformation rather than of basin-wide post-lithification origin (i.e., tectonic) (Amerman et al., 2011). The characteristics of microstructures observed in our thin sections corroborate this interpretation. In contrast to the post-lithification fractures, the extensional microfractures in sample A exhibit the following features: (1) diffuse fracture margins with some spicules aligned parallel to sub-parallel to the fracture walls, (2) devoid of brittle-fractured grains, and (3) filled

with sediments instead of calcite cement (Fig. 2.17 A, B) – all which are diagnostic of pre-lithification failures (e.g., Antonellini et al., 1994; Millan et al., 2007). Isoclinal microfolds in sample B2 and sample C2 verge parallel to the paleotransport direction, which suggest along-flow shortening and shearing. Furthermore, the microstructures in sample B2 and C2 display evidence of non-brittle deformational features that include injection and tapered edge of detached microbeds, i.e., necking before ductile failures (Fig. 2.17 C, D), all of which indicate pre-lithification deformation.

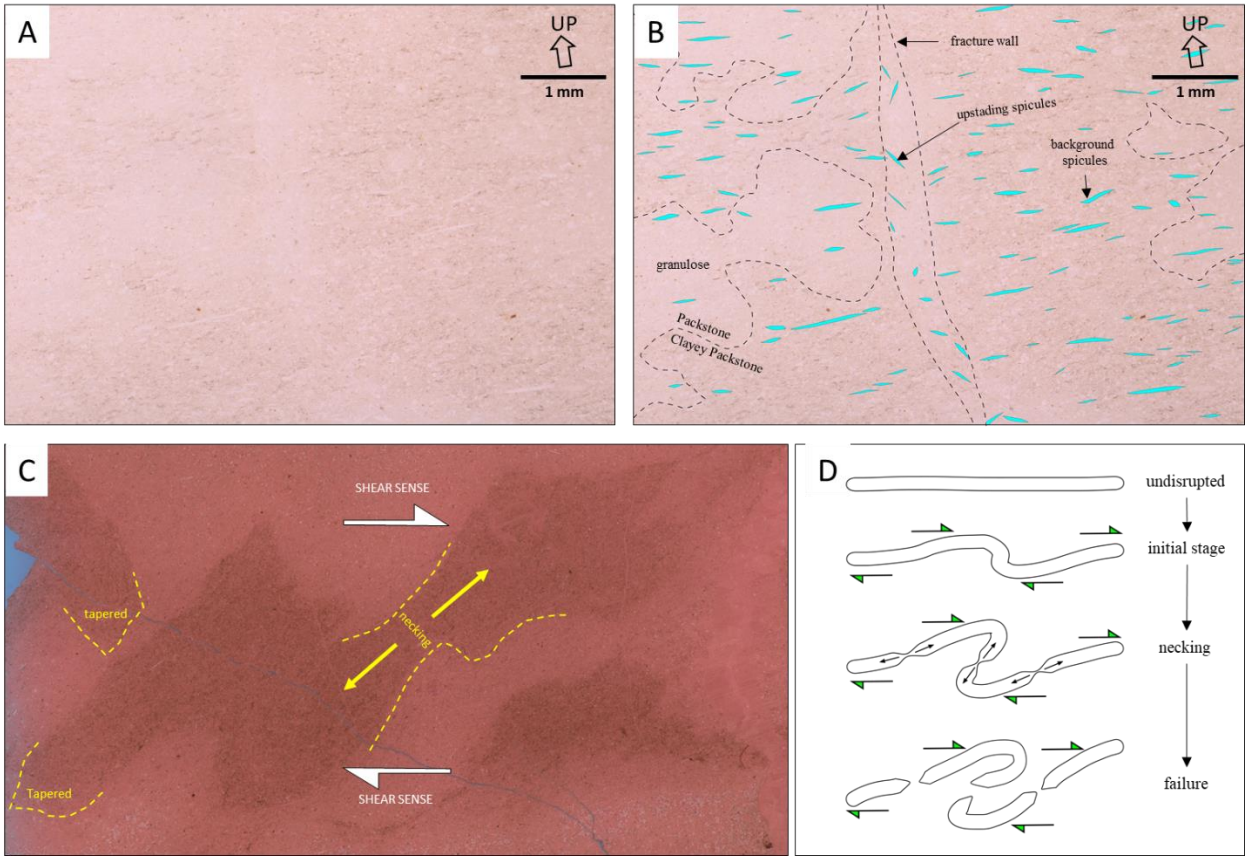

Figure 2.17 (A) Key features of microfractures in sample A: poorly-defined margins, devoid of fractured grains, filled with sediments instead of calcite cement, and localized upstanding spicules along the fracture walls. (B) Interpreted key features of microfractures in sample A. (C) An example of necking and tapered edges in sample C that evidenced of non-brittle, pre-lithification deformation. (D) Schematic diagram showing the stages of non-brittle failures in sample B and C.

2.6.2 The Origin of Spicule Alignments

The three-dimensional orientations of spicule grains are predictable from the associated microstructures in the thin sections. We interpret this co-dependency as an indication that the microstructures and spicule alignments were both originated from the mass-failure event in the Cutoff Formation. By incorporating the direction of paleotransport (N-S to NNE-SSW) inferred from outcrop-scale fold axes and shortening lineations (see Amerman et al. 2011), we interpret that the overall trends of spicules (WNW to ESE) are transverse to the direction of paleotransport in the Cutoff MTDs. Other researchers have interpreted similar grain-fabric to paleotransport relationships from other MTDs using magnetic fabrics and anisotropy of magnetic susceptibility (AMS) methods (e.g., Schwehr et al., 2007; Meissl et al., 2011; Kanamatsu et al., 2014; Weinberger et al., 2017; Alsop et al., 2020). Note that microbeds with fining-upward grain-size trends and sharp bases in sample B1 and sample B2 are likely 'muddy' calciturbidites (e.g., Boulesteix et al., 2019) deposited prior to the mass-failure event. Turbidity currents generally create a primary flow-parallel grain-fabric trend (Spotts, 1964; Sakai et al., 2002; Hiscott, 2006; Brown, 2015; Felletti et al., 2016) and a secondary flow-transverse grain-fabric trend (Brown, 2015). However, the absence of independent pre-MTD paleotransport indicators in the Cutoff Formation makes it difficult to deduce if the original grain alignments from turbidity currents have been completely obliterated, partially overprinted, or even amplified by the subsequent mass-transport event.

2.6.3 Paleotransport of The Cutoff MTDs

In the original work of Amerman et al. (2011), the interpretation of paleotransport direction of the Cutoff MTDs employed three different methods: (1) fold axes measurements, (2) shortening lineation measurements and (3) extensional lineation measurements (described in

section 2.2.). These methods assume that MTD paleotransport direction is in general perpendicular to fold axes and lineations (see Farrell, 1984; Martinsen and Bakken, 1990). The fold axes and shortening lineation methods result in N-S and NNW-SSE trends (more well-established approaches), respectively, but the outcome from extensional lineation method is ENE - WSW (Fig. 2.18A). Our new data suggest that spicule trends (WSW – ENE to WNW – ESE; Fig. 2.9 – Fig.2.11) in the Cutoff Formation are generally transverse to the regional paleotransport, and thus implying that extensional fractures in sub-segment B1 are parallel to the paleotransport direction. Flow-parallel extensional fractures and faults have been documented in MTD outcrops, which are interpreted as products of conjugate tensional stress in compressional regime (e.g., Alsop and Marco, 2011; Alsop et al., 2020), and in a flume-tank experiments (e.g., Sawyer et al., 2012), that we interpret as the results of fanning expansion. Applying this new assumption to the extensional lineation data from Amerman et al. (2011) and from this research yield NNW-SSE paleotransport direction, which is more in unison with the fold axes and shortening lineations (Fig. 2.18B). This alternative interpretation significantly reduces the discordance of paleotransport direction inferred from several different methods, albeit still showing some local variability, which is common in complexly-deformed MTDs (e.g., Sharman et al., 2015; Cardona et al., 2020).

2.6.4 Anisotropy Promoted by Grain-fabric Alignments

Fabric-scale factors that govern mechanical and petrophysical anisotropy are grain shape (aspect ratio) and preferred orientation (e.g., Daigle and Dugan, 2011; Nabawy, 2018). We hypothesize that the strength of anisotropy is also dependent on the wellness of alignment (H-index) and the proportion of oriented components (anisotropic) relative to the non-oriented components (isotropic). Non-oriented components can be either rounded grains and/or elongated

grains with random orientations (H-index ~ 0). Consequently, strong anisotropy only manifests if the proportion of oriented components and H-index are sufficiently high (Fig 19).

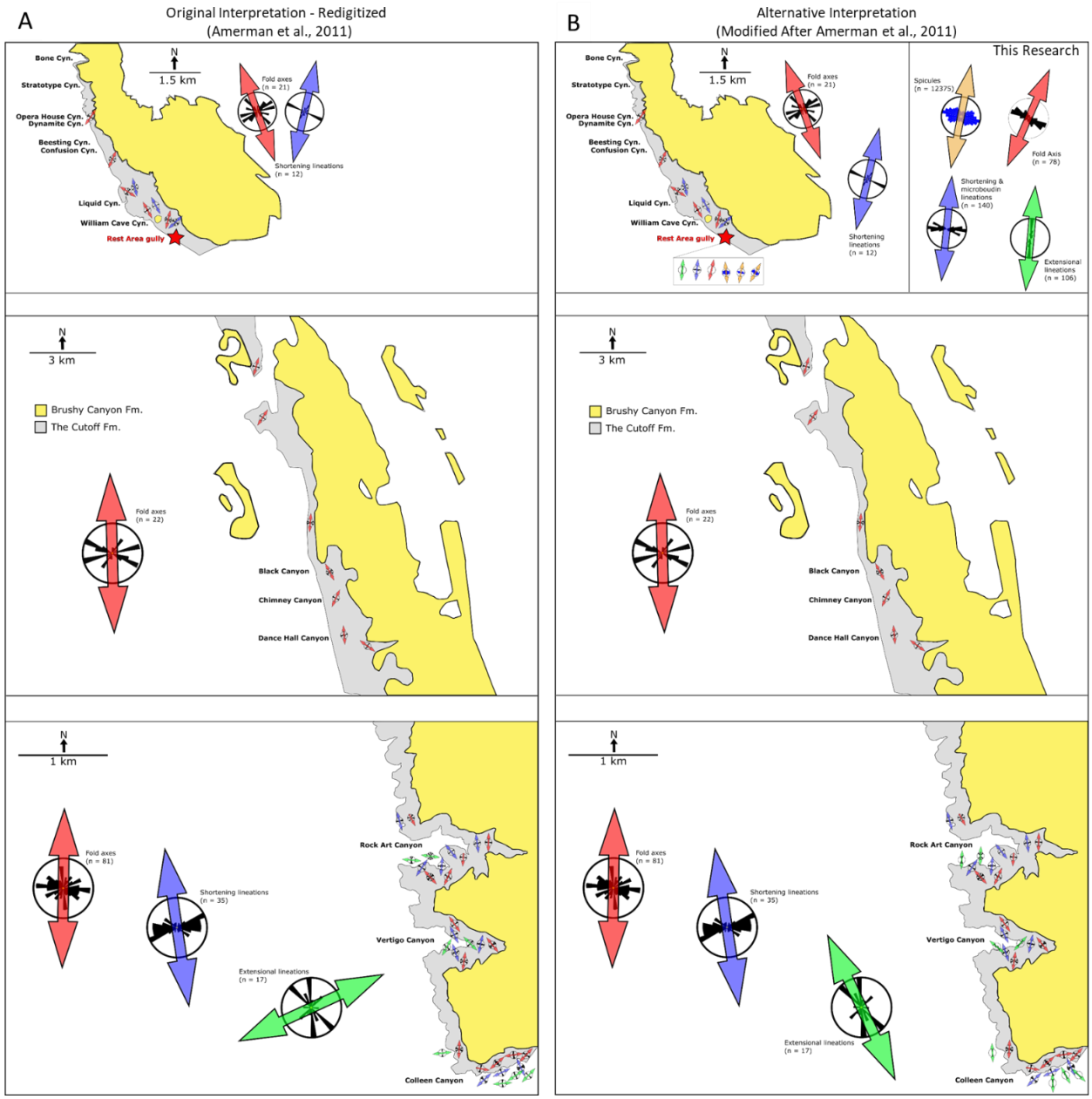

Figure 2.18 (A) Original interpretation of the Cutoff MTD paleotransport: The fold axes and shortening lineation methods are in agreement, but the result from extensional lineation method differs significantly. (B) Alternative interpretation of the Cutoff MTD paleotransport: Fold axes, fold axial plane, shortening lineation, extensional lineation, and grain-fabric alignment methods are now in unison.

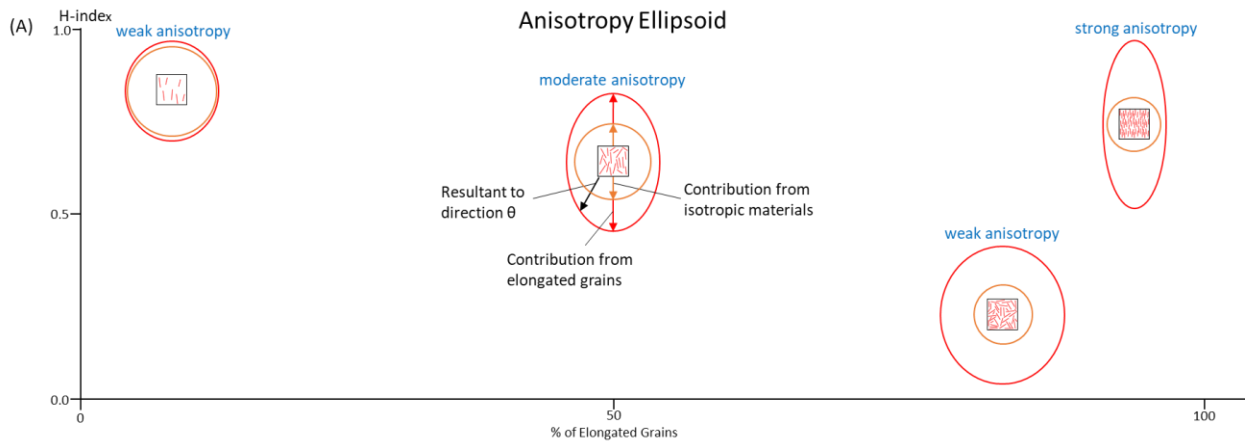

Figure 2.19 Illustration of anisotropy in elongated micro-grains: We assume that the property of interest to a certain direction (λaθ) can be represented with bidirectional vectors. The left figure depicts a property that grows stronger toward the long axis. The right figure illustrates a property that grows stronger toward the short axis. (B) This figure illustrates how the proportion of elongated micro-grains (anisotropic components) and R2 (degree of orientedness) control the shape of anisotropy. The resultant shape of anisotropy is assumed to be the aggregate of contributions from isotropic (orange circles) and anisotropic components.

In our research, the proportion of spicule grains is similar across samples, but the H-index is heterogeneous. Furthermore, grain-fabric alignment in one scale is not necessarily representative in another (e.g., overall thin section vs. local 5 mm^2. area) (see Fig. 2.14B). The anisotropy of the Cutoff MTD is interpreted as follows (Fig. 2.3): (1) sub-segment B1 has relatively weak anisotropy in all scales (low fine-scale H-index, low strike sinuosity), (2) sub-segment B2 has relatively strong anisotropy in all scales (high fine-scale H-index, low to moderate strike sinuosity), and (3) sub-segment C2 has relatively weak anisotropy in large scale, but strong in small scale (high fine-scale H-index, high strike sinuosity).

2.6.5 Predicting Grain-fabric Alignments from Large-scale Data

We propose a simplified model in which elongated grains lay on microbeds with their long-axes oriented perpendicular to paleotransport (Fig. 2.20 A). This satisfies the following criteria: (1) The plunge of elongated grains follows the apparent-dip of microbeds in which they

are measured and (2) observation planes (i.e., thin sections) cut parallel to the dominant grain orientation give longer grain length and more perceived grain abundance than the transverse observation plane (Fig. 2.20 A). The model ties grain orientations to microstructures, and microstructures to fold attitude, which enables upscaling (Fig. 2.20 B, C). For example, the dominant trend of elongated grains is likely parallel to the strike of MTD fold belts imaged in seismic data (Fig. 2.20 C); these fold belts have been observed in the Delaware and Midland Sub-basin (Allen et al., 2013; Bhatnagar et al., 2019). Note that the accuracy of H-index upscaling depends on the strike sinuosity of microstructures (described in section 4.4 A). In addition, the mean spicule plunge depends on the deformation of microbeds. For relatively undeformed microbeds, i.e., microbeds are parallel to the bedding plane (see sample A, Fig. 2.9), the mean spicule plunge likely approaches the apparent-dip magnitude of seismic reflections. If extensive microbed deformation occurs, i.e., microbeds are tilted with respect to the bedding plane (see sample B2 and C2, Figs. 2.10 - 2.11), the mean spicule plunge is likely at an angle with the apparent-dip of seismic reflectors. Note that the complexity of grain-fabric prediction can increase exponentially when MTD compartmentalization is accounted (see Simabrata et al., Part A).

2.7 Conclusions

Grain-fabric alignments in mass-transport deposits can promote anisotropy, which impacts hydrocarbon extraction, carbon sequestration, and geohazard assessments. However, the predictive properties of this phenomenon are poorly understood. This research contributes in elucidating three fundamental questions regarding grain-fabric alignments in MTDs: the 3D orientations, fine-scale heterogeneity, and the controls of grain lengths, clay mineral, and

microstructure styles. After observing, measuring, and analyzing over 29000 spicule bioclasts from three different MTD zones (segments), we conclude our research as follows:

1. The long-axes of spicules lay parallel to the plane of microbeds in which they are measured. Horizontal microbeds give horizontal spicules, while tilted microbeds result in plunging spicules. This observation is applicable in fine-scale (5 mm^2) or when upscaled to whole thin section (7.62 cm × 5.08 cm).
2. The long-axes of spicules also trend parallel to the strike of microfolds and perpendicular to the strike of microfractures. This observation is applicable in fine-scale (5 mm^2) or when upscaled to the whole thin section (7.62 cm × 5.08 cm). The overall mean trend of spicule long-axes is perpendicular to paleotransport direction.
3. The overall wellness of alignments (H-index) are distinctive across samples – 0.16, 0.44, and 0.26 for sample B1, B2, and C2, respectively. In fine-scale, the distribution mean of H-index in sample B1 and B2 increase slightly from 0.16 to 0.2 and 0.44 to 0.49, respectively, but change dramatically in sample C2 from 0.26 to 0.37. This is because sample B1 and B2 have low fine-scale trend variations (low strike sinuosity of microstructures), while sample C2 has high fine-scale trend variations (high strike sinuosity of microstructures).
4. H-index increases with greater long-axis lengths, in a linear fashion. It is also plausible that the trendline eventually flattened beyond specific length thresholds. Note that the aspect ratios of spicules in this research likely remain constant, irrespective of the long-axis lengths. Furthermore, the presence of clay mineral also increases H-index. However, length factor and clay mineral alone cannot fully account for the difference of H-index

between samples. We interpret that differential strain between MTD zones (segments) and/or microstructure types also govern the H-index of spicule bioclasts.

5. The methods and metrices developed in this work can be applied more broadly to other mass-transport deposits, as well as other types of rock-fabric alignments globally.

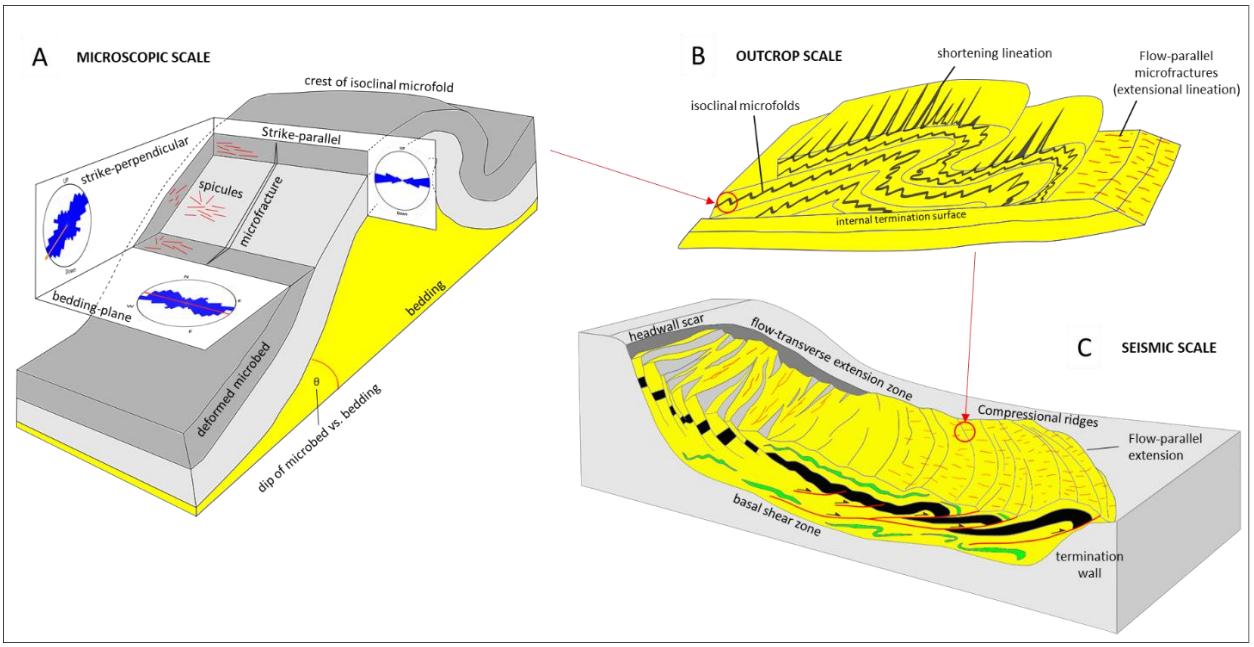

Figure 2.20 (A) Three-dimensional model of spicule orientations: the short axes of spicules are perpendicular to microbeds. If the microbed is tilted, the spicules are also tilted, such that the plunge of each spicule grain approaches the apparent dip of the microbed. Their long axes are parallel to the strike of isoclinal microfolds and transverse to the strike of flow-parallel microfractures / microfaults. Thin sections transverse to the dominant spicule alignments exhibit shorter apparent spicule length. (B) Outcrop Scale: the strikes of isoclinal folds are parallel to isoclinal microfolds and perpendicular to flow-parallel microfractures / microfaults. This allows for upscaling of grain-fabric alignments from microscopic to localized outcrop scale. (C) seismic scale: the strikes of isoclinal folds are likely parallel to the strike of compressional ridges, and transverse to the strike of conjugate extensional fractures/faults. This allows for upscaling of grain-fabric alignments from outcrop to localized seismic scale.

REFERENCES

A. L. O'Neill, 1963, Slope Failures in Foliated Rocks, Butte County, California: California, 40–42 p.

Allen, J., J. DeSantis, D. Koglin, and F. Chen, 2013, Integration of Structure and Stratigraphy in Bone Spring Tight Oil Sandstones using 3D Seismic in the Delaware Basin, TX, *in* Unconventional Resources Technology Conference, Denver, Colorado, 12-14 August 2013: Society of Exploration Geophysicists, American Association of Petroleum Geologists, Society of Petroleum Engineers, p. 2521–2527, doi:10.1190/urtec2013-262.

Alsop, G. I., and S. Marco, 2014, Fold and fabric relationships in temporally and spatially evolving slump systems: A multi-cell flow model: Journal of Structural Geology, v. 63, p. 27–49, doi:10.1016/j.jsg.2014.02.007.

Alsop, G. I., and S. Marco, 2011, Soft-sediment deformation within seismogenic slumps of the Dead Sea Basin: Journal of Structural Geology, v. 33, no. 4, p. 433–457, doi:10.1016/j.jsg.2011.02.003.

Alsop, G. I., and R. Weinberger, 2020, Are slump folds reliable indicators of downslope flow in recent mass transport deposits? Journal of Structural Geology, v. 135, no. October 2019, p. 104037, doi:10.1016/j.jsg.2020.104037.

Alsop, G. I., R. Weinberger, S. Marco, and T. Levi, 2020, Distinguishing coeval patterns of contraction and collapse around flow lobes in mass transport deposits: Journal of Structural Geology, v. 134, no. July 2019, p. 104013, doi:10.1016/j.jsg.2020.104013.

Alves, T. M., 2015, Submarine slide blocks and associated soft-sediment deformation in deep-water basins: A review: Marine and Petroleum Geology, v. 67, p. 262–285, doi:10.1016/j.marpetgeo.2015.05.010.

Amerman, R., E. P. Nelson, M. H. Gardner, and B. Trudgill, 2011, Submarine Mass-Transport Deposits of the Permian Cutoff Formation, West Texas, U.S.A.: Internal Architecture and Controls on Overlying Reservoir Sand Deposition, *in* Mass-Transport Deposits in Deepwater Settings: SEPM (Society for Sedimentary Geology), p. 235–267, doi:10.2110/sepmsp.096.235.

Antonellini, M. A., A. Aydin, and D. D. Pollard, 1994, Microstructure of deformation bands in porous sandstones at Arches National Park, Utah: Journal of Structural Geology, v. 16, no. 7, p. 941–959, doi:10.1016/0191-8141(94)90077-9.

Armitage, P. J., D. R. Faulkner, R. H. Worden, A. C. Aplin, A. R. Butcher, and J. Iliffe, 2011, Experimental measurement of, and controls on, permeability and permeability anisotropy of caprocks from the CO2 storage project at the Krechba Field, Algeria: Journal of

Geophysical Research: Solid Earth, v. 116, no. 12, p. 1–18, doi:10.1029/2011JB008385.

Armitage, D. A., B. W. Romans, J. A. Covault, and S. A. Graham, 2009, The Influence of Mass-Transport-Deposit Surface Topography on the Evolution of Turbidite Architecture: The Sierra Contreras, Tres Pasos Formation (Cretaceous), Southern Chile: Journal of Sedimentary Research, v. 79, no. 5, p. 287–301, doi:10.2110/jsr.2009.035.

Asmus, J. J., and G. M. Grammer, 2013, Characterization of Deepwater Carbonate Turbidites and Mass-Transport Deposits Utilizing High-Resolution Electrical Borehole Image Logs : Upper Leonardian (Lower Permian) Upper Bone Spring Limestone , Delaware Basin , Southeast New Mexico and West Texas: Gulf Coast Association of Geological Societies Transactions, v. 63, no. February, p. 27–65.

Backeberg, N. R., F. Iacoviello, M. Rittner, T. M. Mitchell, A. P. Jones, R. Day, J. Wheeler, P. R. Shearing, P. Vermeesch, and A. Striolo, 2017, Quantifying the anisotropy and tortuosity of permeable pathways in clay-rich mudstones using models based on X-ray tomography: Scientific Reports, v. 7, no. 1, p. 14838, doi:10.1038/s41598-017-14810-1.

Barton, N., and E. Quadros, 2015, Anisotropy is Everywhere, to See, to Measure, and to Model: Rock Mechanics and Rock Engineering, v. 48, no. 4, p. 1323–1339, doi:10.1007/s00603-014-0632-7.

Bhatnagar, P., S. Verma, and R. Bianco, 2019, Characterization of mass transport deposits using seismic attributes: Upper Leonard Formation, Permian Basin: Interpretation, v. 7, no. 4, p. SK19–SK32, doi:10.1190/INT-2019-0036.1.

Boulesteix, K., M. Poyatos-Moré, S. S. Flint, K. G. Taylor, D. M. Hodgson, and S. T. Hasiotis, 2019, Transport and deposition of mud in deep-water environments: Processes and stratigraphic implications: Sedimentology, v. 66, no. 7, p. 2894–2925, doi:10.1111/sed.12614.

Brown, D. M., 2015, Distinguishing Muddy Turbidites and Wave-Influenced Muddy Turbidites from Hemipelagic Deposits Using Grain Fabric : An Experimental Approach: The University of Texas at Austin.

Bull, S., J. Cartwright, and M. Huuse, 2009, A review of kinematic indicators from mass-transport complexes using 3D seismic data: Marine and Petroleum Geology, v. 26, no. 7, p. 1132–1151, doi:10.1016/j.marpetgeo.2008.09.011.

Cardona, S., L. J. Wood, B. Dugan, Z. Jobe, and L. J. Strachan, 2020, Characterization of the Rapanui mass-transport deposit and the basal shear zone: Mount Messenger Formation, Taranaki Basin, New Zealand: Sedimentology, v. 67, no. 4, p. 2111–2148, doi:10.1111/sed.12697.

Cardona, S., L. Wood, L. Moscardelli, and D. Dunlap, 2020, Cannibalization and sealing of deepwater reservoirs by mass-transport complexes-The jubilee field, gulf of Mexico: Interpretation, v. 8, no. 4, doi:10.1190/int-2019-0274.1.

Clare, M. A., T. Le Bas, D. M. Price, J. E. Hunt, D. Sear, M. J. B. Cartigny, A. Vellinga, W. Symons, C. Firth, and S. Cronin, 2018, Complex and Cascading Triggering of Submarine Landslides and Turbidity Currents at Volcanic Islands Revealed From Integration of High-Resolution Onshore and Offshore Surveys: Frontiers in Earth Science, v. 6, no. December, p. 1–24, doi:10.3389/feart.2018.00223.

Clare, M. A., P. J. Talling, P. G. Challenor, and J. E. Hunt, 2016, Tempo and Triggering of Large Submarine Landslides: Statistical Analysis for Hazard Assessment, *in* Advances in Natural and Technological Hazards Research: p. 509–517, doi:10.1007/978-3-319-20979-1_51.

Daigle, H., and B. Dugan, 2011, Permeability anisotropy and fabric development: A mechanistic explanation: Water Resources Research, v. 47, no. 12, p. 1–11, doi:10.1029/2011WR011110.

Day-Stirrat, R. J., P. B. Flemings, Y. You, and B. A. van der Pluijm, 2013, Modification of mudstone fabric and pore structure as a result of slope failure: Ursa Basin, Gulf of Mexico: Marine Geology, v. 341, p. 58–67, doi:10.1016/j.margeo.2013.05.003.

DeReuil, A. A., L. P. Birgenheier, and J. McLennan, 2019, Effects of Anisotropy and Saturation on Geomechanical Behavior of Mudstone: Journal of Geophysical Research: Solid Earth, v. 124, no. 8, p. 8101–8126, doi:10.1029/2018JB017034.

Dickinson, W. R., and C. Suczek, 1979, Plate tectonics and sandstone composition: American Association of Petroleum Geologists Bulletin, v. 63, no. 12, p. 2164–2182, doi:10.1306/2f9188fb-16ce-11d7-8645000102c1865d.

Dugan, B., 2012, Petrophysical and consolidation behavior of mass transport deposits from the northern Gulf of Mexico, IODP Expedition 308: Marine Geology, v. 315–318, p. 98–107, doi:10.1016/j.margeo.2012.05.001.

Dunham, R. J., 1962, Classification of Carbonate Rocks According to Depositional Texture: Huston, Texas, p. 108–121.

Erdlac, R. J., 1993, Small-scale structures in the Guadalupe Mountains region: implication for Laramide stress trends in the Permian basin, *in* Carlsbad region, New Mexico and west Texas: New Mexico Geological Society, Guidebook 44: p. 167–174.

Farrell, S. G., 1984, A dislocation model applied to slump structures, Ainsa Basin, South Central Pyrenees: Journal of Structural Geology, v. 6, no. 6, p. 727–736, doi:10.1016/0191-8141(84)90012-9.

Felletti, F., E. Dall'Olio, and G. Muttoni, 2016, Determining flow directions in turbidites: An integrated sedimentological and magnetic fabric study of the Miocene Marnoso Arenacea Formation (northern Apennines, Italy): Sedimentary Geology, v. 335, p. 197–215, doi:10.1016/j.sedgeo.2016.02.009.

Ferrill, D. A., R. N. McGinnis, A. P. Morris, K. J. Smart, Z. T. Sickmann, M. Bentz, D. Lehrmann, and M. A. Evans, 2014, Control of mechanical stratigraphy on bed-restricted

jointing and normal faulting: Eagle Ford Formation, south-central Texas: AAPG Bulletin, v. 98, no. 11, p. 2477–2506, doi:10.1306/08191414053.

Galley, J. E., 1958, Oil and Geology in the Permian Basin of Texas and New Mexico: North America habitat of Oil: AAPG Special Volume, p. 395–446.

Gamboa, D., and T. M. Alves, 2015, Three-dimensional fault meshes and multi-layer shear in mass-transport blocks: Implications for fluid flow on continental margins: Tectonophysics, v. 647–648, p. 21–32, doi:10.1016/j.tecto.2015.02.007.

Le Goff, J., A. Slootman, T. Mulder, T. Cavailhes, E. Ducassou, V. Hanquiez, J. Jaballah, and J. J. G. Reijmer, 2020, On the architecture of intra-formational Mass-Transport Deposits: Insights from the carbonate slopes of Great Bahama Bank and the Apulian Carbonate Platform: Marine Geology, v. 427, no. April, p. 106205, doi:10.1016/j.margeo.2020.106205.

Graham, S. A., R. V Ingersoll, and W. R. Dickinson, 1976, Common provenance for lithic grains in Carboniferous Sandstones from Ouachita Mountains and Black Warrior Basin: Journal of Sedimentary Petrology, v. 46, no. 3, p. 620–632.

Harris, M. T., 1987, (Permian), Sedimentology of the Cutoff Formation, Western Guadalupe Mountains , West Texas: New Mexico Geology, no. November, p. 74–79.

Haughton, P., C. Davis, W. McCaffrey, and S. Barker, 2009, Hybrid sediment gravity flow deposits - Classification, origin and significance: Marine and Petroleum Geology, v. 26, no. 10, p. 1900–1918, doi:10.1016/j.marpetgeo.2009.02.012.

Henderson, N., and L. Pena, 2017, Simulating effects of the permeability anisotropy on the formation of viscous fingers during waterflood operations: Journal of Petroleum Science and Engineering, v. 153, no. February 2016, p. 178–186, doi:10.1016/j.petrol.2017.03.047.

Henry, L. C., J. A. Wadsworth, B. Hansen, and K. Hartman, 2018, Erosion and ponding of Thunder Horse deepwater turbidites by mass transport complexes in Mississippi Canyon based on image log sedimentology: Marine and Petroleum Geology, v. 97, no. August, p. 639–658, doi:10.1016/j.marpetgeo.2018.08.006.

Hills, J. M., 1984a, Sedimentation, Tectonism, and Hydrocarbon Generation in Delaware Basin, West Texas and Southeastern New Mexico.: American Association of Petroleum Geologists Bulletin, v. 68, no. 3, p. 250–267, doi:10.1306/ad460a08-16f7-11d7-8645000102c1865d.

Hills, J. M., 1984b, Sedimentation, Tectonism, and Hydrocarbon Generation in Delaware Basin, West Texas and Southeastern New Mexico: AAPG Bulletin, v. 68, no. 3, p. 250–267, doi:10.1306/AD460A08-16F7-11D7-8645000102C1865D.

Hiscott, R. N., 2006, Paleoflow directions of Albian basin-floor turbidity currents in the Newfoundland Basin: Proceedings of the Ocean Drilling Program: Scientific Results, v. 210, no. May, doi:10.2973/odp.proc.sr.210.103.2007.

Horak, R. L., 1985, Trans-Pecos Tectonism and Its Effect on the Permian Basin, *in* Structure and Tectonics of Trans-Pecos Texas.

Huang, C., T. B. Byrne, W. B. Ouimet, C. W. Lin, J. C. Hu, L. Y. Fei, and Y. B. Wang, 2016, Tectonic foliations and the distribution of landslides in the southern Central Range, Taiwan: Tectonophysics, v. 692, p. 203–212, doi:10.1016/j.tecto.2016.06.004.

Hurd, G. S., 2016, Revised Stratigraphic Framework for The Cutoff Formation and Implications for Deepwater Systems Modified by Large-Scale Inflections in Slope Angle Below The Shelf Break: doi:10.1088/1751-8113/44/8/085201.

Hurd, G. S., C. Kerans, S. Fullmer, and X. Janson, 2016, Large-Scale Inflections in Slope Angle Below the Shelf Break: A First Order Control On the Stratigraphic Architecture of Carbonate Slopes: Cutoff Formation, Guadalupe Mountains National Park, West Texas, U.S.A.: Journal of Sedimentary Research, v. 86, no. 4, p. 336–362, doi:10.2110/jsr.2016.25.

Ingersoll, R. V. . B., 1984, The effect of grain size on detrital modes: A test of the Gazzi-Dickinson point-counting method: Geological Society of America Bulletin, v. 54, no. 1, p. 222–235.

Jablonská, D., C. N. Di Celma, G. I. Alsop, and E. Tondi, 2018, Internal architecture of mass-transport deposits in basinal carbonates: A case study from southern Italy: Sedimentology, v. 65, no. 4, p. 1246–1276, doi:10.1111/sed.12420.

Kanamatsu, T., K. Kawamura, M. Strasser, B. Novak, and Y. Kitamura, 2014, Flow dynamics of Nankai Trough submarine landslide inferred from internal deformation using magnetic fabric: geochem.Geophys.Geosysts., v. 0018, p. 4079–4092, doi:10.1002/2014GC005409.Received.

Kerans, C., and W. M. Fitchen, 1995, Sequence Hierarchy and Facies Architecture of a Carbonate-Ramp System: San Andres Formation of Algerita Escarpment and Western Guadalupe Mountains, West Texas and New Mexico: Bureau of Economic Geology, v. Repot of I.

Khan, S., R. Williams, S. Ansari, and N. Khosravi, 2012, Impact of mechanical anisotropy on design of hydraulic fracturing in shales: Society of Petroleum Engineers - Abu Dhabi International Petroleum Exhibition and Conference 2012, ADIPEC 2012 - Sustainable Energy Growth: People, Responsibility, and Innovation, v. 4, p. 3145–3151, doi:10.2118/162138-ms.

Kremer, K., S. B. Wirth, A. Reusch, D. Fäh, B. Bellwald, F. S. Anselmetti, S. Girardclos, and M. Strasser, 2017, Lake-sediment based paleoseismology: Limitations and perspectives from the Swiss Alps: Quaternary Science Reviews, v. 168, p. 1–18, doi:10.1016/j.quascirev.2017.04.026.

Kullman, A. J., 1999, Fracture networks and fault zone features in a deep water sandstone. Brushy Canyon Formation, west Texas [Unpublished Master's Thesis]: Colorado School of Mines.

Mao, P., J. Sun, F. Ning, G. Hu, Y. Wan, X. Cao, and N. Wu, 2020, Effect of permeability anisotropy on depressurization-induced gas production from hydrate reservoirs in the South China Sea: Energy Science and Engineering, v. 8, no. 8, p. 2690–2707, doi:10.1002/ese3.701.

Martinsen, O. J., and B. Bakken, 1990, Extensional and compressional zones in slumps and slides in the Namurian of County Clare, Ireland: Journal of the Geological Society, v. 147, no. 1, p. 153–164, doi:10.1144/gsjgs.147.1.0153.

Meissl, S., J. H. Behrmann, and C. Franke, 2011, Magnetic fabrics in Quaternary sediments, Ursa Basin, northern Gulf of Mexico record transport processes, compaction and submarine slumping: Marine Geology, v. 286, no. 1–4, p. 51–64, doi:10.1016/j.margeo.2011.05.007.

Van Der Merwe, W. C., D. M. Hodgson, and S. S. Flint, 2011, Origin and terminal architecture of a submarine slide: A case study from the Permian Vischkuil Formation, Karoo Basin, South Africa: Sedimentology, v. 58, no. 7, p. 2012–2038, doi:10.1111/j.1365-3091.2011.01249.x.

Millan, C., T. Paulsen, C. editor Raymond, T. Wilson, and S. International Symposium on Antarctic Earth, 2007, Microstructural study of natural fractures in Cape Roberts Project 3 core, western Ross Sea, Antarctica: Open-File Report - U. S. Geological Survey, p. Short Research Paper 053.

Moscardelli, L., and L. Wood, 2016, Morphometry of mass-transport deposits as a predictive tool: Bulletin of the Geological Society of America, v. 128, no. 1–2, p. 47–80, doi:10.1130/B31221.1.

Nabawy, B. S., 2018, Impacts of fossil anisotropy on the electric and permeability anisotropy of highly fossiliferous limestone: a case study: Marine Geophysical Research, v. 39, no. 4, p. 537–550, doi:10.1007/s11001-017-9335-2.

Nelson, E. P., E. P. Kullman, M. H. Gardner, and M. Batzle, 1999, Fault - fracture networks and related fluid flow and sealing, Brushy Canyon Formation, west Texas, *in* Faults and Subsurface Fluid Flow in the Shallow Crust: American Geophysical Union, p. 69–81.

Nourollah, H., M. Urosevic, and J. Keetley, 2015, Seal potential of shale sequences through seismic anisotropy: Case study from Exmouth Sub-basin, Australia: Interpretation, v. 3, no. 4, p. T257–T267, doi:10.1190/INT-2014-0284.1.

Nugraha, H. D., C. A.-L. Jackson, H. Johnson, and D. Hodgson, 2020, Evolution of flow cells within a mass-transport complex: Insights from the Gorgon Slide, offshore NW Australia: no. April, doi:10.31223/osf.io/zswe7.

Ogata, K., J. J. Mountjoy, G. A. Pini, A. Festa, and R. Tinterri, 2014, Shear zone liquefaction in mass transport deposit emplacement: A multi-scale integration of seismic reflection and outcrop data: Marine Geology, v. 356, p. 50–64, doi:10.1016/j.margeo.2014.05.001.

Ortiz-Karpf, A., D. M. Hodgson, and W. D. McCaffrey, 2015, The role of mass-transport

complexes in controlling channel avulsion and the subsequent sediment dispersal patterns on an active margin: The Magdalena Fan, offshore Colombia: Marine and Petroleum Geology, v. 64, p. 58–75, doi:10.1016/j.marpetgeo.2015.01.005.

Özbek, A., 2009, Variation of Schmidt hammer values with imbrication direction in clastic sedimentary rocks: International Journal of Rock Mechanics and Mining Sciences, v. 46, no. 3, p. 548–554, doi:10.1016/j.ijrmms.2008.09.003.

Pewsey, A., M. Neuhauser, and G. D. Ruxton, 2013, Circular Statistics in R: Oxford University.

Pisani, L. et al., 2022, Silicification, flow pathways, and deep-seated hypogene dissolution controlled by structural and stratigraphic variability in a carbonate-siliciclastic sequence (Brazil): Marine and Petroleum Geology, v. 139, no. February, p. 105611, doi:10.1016/j.marpetgeo.2022.105611.

Posamentier, H. W., 2003, Depositional elements associated with a basin floor channel-levee system: case study from the Gulf of Mexico: Marine and Petroleum Geology, v. 20, no. 6–8, p. 677–690, doi:10.1016/j.marpetgeo.2003.01.002.

Posamentier, H. W., and O. J. Martinsen, 2011, The Character and Genesis of Submarine Mass-Transport Deposits: Insights from Outcrop and 3D Seismic Data, *in* Mass-Transport Deposits in Deepwater Settings: SEPM (Society for Sedimentary Geology), p. 7–38, doi:10.2110/sepmsp.096.007.

Posamentier, H. W., and R. G. Walker, 2006, Facies Models Revisited, *in* The Character and Genesis of Submarine Mass-Transport Deposits: Insight from Outcrop and 3D Seismic Data: SEPM, p. 397–520, doi:10.2110/pec.06.84.0001.

Praet, N., J. Moernaut, M. Van Daele, E. Boes, P. J. Haeussler, M. Strupler, S. Schmidt, M. G. Loso, and M. De Batist, 2017, Paleoseismic potential of sublacustrine landslide records in a high-seismicity setting (south-central Alaska): Marine Geology, v. 384, p. 103–119, doi:10.1016/j.margeo.2016.05.004.

Sakai, T., M. Yokokawa, Y. Kubo, N. Endo, and F. Masuda, 2002, Grain fabric of experimental gravity flow deposits: Sedimentary Geology, v. 154, no. 1–2, p. 1–10, doi:10.1016/S0037-0738(02)00106-9.

Sammartini, M., J. Moernaut, F. S. Anselmetti, M. Hilbe, K. Lindhorst, N. Praet, and M. Strasser, 2019, An Atlas of Mass-Transport Deposits in Lakes, *in* Geophysical Monograph Series: p. 201–226, doi:10.1002/9781119500513.ch13.

Saroglou, H., P. Marinos, and G. Tsiambaos, 2003, The anisotropic nature of selected metamorphic rocks from Greece: 10th ISRM Congress, no. May, p. 1019–1023.

Sato, M., K. Panaghi, N. Takada, and M. Takeda, 2019, Effect of Bedding Planes on the Permeability and Diffusivity Anisotropies of Berea Sandstone: Transport in Porous Media, v. 127, no. 3, p. 587–603, doi:10.1007/s11242-018-1214-z.

Sawyer, D. E., P. B. Flemings, J. Buttles, and D. Mohrig, 2012, Mudflow transport behavior and deposit morphology: Role of shear stress to yield strength ratio in subaqueous experiments: Marine Geology, v. 307–310, p. 28–39, doi:10.1016/j.margeo.2012.01.009.

Sawyer, D. E., P. B. Flemings, B. Dugan, and J. T. Germaine, 2009, Retrogressive failures recorded in mass transport deposits in the Ursa Basin, Northern Gulf of Mexico: Journal of Geophysical Research: Solid Earth, v. 114, no. 10, p. 1–20, doi:10.1029/2008JB006159.

Schnellmann, M., F. S. Anselmetti, D. Giardini, and J. A. McKenzie, 2005, Mass movement-induced fold-and-thrust belt structures in unconsolidated sediments in Lake Lucerne (Switzerland): Sedimentology, v. 52, no. 2, p. 271–289, doi:10.1111/j.1365-3091.2004.00694.x.

Schwehr, K., N. Driscoll, and L. Tauxe, 2007, Origin of continental margin morphology: Submarine-slide or downslope current-controlled bedforms, a rock magnetic approach: Marine Geology, v. 240, no. 1–4, p. 19–41, doi:10.1016/j.margeo.2007.01.012.

Sharman, G. R., S. A. Graham, L. U. Masalimova, L. E. Shumaker, and P. R. King, 2015, Spatial patterns of deformation and paleoslope estimation within the marginal and central portions of a basin-floor mass-transport deposit, Taranaki Basin, New Zealand: Geosphere, v. 11, no. 2, p. 266–306, doi:10.1130/GES01126.1.

Shipp, R. C., J. A. Nott, and J. A. Newlin, 2004, Physical Characteristics and Impact of Mass Transport Complexes on Deepwater Jetted Conductors and Suction Anchor Piles, *in* All Days: OTC, p. 2001–2011, doi:10.4043/16751-MS.

Souza, V. H. P., F. H. R. Bezerra, L. C. Vieira, C. L. Cazarin, and J. A. Brod, 2021, Hydrothermal silicification confined to stratigraphic layers: Implications for carbonate reservoirs: Marine and Petroleum Geology, v. 124, no. October 2020, doi:10.1016/j.marpetgeo.2020.104818.

Spotts, J. . H., 1964, Grain orientation and imbrication in Miocene turbidity current sandstones, California: Journal of Sedimentary Petrology, v. 34, no. 2, p. 229–253.

Steventon, M. J., C. A. L. Jackson, D. M. Hodgson, and H. D. Johnson, 2019, Strain analysis of a seismically imaged mass-transport complex, offshore Uruguay: Basin Research, v. 31, no. 3, p. 600–620, doi:10.1111/bre.12337.

Strachan, L. J., and G. I. Alsop, 2006, Slump folds as estimators of palaeoslope: a case study from the Fisherstreet Slump of County Clare, Ireland: Basin Research, v. 18, no. 4, p. 451–470, doi:10.1111/j.1365-2117.2006.00302.x.

Strasser, M., K. Monecke, M. Schnellmann, and F. S. Anselmetti, 2013, Lake sediments as natural seismographs: A compiled record of Late Quaternary earthquakes in Central Switzerland and its implication for Alpine deformation: Sedimentology, v. 60, no. 1, p. 319–341, doi:10.1111/sed.12003.

Sun, Q., and T. Alves, 2020, Petrophysics of fine-grained mass-transport deposits: A critical

review: Journal of Asian Earth Sciences, v. 192, no. November 2019, doi:10.1016/j.jseaes.2020.104291.

Sun, Q., T. Alves, X. Xie, J. He, W. Li, X. Ni, and Q. Sun, 2017, Free gas accumulations in basal shear zones of mass-transport deposits (Pearl River Mouth Basin, South China Sea): An important geohazard on continental slope basins: Marine and Petroleum Geology, v. 81, p. 17–32, doi:10.1016/j.marpetgeo.2016.12.029.

Talling, P. J., D. G. Masson, E. J. Sumner, and G. Malgesini, 2012, Subaqueous sediment density flows: Depositional processes and deposit types: Sedimentology, v. 59, no. 7, p. 1937–2003, doi:10.1111/j.1365-3091.2012.01353.x.

Walker, W., Z. R. Jobe, J. F. Sarg, and L. Wood, 2021, Progradational slope architecture and sediment distribution in outcrops of the mixed carbonate-siliciclastic Bone Spring Formation, Permian Basin, west Texas: Geosphere, v. 17, no. 4, p. 1268–1293, doi:10.1130/GES02355.1.

Wang, J., H. Xie, and C. Li, 2021, Anisotropic failure behaviour and breakdown pressure interpretation of hydraulic fracturing experiments on shale: International Journal of Rock Mechanics and Mining Sciences, v. 142, no. August 2020, p. 104748, doi:10.1016/j.ijrmms.2021.104748.

Waters, G. A., R. E. Lewis, and D. C. Bentley, 2012, The effect of mechanical properties anisotropy in the generation of hydraulic fractures in organic shales: Society of Petroleum Engineers - SPE Middle East Unconventional Gas Conference and Exhibition 2012, UGAS - Unlocking Unconventional Gas: New Energy in the Middle East, no. Fig 1, p. 51–75.

Weinberger, R., T. Levi, G. I. Alsop, and S. Marco, 2017, Kinematics of Mass Transport Deposits revealed by magnetic fabrics: Geophysical Research Letters, v. 44, no. 15, p. 7743–7749, doi:10.1002/2017GL074471.

Woodcock, N. H., 1976, Structural style in slump sheets: Ludlow Series, Powys, Wales: Journal of the Geological Society, v. 132, no. 4, p. 399–415, doi:10.1144/gsjgs.132.4.0399.

Yang, K.-M., and S. L. Dorobek, 1995, the Permian Basin of West Texas and New Mexico: Flexural Modeling and Evidence for Lithospheric Heterogeneity Across the Marathon Foreland: Stratigraphic Evolution of Foreland Basins, no. January, p. 37–50, doi:10.2110/pec.95.52.0037.

You, D., J. Han, W. Hu, Y. Qian, Q. Chen, B. Xi, and H. Ma, 2018, Characteristics and formation mechanisms of silicified carbonate reservoirs in well SN4 of the Tarim Basin: Energy Exploration and Exploitation, v. 36, no. 4, p. 820–849, doi:10.1177/0144598718757515.

Zeng, Q. D., J. Yao, and J. Shao, 2019, Study of hydraulic fracturing in an anisotropic poroelastic medium via a hybrid EDFM-XFEM approach: Computers and Geotechnics, v. 105, no. January 2018, p. 51–68, doi:10.1016/j.compgeo.2018.09.010.

APPRENDIX A

SUPPLEMENTARY FILES

The supplementary files include permission for copyrighted materials, which have been properly cited in this thesis.

No	Journal Name	Publisher
1	Interpretations	SEGY
2	Tectonophysics	Elsevier
3	Geospehere	Geological Society of America (GSA)
4	GSA Bulletin	Geological Society of America (GSA)
5	Journal of Sedimentary Research	Society for Sedimentary Geology (SEPM)
6	SEPM Special Publication	Society for Sedimentary Geology (SEPM)
7	GSA Special Paper	Geological Society of America (GSA)